Fabrication of Fe_2O_3 Nano Architectures Based on Stress-induced Atomic Diffusion Used for Photocatalytic Water Splitting

Department of Mechanical Science and Engineering

Nagoya University

Yiyuan Xie

Contents

Chapter 1 Introduction

1.1 New energy: hydrogen

1.1.1 World energy outlook

Fossil fuels have been widely used as the most important energy sources since the beginning of industrial revolution. In 1901, oil companies found a huge amount of oil in Spindeltop, which made it possible to consume large quantities of oil [1]. The economic expansion started from the end of the Second World War also promoted the demand of oil and oil products. To date, global oil demand still on the rise. For example, in 2014, the world oil demand was 92.4 million barrels, and this number is estimated to be 99.1 in 2020 [2]. As the second most important fossil fuel, coal accounted for 30% global primary energy consumption, and 40% of global power generation relied on this fuel [3]. Natural gas is the number three fuel, representing a 22% share in power generation [4]. However, the three main fossil fuels were formed millions years ago from dead plants and animals, which means they are finite and nonrenewable, and the exhaustion of fossil fuels is only a matter of time. It has been estimated that oil will be run out in 2052, and the gas will be exhausted in 2060, and after 2088, the coal will no longer existed in the earth [5]. On the other hand, CO_2 emission from the fossil fuel is another challenge for our future. It is known that the increasing CO_2 concentration is the main reason of the global warming, which will lead to the global climate change, redistribution of global precipitation, permafrost ablation and sea level rise. Therefore, the search for the new, clean, sustainable and renewable energy is indispensable for our future.

Nowadays, several promising renewable energy sources such as solar energy, wind energy, geothermal energy and hydroelectric energy have been developed

widely. According to the statistics, 23.7% of the worldwide electricity generation and 19.2% of the global energy consumption was come from renewable energy sources in 2014 and 2015. It has been estimated that in 2040, the global power generation from renewable energy sources will be equal to coal and natural gas electricity generation [6]. However, solar energy and wind energy can not produce energy all the time, so it is necessary to transfer and delivery the energy by using the energy carrier. An energy carrier is a substance (energy form) or sometimes a phenomenon (energy system) that contains energy that can be later converted to other forms such as mechanical work or heat or to operate chemical or physical processes [7]. Hydrogen is an increasingly important energy carrier, it could be produced from the renewable energy and converted to electricity. For example, in a fuel cell vehicle, the power was provided by the chemical reaction between the oxygen from the air and compressed hydrogen, and the byproduct is only heat and water. In 2016, there are three hydrogen fuel cell vehicle (FCV) came out: the Toyota Mirai, the Hyundai ix35 FCEV, and the Honda Clarity.

1.1.2 Photoelectrochemical (PEC) hydrogen production

As a future energy, hydrogen is clean and zero emission, but the traditional method to produce energy is not environmentally friendly. Currently the most used technology for hydrogen production is steam reforming from fossil fuels, in 2014, 95% of hydrogen is made from natural gas [8]. Therefore, a clean hydrogen production method is desirable to meet the increasing needs of future hydrogen energy.

Solar water splitting is a new promising technology which could produce hydrogen using only sunlight and water. The concept of solar water splitting was first demonstrated by Fujishima and Honda in1972 [9], as shown in Fig. 1.1.

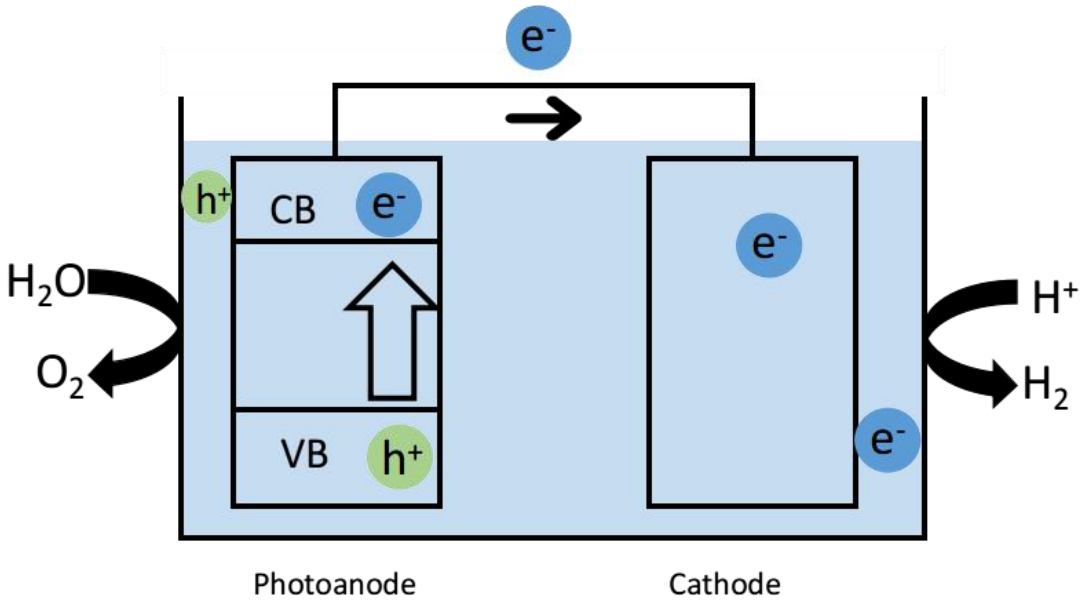

Fig. 1.1 Principle of solar water splitting.

The anode in a solar water splitting system can be a semiconductor material with a suitable band gap, while the cathode can be a metallic material. Both the anode and cathode are placed in water or an electrolyte solution. When the photoanode is illuminated by sunlight, the photons with an energy larger than the band gap of the semiconductor will excite the electrons from the valence band to the conduction band. The excited electrons will then move to the cathode and react with the electrolyte solution to produce hydrogen, and the reaction at cathode and anode could be summarized as the following equations:

$$2H^+ + 2e^- \rightarrow H_2 \tag{1.1}$$

and

$$2H_2O \rightarrow O_2 + 4H^+ + 4e^- \tag{1.2}$$

1.2 Semiconductor materials for PEC water splitting

1.2.1 Requirements for materials

There are some requirements for the semiconductor materials used for the working electrode in a PEC water splitting system. First requirement is the band gap of semiconductor materials. There is a minimum energy which is required to excite an electron from the valence band to the conduction band. When the semiconductor materials illuminated by the light which has a larger energy than the band gap of semiconductor materials, electrons will be excited from the valence band to the conduction band. The relationship between the band gap and the absorbable light wave length could be calculated by the following equation:

$$E = hf = \frac{hc}{\lambda}, \tag{1.3}$$

where E is the minimal increment of energy, h is the Planck constant, and f is the frequency. Comparing to the solar spectrum as shown in Fig. 1.2, the sunlight is consisted of 2% ultraviolet, 47% visible (corresponding wavelength of 380-780 nm) and 51% infrared [10].

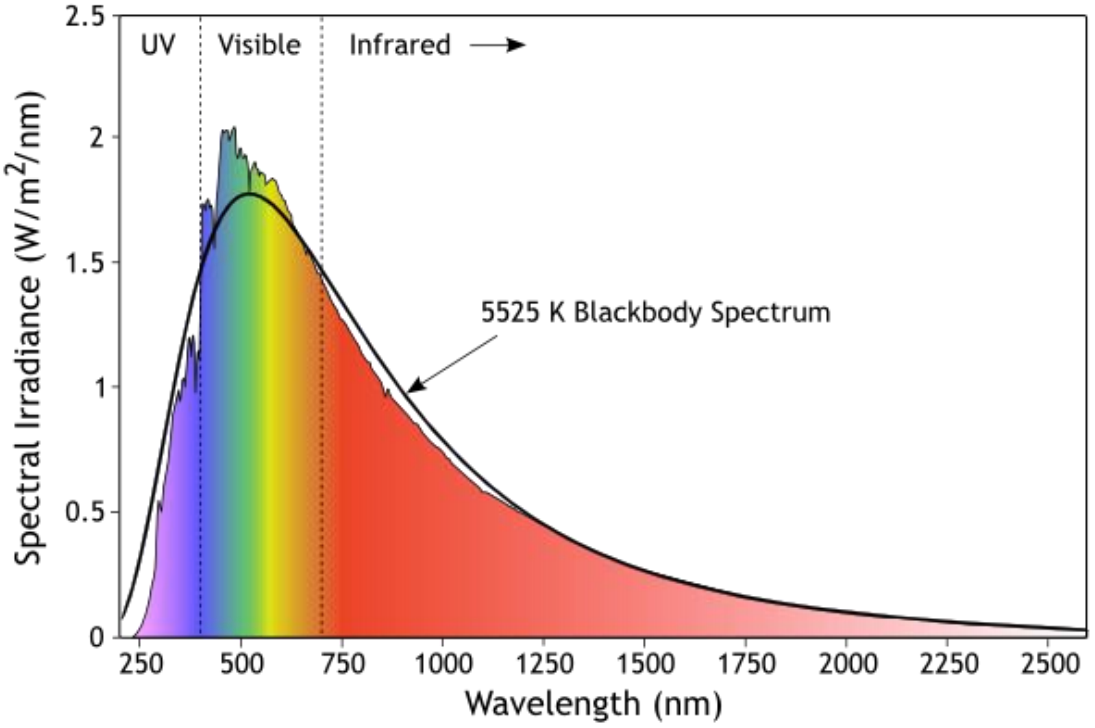

Fig. 1.2 Solar spectrum.

From the view of light absorption efficiency, the suitable material should absorb the wavelength of light over 400nm, which means the maximum band gap should be lower than 3.1 eV. On the other hand, the minimum band gap is determined by the redox potentials to split water molecules. The bottom level of the conduction band have to be more negative than the redox potential of H^+/H_2 (0 V vs. normal hydrogen electrode), while the top level of the valence band have to be more positive than the redox potential of O_2/H_2O (1.23 V). However, when considering the thermodynamic energy losses (0.3-0.4 eV) occurring during charge carrier transportation and the overpotential requirement for acceptable surface reaction kinetics (0.4-0.6 eV), a minimum band-gap of 1.93 eV is required, corresponding to light absorption at 700 nm. Therefore, semiconductors must have a band gap larger than 1.93 eV with suitable levels of conduction band and valence band for water splitting [11]. As a conclusion, the band gap of semiconductor materials used for solar water splitting should be higher than 1.93 eV to splitting water and lower than 3.1 eV to absorb more sunlight. Figure 1.3 shows the band gaps and band positions of typical n-type and p-type semiconductors utilized for PEC water splitting at pH =0. It should be

mentioned that the band positions of semiconductors are depending on the pH value of the electrolyte, the band positions changes by -59 mV per unit pH at 25 ^{o}C [12].

The second requirement for the materials is the stability against photocorrosion. Photocorrosion happens on most semiconductor materials, it means the photo generated holes from the semiconductor materials oxidize itself when illuminated by the light. Photocorrosion will dissolve the semiconductor materials or form a thin oxide film on the surface to block the charge transfer happened on the semiconductor/electrolyte interface [13]. Semiconductor materials with the wide band gap is considered to be stable against the photo corrosion, and the candidates with the narrow band gap are not suitable for this requirement, such as the ZnO [14-18]. However, this is opposite to the requirement of light absorption. Some candidate materials could find a balance such as TiO_2 [19-25] and SnO_2 [26-28], which show the excellent stability over a wide range of pH values and applied potentials. The third requirement is the fast transport of the photo generated electrons and holes in the semiconductor [29], which is helpful to reduce the electron/hole recombination in the materials. The forth requirement is the low overpotentials for the electrode reactions, and the fifth requirement is low cost [30].

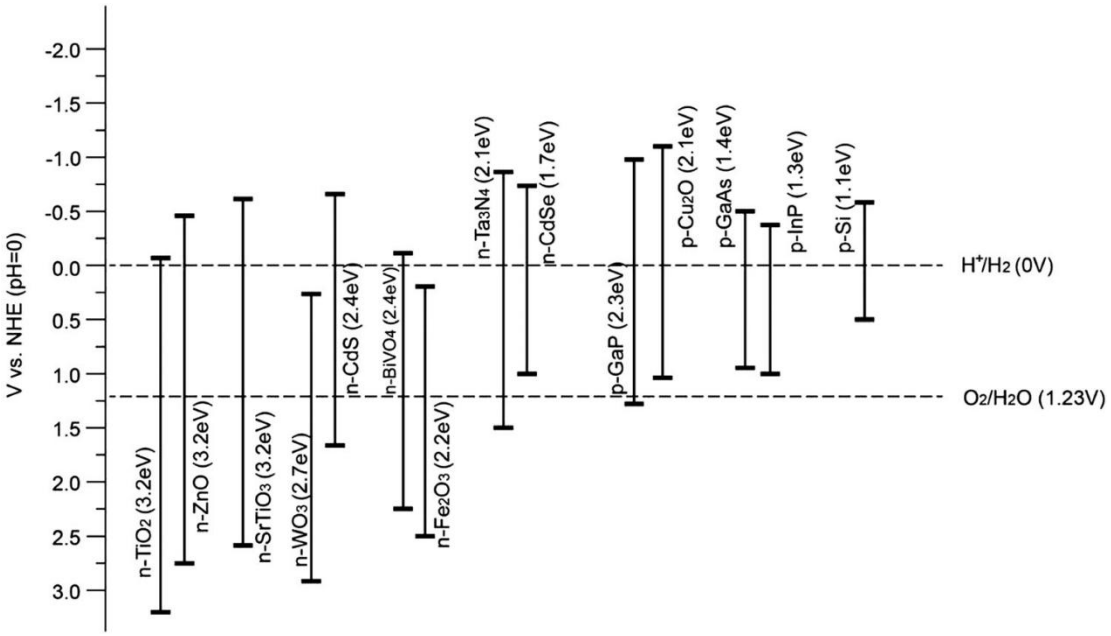

Fig. 1.3 Band positions of semiconductor materials [12].

1.2.2 Candidates materials

Although we have listed the requirements of the semiconductor materials used for the PEC water splitting in the last section, but until now there is no material could meet all the requirements. However, some materials have been widely studied as the working electrode in solar water splitting system due to the great potential according to the theoretical maximum solar to hydrogen efficiency (STH). For example, as photoanode materials, Fe_2O_3 [31-40] with the theoretical maximum STH efficiency of 15.3% [41], WO_3 [42-45] with the theoretical maximum STH efficiency of 7.5% [41], $BiVO_4$ [46-49] with the theoretical maximum STH efficiency of 9.2% [41], and TiO_2 [50-57] with the theoretical maximum STH efficiency of 2.0% [41] have been reported. On the other hand, as shown in Fig. 1.3, the conduction band positions of p-type semiconductors such as cuprous oxide (Cu_2O) and Si are more negative than the redox potential of H^+/H_2, and thus they can be employed as photocathodes for proton reduction. However, in most cases of their application is still limited, due to their facile cathodic photocorrosion in solution [58,59].

Among these materials, Fe_2O_3 could satisfy most of requirements, such as a suitable band gap of 2.1 eV, and the excellent stability against photo corrosion under alkaline conditions. Iron is also the fourth most common element on Earth (6.3% by weight) [60]. However, on the other hand, some disadvantages limit the solar to hydrogen efficiency of Fe_2O_3. These disadvantages include a very short excited-state lifetime, a short hole diffusion length of 2-4 nm [31], and poor electrical conductivity.

1.3 Fe_2O_3 photoanode for PEC cell

In order to overcome the disadvantages of Fe_2O_3, two popular strategies have been widely studied. One strategy is to dope another material on to Fe_2O_3, which could improve the electron transport ability [61], and alter the band gap [62]. Another strategy is the fabrication of nanostructured Fe_2O_3 photoanode, such as nanowire,

nanoparticle and nanotube to improve the photoelectrochemical performance.

1.3.1 Doped Fe_2O_3 photoanode

Usually, the doping materials on Fe_2O_3 photoanode can be classified as the following three categories: for metal element doping, n-type dopants are represented such as Ti^{4+} [63-67], Pt^{4+} [68-70], and Sn^{4+} [71-76]. P-type dopants include Mg^{2+} [77, 78], Ag^{+} [79], Cu^{2+} [80], and there is also nonisovalent substitutional doping using Al^{3+} [81]. Studies on non-metal element doping are dominated with Si [82-85] and P [86], which give superior activity.

1.3.2 Fe_2O_3 nanostructured photoanode

Compared with a bulk material, a nanostructured material could provide a significant enlargement of the material surface area, which could increase the absorption of sunlight and the contact surface between the photoanode and the electrolyte [87]. A nanostructure is also helpful in overcoming the short hole diffusion length of Fe_2O_3 because it could reduce the necessary path length of the electron transport [88], as shown in Fig. 1.4.

Some studies on the Fe_2O_3 nanostructures have been reported. For example, Gurudayal et al. reported a hematite nanorod photoanode with a photocurrent of 0.45 mA/cm^2 at 1.23 V vs. a reversible hydrogen electrode (RHE) [89]; Sivula et al. reported an Fe_2O_3 nanoparticle photoanode with a photocurrent of 0.56 mA/cm^2 at 1.23 V vs. RHE [90]; and Momeni et al. fabricated a Fe_2O_3 nanotube photoanode having a photocurrent of 0.35 mA/cm^2 at 1.23 V vs. RHE [91].

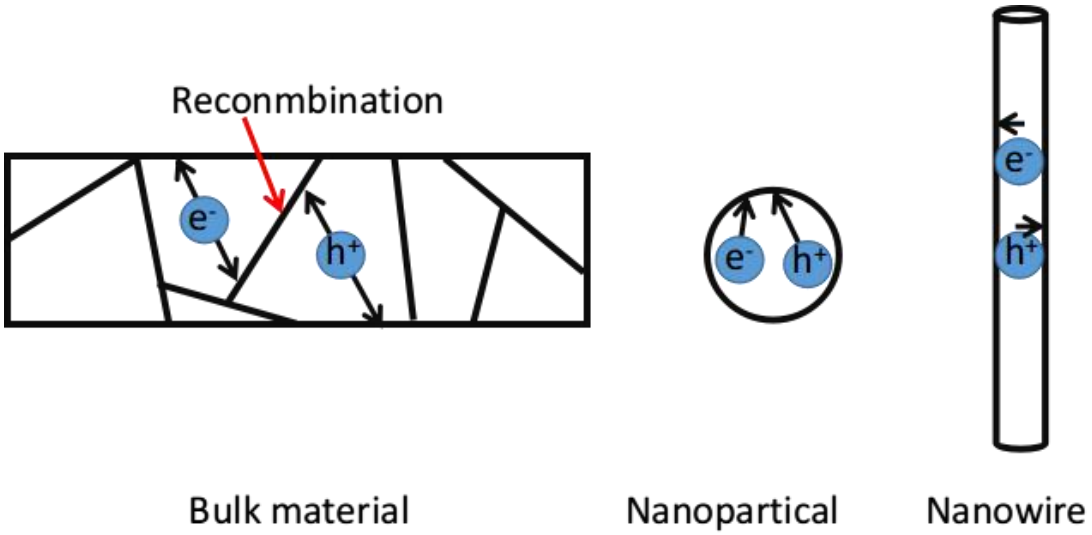

Fig. 1.4 Comparison of bulk material, nanopartical and nanowire structures.

Compared to other nanostructures, a nanowire array could provide a larger surface area because of the high aspect ratio, which could not only absorb more light than other nanostructures (e.g., nanorods, nanoparticles, and nanotubes), but also increase the photoelectrode/electrolyte interface area, thereby enhancing the chemical reaction of water splitting. Meanwhile, the nanowire structure could reduce the diffusion distance of photogenerated minority carriers from the center to the nanowire surface because of the small diameter. Therefore, photogenerated electron–hole pairs could efficiently separate before recombination in the nanowire structure, which could eventually increase the solar water splitting efficiency.

However, there are few literatures regarding to the studies of Fe_2O_3 nanowire array used for water splitting. Frites et al. have reported a Fe_2O_3 nanowire films with the maximum photo conversion efficiency of 1.69% at higher applied potential of -0.50 V vs. the saturated calomel electrode [92]. Sabina reported a Fe_2O_3 nanowire array with the the photocurrent of 0.5 mA/cm^2 at 1.23 V vs. RHE [93]. It is considered that the reason of poor photoelectrochemical performance could be the due to low density of nanowire array and the the growth direction of the nanowires is not vertical.

1.4 Research objectives

In this study, we aimed at improving the photoelectrochemical performance of photoanode by introducing Fe_2O_3 nanowire array. The growth mechanisms of both poly crystalline and single-crystalline Fe_2O_3 nanowire array will also been investigated in this work. Hence, the present study is intended to be carried out through the following objectives:

1) Fabrication of the high density Fe_2O_3 nanowire array

It is believed that the length, diameter and density of Fe_2O_3 nanowire arrays are key factors to affect the PEC efficiency of water splitting, therefore it is necessary to investigate the effect of nanowire parameters on the PEC performance. The first objective of this research is to fabricate the high density Fe_2O_3 nanowire array. In order to achieve this goal, the water vapor environment will be introduced in the fabrication process, which is believed to be able to increase the PEC efficiency of water splitting.

2) Fabrication of the single-crystal high density Fe_2O_3 nanowire array

single-crystal structure could reduce the recombination of photogenerated electrons and holes when the semiconductor is illuminated. The second goal of this research is to fabricate high density single-crystal Fe_2O_3 nanowire array, which is believed to be able to improve the PEC efficiency compared to the polycrystalline nanostructures.

3) Surface modification of single-crystal Fe_2O_3 nanowire array

There are two strategies which could improve the PEC efficiency theoretically, first is the nanostructuring, and the second is surface modification. After the high density single-crystal Fe_2O_3 nanowire array is achieved, the effect of doping other materials on the Fe_2O_3 nanowire photoanode will be investigated. The third goal of this research is to improve the PEC efficiency of high density single-crystal Fe_2O_3 nanowire array photoanode by making the surface modification.

4) Mechanism investigation of Fe_2O_3 nanowire growth

Since a new fabrication method has been introduced to fabricate Fe_2O_3 nanowire array in this study, it is necessary to clarify the mechanism of the nanowire growth.

1.5 Thesis organization

In this thesis, the author aimed at the importance of the PEC efficiency of water splitting by using Fe_2O_3 nanowire array. Two Fe_2O_3 fabrication methods have been demonstrated in this thesis, and the growth mechanisms of these two methods have also been studied. In order to improve the PEC efficiency, the relationship between the density and dimension of nanowires and the PEC performance has been investigated, and the surface modification by doping several materials on the surface of Fe_2O_3 nanowire array photoanode has also been carried out.

Chapter 1 introduces the background of this research, which includes: 1. why the clean sustainable hydrogen production method is necessary; 2. the advantage of solar water splitting; 3. several suitable materials for water splitting; 4. the current research of the Fe_2O_3 photoanode used for solar water splitting.

Chapter 2 describes the experimental approaches and several principles in this study. In this chapter, the original methods to evaluate the nanowire array, and the original design of the photoanode structure have been introduced in detail. The evaluation method of water splitting and the proposed mechanism of nanowire growth have also been described in this chapter.

Chapter 3 presents the fabrication method of high density Fe_2O_3 nanowire arrays. Several experimental conditions, such as heating time, heating temperature, and the volume of water vapor have been investigated in this chapter. The PEC efficiency of the fabricated Fe_2O_3 nanowire array photoanode has been measured.

Chapter 4 reports a fabrication method to obtain the high density single-crystal Fe_2O_3 nanowire array. The effect of surface roughness and residual stress have been discussed in this study. The PEC performance of high density single-crystal Fe_2O_3 nanowire array have been studied.

Chapter 5 compares the effect of different dopants on Fe_2O_3 nanowire photoanode. The optimized experimental conditions of each material have been investigated.

Chapter 6 is the conclusion of this thesis.

References

1. Roberts P. The end of oil: on the edge of a perilous new world[M]. Houghton Mifflin Harcourt, 2005.
2. Ramady M, Mahdi W. A New Paradigm: Protecting Market Share?[M]. Springer International Publishing, 2015: 3-32.
3. Dorian J P, Franssen H T, Simbeck D R. Global challenges in energy[J]. Energy Policy, 2006, 34(15): 1984-1991.
4. Howarth R W, Santoro R, Ingraffea A. Methane and the greenhouse-gas footprint of natural gas from shale formations[J]. Climatic Change, 2011, 106(4): 679.
5. Solomon E. The Mass Flux of Non-renewable Energy for Humanity[D]. University of Arkansas, 2016.
6. Panwar N L, Kaushik S C, Kothari S. Role of renewable energy sources in environmental protection: a review[J]. Renewable and Sustainable Energy Reviews, 2011, 15(3): 1513-1524.
7. https://en.wikipedia.org/wiki/Energy_carrier
8. Romm J. Tesla Trumps Toyota: Why Hydrogen Cars Can't Compete With Pure Electric Cars[J]. ThinkProgress, August, 2014, 5.
9. Fujishima A, Honda K. Electrochemical photolysis of water at a semiconductor electrode[J]. Nature, 1972, 238(5358): 37-38.
10. Di Quarto F, Sunseri C, Piazza S, et al. Semiempirical correlation between optical band gap values of oxides and the difference of electronegativity of the elements. Its importance for a quantitative use of photocurrent spectroscopy in corrosion studies[J]. The Journal of Physical Chemistry B, 1997, 101(14): 2519-2525.
11. Revankar S T, Majumdar P. Fuel cells: principles, design, and analysis[M]. CRC press, 2014.
12. Jiang C, Moniz S J A, Wang A, et al. Photoelectrochemical devices for solar water splitting materials and challenges[J]. Chemical Society Reviews, 2017, 46(15): 4645-4660.

13. Van de Krol R, Liang Y, Schoonman J. Solar hydrogen production with nanostructured metal oxides[J]. Journal of Materials Chemistry, 2008, 18(20): 2311-2320.
14. Yang X, Wolcott A, Wang G, et al. Nitrogen-doped ZnO nanowire arrays for photoelectrochemical water splitting[J]. Nano Letters, 2009, 9(6): 2331-2336.
15. Steinfeld A. Solar hydrogen production via a two-step water-splitting thermochemical cycle based on Zn/ZnO redox reactions[J]. International Journal of Hydrogen Energy, 2002, 27(6): 611-619.
16. Steinfeld A. Solar hydrogen production via a two-step water-splitting thermochemical cycle based on Zn/ZnO redox reactions[J]. International Journal of Hydrogen Energy, 2002, 27(6): 611-619.
17. Wolcott A, Smith W A, Kuykendall T R, et al. Photoelectrochemical study of nanostructured ZnO thin films for hydrogen generation from water splitting[J]. Advanced Functional Materials, 2009, 19(12): 1849-1856.
18. Wegner K, Ly H C, Weiss R J, et al. In situ formation and hydrolysis of Zn nanoparticles for H_2 production by the 2-step ZnO/Zn water-splitting thermochemical cycle[J]. International Journal of Hydrogen Energy, 2006, 31(1): 55-61.
19. Khan S U M, Al-Shahry M, Ingler W B. Efficient photochemical water splitting by a chemically modified n-TiO_2[J]. science, 2002, 297(5590): 2243-2245.
20. Ni M, Leung M K H, Leung D Y C, et al. A review and recent developments in photocatalytic water-splitting using TiO_2 for hydrogen production[J]. Renewable and Sustainable Energy Reviews, 2007, 11(3): 401-425.
21. Wang G, Wang H, Ling Y, et al. Hydrogen-treated TiO_2 nanowire arrays for photoelectrochemical water splitting[J]. Nano letters, 2011, 11(7): 3026-3033.
22. Tang J, Durrant J R, Klug D R. Mechanism of photocatalytic water splitting in TiO_2. Reaction of water with photoholes, importance of charge carrier dynamics, and evidence for four-hole chemistry[J]. Journal of the American Chemical Society, 2008, 130(42): 13885-13891.
23. Galińska A, Walendziewski J. Photocatalytic water splitting over Pt-TiO_2 in the

presence of sacrificial reagents[J]. Energy & Fuels, 2005, 19(3): 1143-1147.

24. Wolcott A, Smith W A, Kuykendall T R, et al. Photoelectrochemical water splitting using dense and aligned TiO_2 nanorod arrays[J]. Small, 2009, 5(1): 104-111.
25. Cowan A J, Tang J, Leng W, et al. Water splitting by nanocrystalline TiO_2 in a complete photoelectrochemical cell exhibits efficiencies limited by charge recombination[J]. The Journal of Physical Chemistry C, 2010, 114(9): 4208-4214.
26. Ni M, Leung M K H, Leung D Y C, et al. A review and recent developments in photocatalytic water-splitting using TiO_2 for hydrogen production[J]. Renewable and Sustainable Energy Reviews, 2007, 11(3): 401-425.
27. Cesar I, Kay A, Gonzalez Martinez J A, et al. Translucent thin film Fe_2O_3 photoanodes for efficient water splitting by sunlight: nanostructure-directing effect of Si-doping[J]. Journal of the American Chemical Society, 2006, 128(14): 4582-4583.
28. Saito R, Miseki Y, Sayama K. Highly efficient photoelectrochemical water splitting using a thin film photoanode of $BiVO_4$ /SnO_2/ WO_3 multi-composite in a carbonate electrolyte[J]. Chemical Communications, 2012, 48(32): 3833-3835.
29. Jing D, Guo L, Zhao L, et al. Efficient solar hydrogen production by photocatalytic water splitting: from fundamental study to pilot demonstration[J]. International Journal of Hydrogen Energy, 2010, 35(13): 7087-7097.
30. Walter M G, Warren E L, McKone J R, et al. Solar water splitting cells[J]. Chemical reviews, 2010, 110(11): 6446-6473.
31. Sivula K, Le Formal F, Grätzel M. Solar water splitting: progress using hematite (α-Fe_2O_3) photoelectrodes[J]. ChemSusChem, 2011, 4(4): 432-449.
32. Hu Y S, Kleiman-Shwarsctein A, Forman A J, et al. Pt-doped α-Fe_2O_3 thin films active for photoelectrochemical water splitting[J]. Chemistry of Materials, 2008, 20(12): 3803-3805.
33. Thimsen E, Le Formal F, Grätzel M, et al. Influence of plasmonic Au nanoparticles on the photoactivity of Fe_2O_3 electrodes for water splitting[J]. Nano

letters, 2010, 11(1): 35-43.

34. Saremi-Yarahmadi S, Wijayantha K G U, Tahir A A, et al. Nanostructured α-Fe_2O_3 electrodes for solar driven water splitting: effect of doping agents on preparation and performance[J]. The Journal of Physical Chemistry C, 2009, 113(12): 4768-4778.
35. Kim J Y, Magesh G, Youn D H, et al. Single-crystalline, wormlike hematite photoanodes for efficient solar water splitting[J]. Scientific reports, 2013, 3: 2681.
36. Zhong D K, Sun J, Inumaru H, et al. Solar water oxidation by composite catalyst/α-Fe_2O_3 photoanodes[J]. Journal of the American Chemical Society, 2009, 131(17): 6086-6087.
37. Cummings C Y, Marken F, Peter L M, et al. New insights into water splitting at mesoporous α-Fe_2O_3 films: a study by modulated transmittance and impedance spectroscopies[J]. Journal of the American Chemical Society, 2011, 134(2): 1228-1234.
38. Tilley S D, Cornuz M, Sivula K, et al. Light-Induced Water Splitting with Hematite: Improved Nanostructure and Iridium Oxide Catalysis[J]. Angewandte Chemie, 2010, 122(36): 6549-6552.
39. Lin Y, Zhou S, Sheehan S W, et al. Nanonet-based hematite heteronanostructures for efficient solar water splitting[J]. Journal of the American Chemical Society, 2011, 133(8): 2398-2401.
40. Kay A, Cesar I, Grätzel M. New benchmark for water photooxidation by nanostructured α-Fe_2O_3 films[J]. Journal of the American Chemical Society, 2006, 128(49): 15714-15721.
41. Tamirat A G, Rick J, Dubale A A, et al. Using hematite for photoelectrochemical water splitting: a review of current progress and challenges[J]. Nanoscale Horizons, 2016, 1(4): 243-267.
42. Wang H, Deutsch T, Turner J A. Direct water splitting under visible light with nanostructured hematite and WO_3 photoanodes and a $GaInP_2$ photocathode[J]. Journal of the Electrochemical Society, 2008, 155(5): F91-F96.

43. Cristino V, Caramori S, Argazzi R, et al. Efficient photoelectrochemical water splitting by anodically grown WO3 electrodes[J]. Langmuir, 2011, 27(11): 7276-7284.
44. Hwang D W, Kim J, Park T J, et al. Mg-doped WO_3 as a novel photocatalyst for visible light-induced water splitting[J]. Catalysis Letters, 2002, 80(1): 53-57.
45. Pihosh Y, Turkevych I, Mawatari K, et al. Photocatalytic generation of hydrogen by core-shell $WO_3/BiVO_4$ nanorods with ultimate water splitting efficiency[J]. Scientific reports, 2015, 5.
46. Kim T W, Choi K S. Nanoporous BiVO4 photoanodes with dual-layer oxygen evolution catalysts for solar water splitting[J]. Science, 2014, 343(6174): 990-994.
47. Ng Y H, Iwase A, Kudo A, et al. Reducing graphene oxide on a visible-light $BiVO_4$ photocatalyst for an enhanced photoelectrochemical water splitting[J]. The Journal of Physical Chemistry Letters, 2010, 1(17): 2607-2612.
48. Iwase A, Kudo A. Photoelectrochemical water splitting using visible light responsive $BiVO_4$ fine particles prepared in an aqueous acetic acid solution[J]. Journal of Materials Chemistry, 2010, 20(35): 7536-7542.
49. Jia Q, Iwashina K, Kudo A. Facile fabrication of an efficient $BiVO_4$ thin film electrode for water splitting under visible light irradiation[J]. Proceedings of the National Academy of Sciences, 2012, 109(29): 11564-11569.
50. Khan S U M, Al-Shahry M, Ingler W B. Efficient photochemical water splitting by a chemically modified n-TiO_2[J]. science, 2002, 297(5590): 2243-2245.
51. Ni M, Leung M K H, Leung D Y C, et al. A review and recent developments in photocatalytic water-splitting using TiO_2 for hydrogen production[J]. Renewable and Sustainable Energy Reviews, 2007, 11(3): 401-425.
52. Park J H, Kim S, Bard A J. Novel carbon-doped TiO_2 nanotube arrays with high aspect ratios for efficient solar water splitting[J]. Nano letters, 2006, 6(1): 24-28.
53. Wang G, Wang H, Ling Y, et al. Hydrogen-treated TiO_2 nanowire arrays for photoelectrochemical water splitting[J]. Nano letters, 2011, 11(7): 3026-3033.
54. Tang J, Durrant J R, Klug D R. Mechanism of photocatalytic water splitting in

TiO_2. Reaction of water with photoholes, importance of charge carrier dynamics, and evidence for four-hole chemistry[J]. Journal of the American Chemical Society, 2008, 130(42): 13885-13891.

55. Zhang Z, Zhang L, Hedhili M N, et al. Plasmonic gold nanocrystals coupled with photonic crystal seamlessly on TiO_2 nanotube photoelectrodes for efficient visible light photoelectrochemical water splitting[J]. Nano letters, 2012, 13(1): 14-20.
56. Pu Y C, Wang G, Chang K D, et al. Au nanostructure-decorated TiO_2 nanowires exhibiting photoactivity across entire UV-visible region for photoelectrochemical water splitting[J]. Nano letters, 2013, 13(8): 3817-3823.
57. Galińska A, Walendziewski J. Photocatalytic water splitting over Pt-TiO_2 in the presence of sacrificial reagents[J]. Energy & Fuels, 2005, 19(3): 1143-1147.
58. Paracchino A, Laporte V, Sivula K, et al. Highly active oxide photocathode for photoelectrochemical water reduction[J]. Nature materials, 2011, 10(6): 456-461.
59. Sun K, Shen S, Liang Y, et al. Enabling silicon for solar-fuel production[J]. Chemical reviews, 2014, 114(17): 8662-8719.
60. Gordon R M, Martin J H, Knauer G A. Iron in north-east Pacific waters[J]. Nature, 1982, 299(5884): 611-612.
61. Kleiman-Shwarsctein A, Huda M N, Walsh A, et al. Electrodeposited aluminum-doped α-Fe_2O_3 photoelectrodes: experiment and theory[J]. Chemistry of Materials, 2009, 22(2): 510-517.
62. Niu M, Huang F, Cui L, et al. Hydrothermal synthesis, structural characteristics, and enhanced photocatalysis of SnO_2/α-Fe_2O_3 semiconductor nanoheterostructures[J]. ACS nano, 2010, 4(2): 681-688.
63. Morin F J. Electrical Properties of α-$Fe_2O_3$and α-Fe_2O_3Containing Titanium[J]. Physical Review, 1951, 83(5): 1005.
64. Zandi O, Klahr B M, Hamann T W. Highly photoactive Ti-doped α-Fe_2O_3 thin film electrodes: resurrection of the dead layer[J]. Energy & Environmental Science, 2013, 6(2): 634-642.
65. Kronawitter C X, Zegkinoglou I, Shen S H, et al. Titanium incorporation into hematite photoelectrodes: theoretical considerations and experimental

observations[J]. Energy & Environmental Science, 2014, 7(10): 3100-3121.

66. Pu A, Deng J, Li M, et al. Coupling Ti-doping and oxygen vacancies in hematite nanostructures for solar water oxidation with high efficiency[J]. Journal of Materials chemistry A, 2014, 2(8): 2491-2497.
67. Deng J, Zhong J, Pu A, et al. Ti-doped hematite nanostructures for solar water splitting with high efficiency[J]. Journal of Applied Physics, 2012, 112(8): 084312.
68. Hu Y S, Kleiman-Shwarsctein A, Forman A J, et al. Pt-doped α-Fe_2O_3 thin films active for photoelectrochemical water splitting[J]. Chemistry of Materials, 2008, 20(12): 3803-3805.
69. Cha H G, Song J, Kim H S, et al. Facile preparation of Fe_2O_3thin film with photoelectrochemical properties[J]. Chemical Communications, 2011, 47(8): 2441-2443.
70. Neufeld O, Toroker M C. Platinum-doped α-Fe_2O_3 for enhanced water splitting efficiency: a DFT+ U study[J]. The Journal of Physical Chemistry C, 2015, 119(11): 5836-5847.
71. Ling Y, Wang G, Wheeler D A, et al. Sn-doped hematite nanostructures for photoelectrochemical water splitting[J]. Nano letters, 2011, 11(5): 2119-2125.
72. Bohn C D, Agrawal A K, Walter E C, et al. Effect of tin doping on α-Fe_2O_3 photoanodes for water splitting[J]. The Journal of Physical Chemistry C, 2012, 116(29): 15290-15296.
73. Frydrych J, Machala L, Tucek J, et al. Facile fabrication of tin-doped hematite photoelectrodes–effect of doping on magnetic properties and performance for light-induced water splitting[J]. Journal of Materials Chemistry, 2012, 22(43): 23232-23239.
74. Dunn H K, Feckl J M, Müller A, et al. Tin doping speeds up hole transfer during light-driven water oxidation at hematite photoanodes[J]. Physical Chemistry Chemical Physics, 2014, 16(44): 24610-24620.
75. Shinde P S, Choi S H, Kim Y, et al. Onset potential behavior in α-Fe_2O_3 photoanodes: the influence of surface and diffusion Sn doping on the surface

states[J]. Physical Chemistry Chemical Physics, 2016, 18(4): 2495-2509.

76. Annamalai A, Lee H H, Choi S H, et al. Sn/Be sequentially co-doped hematite photoanodes for enhanced photoelectrochemical water oxidation: effect of Be2+ as co-dopant[J]. Scientific reports, 2016, 6: 23183.
77. Lin Y, Xu Y, Mayer M T, et al. Growth of p-type hematite by atomic layer deposition and its utilization for improved solar water splitting[J]. Journal of the American Chemical Society, 2012, 134(12): 5508-5511.
78. Hou Y, Zuo F, Dagg A, et al. A Three‐Dimensional Branched Cobalt-Doped α-Fe_2O_3 Nanorod/MgFe2O4 Heterojunction Array as a Flexible Photoanode for Efficient Photoelectrochemical Water Oxidation[J]. Angewandte Chemie, 2013, 125(4): 1286-1290.
79. Shen S, Zhou J, Dong C L, et al. Surface engineered doping of hematite nanorod arrays for improved photoelectrochemical water splitting[J]. Scientific reports, 2014, 4: 6627.
80. Ingler W B, Khan S U M. Photoresponse of spray pyrolytically synthesized copper-doped p-Fe_2O_3 thin film electrodes in water splitting[J]. International Journal of Hydrogen Energy, 2005, 30(8): 821-827.
81. Kleiman-Shwarsctein A, Huda M N, Walsh A, et al. Electrodeposited aluminum-doped α-Fe_2O_3 photoelectrodes: experiment and theory[J]. Chemistry of Materials, 2009, 22(2): 510-517.
82. Cesar I, Kay A, Gonzalez Martinez J A, et al. Translucent thin film Fe_2O_3 photoanodes for efficient water splitting by sunlight: nanostructure-directing effect of Si-doping[J]. Journal of the American Chemical Society, 2006, 128(14): 4582-4583.
83. Cesar I, Sivula K, Kay A, et al. Influence of feature size, film thickness, and silicon doping on the performance of nanostructured hematite photoanodes for solar water splitting[J]. The Journal of Physical Chemistry C, 2008, 113(2): 772-782.
84. Saremi-Yarahmadi S, Wijayantha K G U, Tahir A A, et al. Nanostructured α-Fe_2O_3 electrodes for solar driven water splitting: effect of doping agents on

preparation and performance[J]. The Journal of Physical Chemistry C, 2009, 113(12): 4768-4778.

85. Zhang M, Luo W, Li Z, et al. Improved photoelectrochemical responses of Si and Ti codoped α-Fe_2O_3 photoanode films[J]. Applied Physics Letters, 2010, 97(4): 042105.
86. Zhang, Y.; Zhou, Z.; Chen, C.; Che, Y.; Ji, H.; Ma, W.; Zhang, J.; Song, D.; Zhao, J. Gradient $FeO_x(PO_4)_y$ layer on hematite photoanodes: novel structure for efficient light driven water oxidation[J]. 2014.
87. Grätzel M. Photoelectrochemical cells[J]. Nature, 2001, 414(6861): 338-344.
88. Cahill D G, Ford W K, Goodson K E, et al. Nanoscale thermal transport[J]. Journal of applied physics, 2003, 93(2): 793-818.
89. Chiam S Y, Kumar M H, Bassi P S, et al. Improving the efficiency of hematite nanorods for photoelectrochemical water splitting by doping with manganese[J]. ACS applied materials & interfaces, 2014, 6(8): 5852-5859.
90. Sivula K, Zboril R, Le Formal F, et al. Photoelectrochemical water splitting with mesoporous hematite prepared by a solution-based colloidal approach[J]. Journal of the American Chemical Society, 2010, 132(21): 7436-7444.
91. Momeni M M, Ghayeb Y, Mohammadi F. Solar water splitting for hydrogen production with Fe_2O_3 nanotubes prepared by anodizing method: effect of anodizing time on performance of Fe_2O_3 nanotube arrays[J]. Journal of Materials Science: Materials in Electronics, 2015, 26(2): 685-692.
92. Frites M, Shaban Y A, Khan S U M. Iron oxide (n-Fe_2O_3) nanowire films and carbon modified (CM)-n-Fe_2O_3 thin films for hydrogen production by photosplitting of water[J].
93. International Journal of Hydrogen Energy, 2010, 35(10): 4944-4948.Grigorescu S, Lee C Y, Lee K, et al. Thermal air oxidation of Fe: rapid hematite nanowire growth and photoelectrochemical water splitting performance[J]. Electrochemistry Communications, 2012, 23: 59-62.

Chapter 2 Experimental approach and principles

2.1 Fabrication methods of Fe_2O_3 nanowire arrays

Several fabrication methods of Fe_2O_3 nanowire arrays have been reported recently [1-6]. Electrochemical deposition method is a popular method to fabricate nanowires [7-11]. In this method, anodic aluminium oxide (AAO) templates were used to form the nanowire or nanorod structure under the effect of electrochemical deposition, then removed the AAO template by using NaOH solution. For example, Mao et al. reported a work using this method to grow Fe_2O_3 nanorod on a Au nanorod substrate [12]. Vapor phase deposition method is another method to obtain Fe_2O_3 nanostructures [13-20], it includes physical vapor evaporation, chemical vapor deposition (CVD), atomic layer deposition, and reactive sputtering [21]. Chueh et al. has reported chemical vapor deposition method to obtain the aligned and uniform Fe_2O_3 nanowire array [22]. Solution based method can also be used to fabricate the Fe_2O_3 nanowires [23, 24]. For example, Ling et al. used hydrothemal method to synthesis the Fe_2O_3 nanowires and nanocorals [25]. Stress-induced atomic diffusion (SAD) is the also an important approach for the synthesis of Fe_2O_3 nanowire, since it could obtain the Fe_2O_3 nanowire array directly [26, 27]. Also this method could control the morphologies of Fe_2O_3 nanowires by simply changing the experiment parameters.

In this study, one of the research objectives is to find the optimize parameters of Fe_2O_3 nanowire array for solar water splitting application, therefore SAD method was used to fabricated Fe_2O_3 nanowire arrays. However, normally the density of Fe_2O_3 nanowire arrays fabricated based on this method is very low [26, 27], which cannot

satisfy the requirement of solar water splitting. In this study, water vapor environment and surface polishing treatment were introduced to improve SAD in order to increase the density of nanowires.

2.2 Evaluation methods of nanowire arrays

In order to find the optimized parameters of Fe_2O_3 nanowire array for water splitting application, the density, diameter and length of nanowire array were investigated in this study. In this section, the evaluation method of Fe_2O_3 nanowire arrays is described.

2.2.1 Density evaluation method

Figure 2.1 shows the evaluation method of nanowire array density in this study. First, the SEM image was divided to small square area with each side of 1 μm by the image processing software. Then several nonadjacent areas were chosen and the number of nanowires in each area was counted. After that the average density of all three area was calculated.

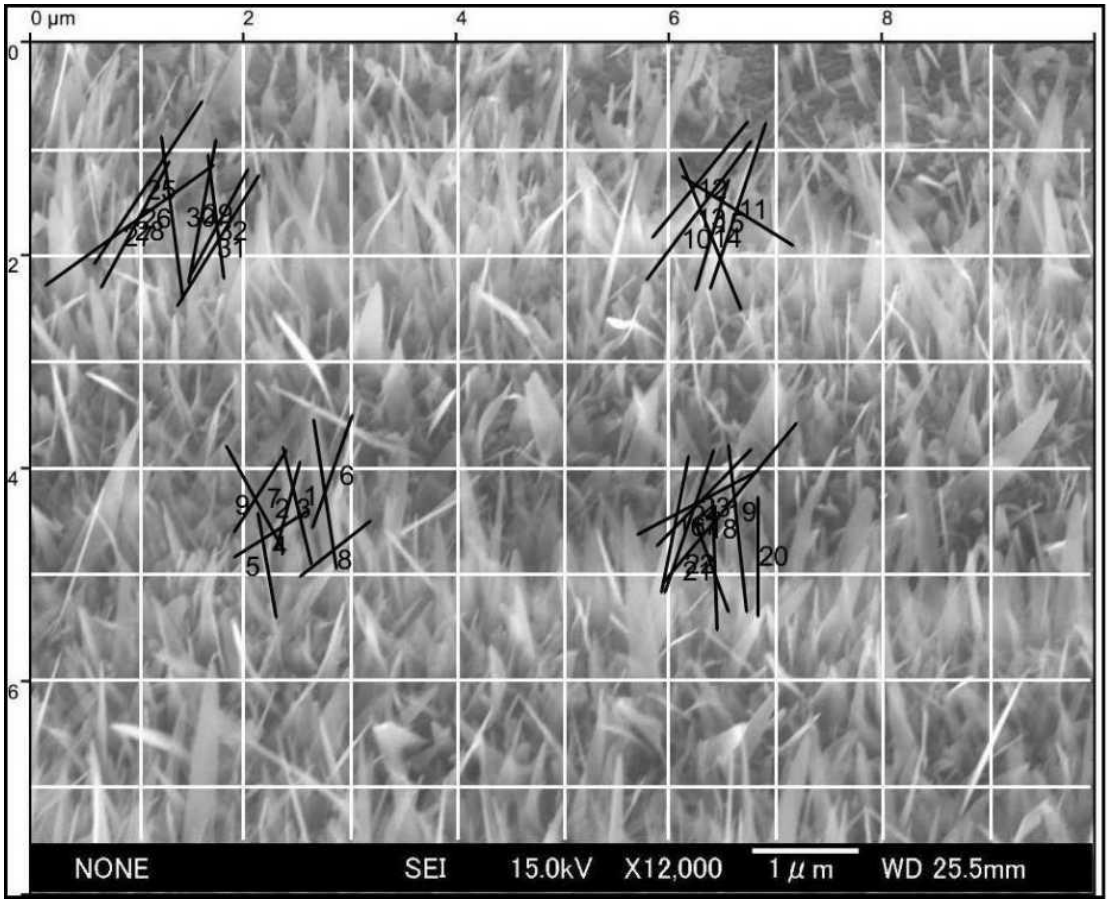

Fig. 2.1 Density evaluation by Gwyddion

2.2.2 Length evaluation method

The nanowire length will effect the light absorption and electron transfer path of the Fe_2O_3 nanowire array photoanode. In this study, we used a software of image processing (Gwyddion) to analyze the SEM image, as shown in Fig. 2.2. First, several nanowires were chosen randomly, then the length of each nanowire was measured by the software. After that all the length data has been collected and calculated to obtain the average length.

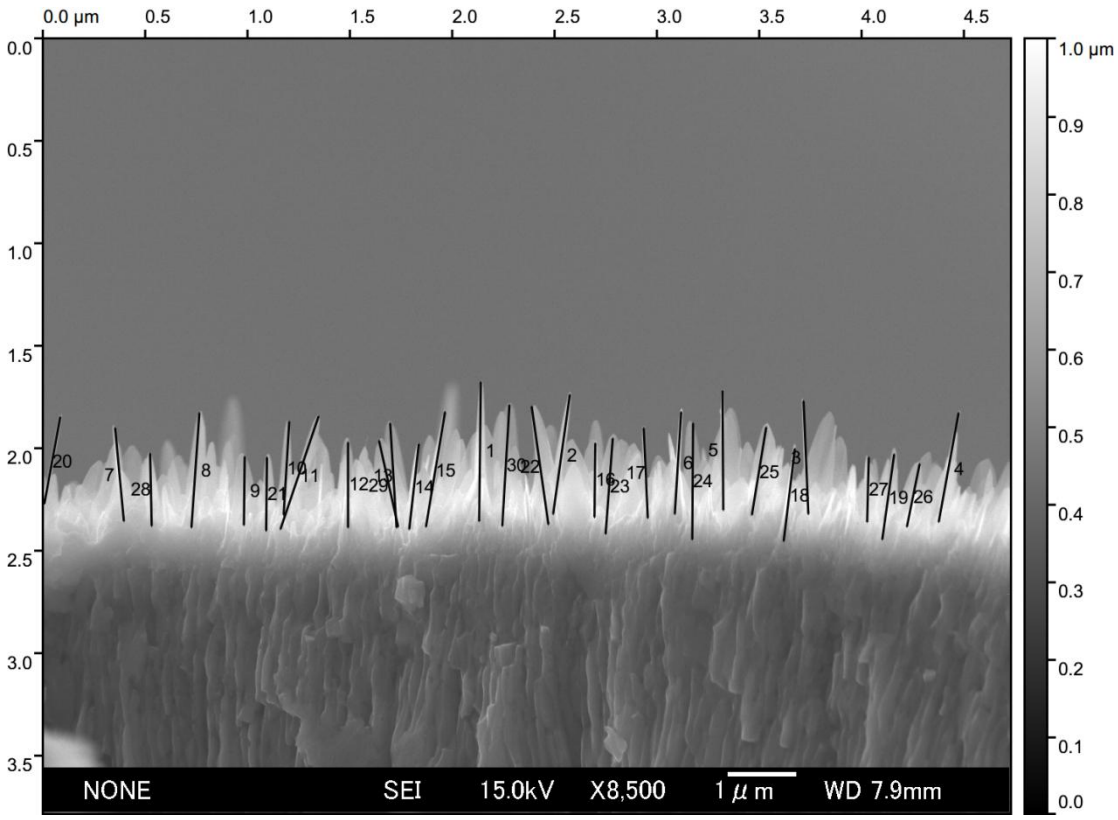

Fig. 2.2 Length evaluation by Gwyddion

2.2.3 Diameter evaluation method

The statistic of diameter has also been measured by using the same software, as shown in Fig. 2.3. It should be mentioned that since sometime the shape of nanowire is like a long triangle or oblong oval, the width from the middle part of the nanowire will be collected as the diameter. After that the average length was calculated from the collected data.

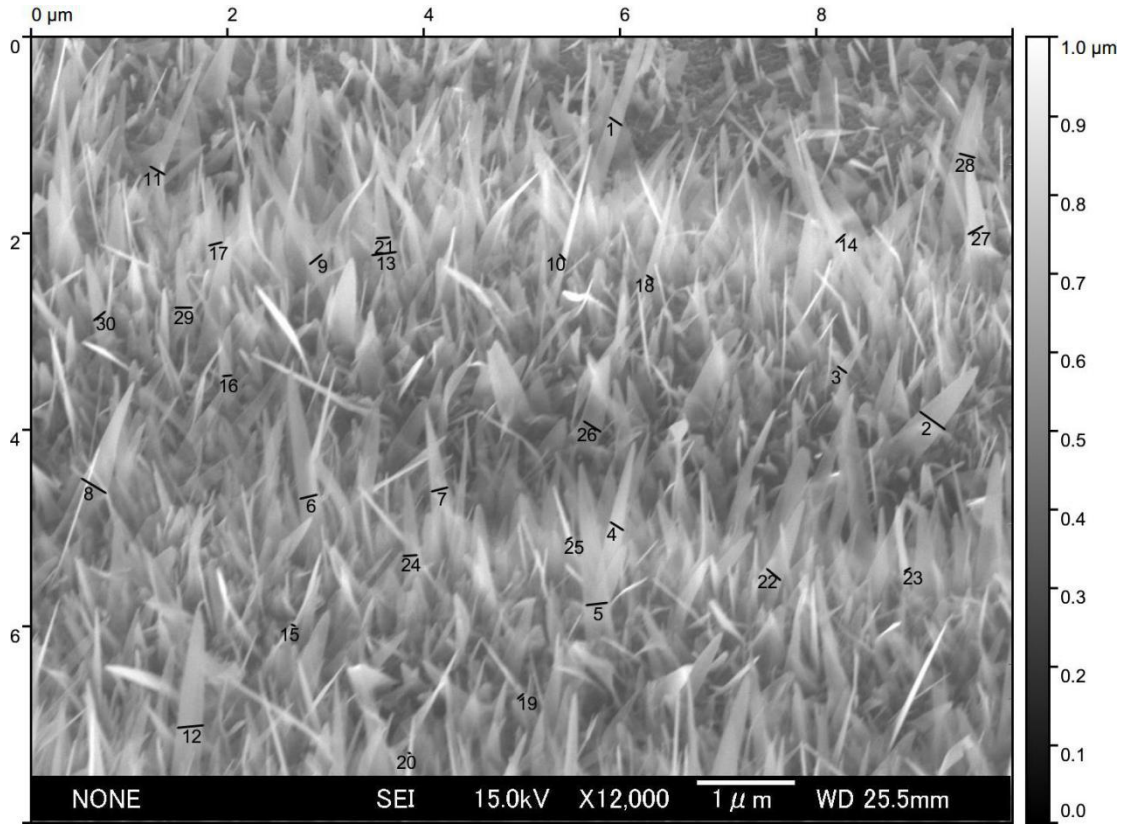

Fig. 2.3 Diameter evaluation by Gwyddion

2.3 Photoelectrochemical performance evaluation method

2.3.1 Design of the photoelectrode structure

In this study, the substrate of Fe_2O_3 nanowire array photoanode is iron plate. Since the structure of photoanode will effect the photoelectrochemical performance greatly, it is necessary to design an optimize structure of photoanode. For PEC measurements, such as the photocurrent measurement and the IPCE measurement, there is a basic requirement for the photoanode that only the semiconductor surface to be exposed to the light source and electrolyte. The procedures of how to assemble the Fe_2O_3 nanowire array photoanode are as follows.

1) Half of the side with the Fe_2O_3 nanowire array was polished with the sand paper until the pure iron inside the iron substrate was exposed, as shown in Fig. 2.4;

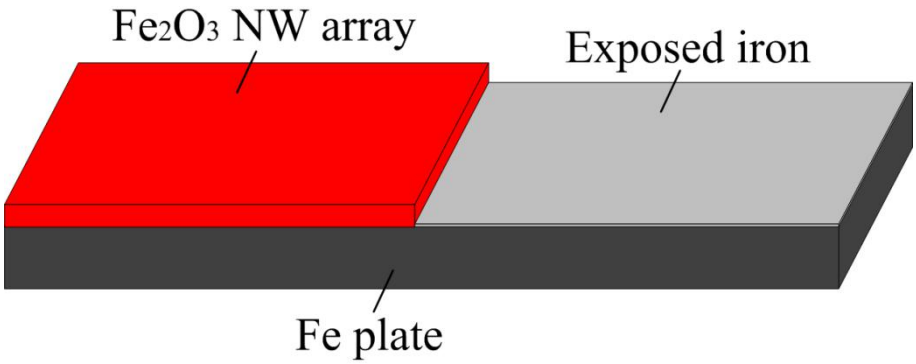

Fig. 2.4 First step of the photoanode assembling.

2) A copper wire with the diameter of 0.25 μm was polished to remove the oxide layer that may exist on the surface, and conducted with the Fe_2O_3 nanowire array at the polished part; a carbon tape was used to fixed the copper wire on the substrate, as shown in Fig .2.5.

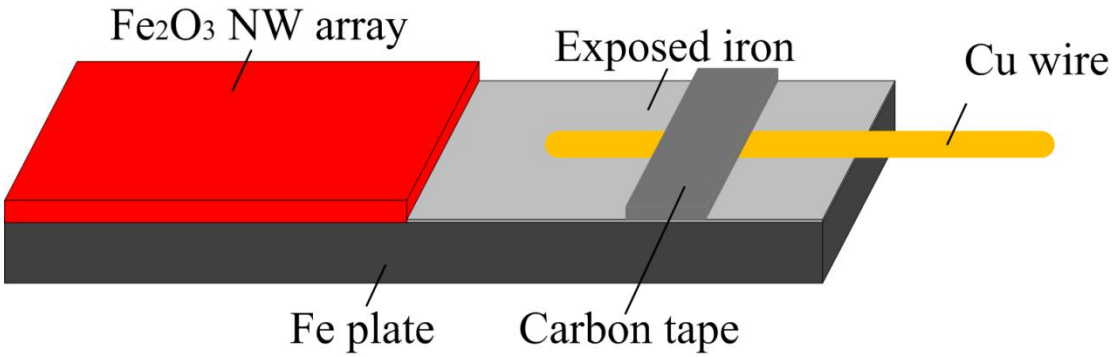

Fig. 2.5 Photoanode contact with the Cu wire.

3) After that a non-conductive adhesive was applied on the surface of carbon tape and copper wire to ensure that the conductive part will not contact with electrolyte.
4) After the assembling, the photoanode was put into an oven at 70 ^{o}C, until the adhesive dried.

2.3.2 Photocurrent density measurement

Photocurrent is an electric current produced by the photovoltaic effect from the photocatalyst, it can be determined by comparing the dark current and light current at the potential versus reference electrode. Photocurrent measurement was carried out using a three-electrode system, as shown in Fig. 2.6. The fabricated Fe_2O_3 nanowire array is used as the photoanode, the cathode is a Pt wire with a diameter of 0.05 mm, and Ag/AgCl is used as the reference electrode. These three electrodes were placed in a 1 mol/L NaOH solution. The light source is a quartz halogen fiber optic illuminator (Fiber-Lite PL800), the spectrum of the light source was measured as shown in Fig. 2.7, and the optical power density was measured to be 154 mW/cm^2 by a power meter (COHERENT LM-10).

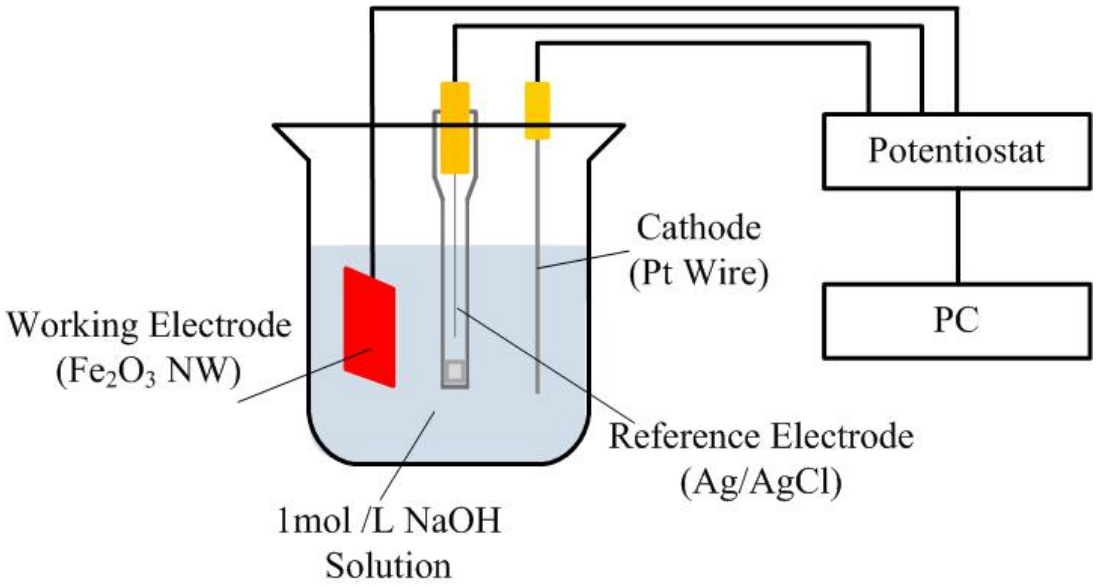

Fig. 2.6 Schematic of the three-electrode measurement system.

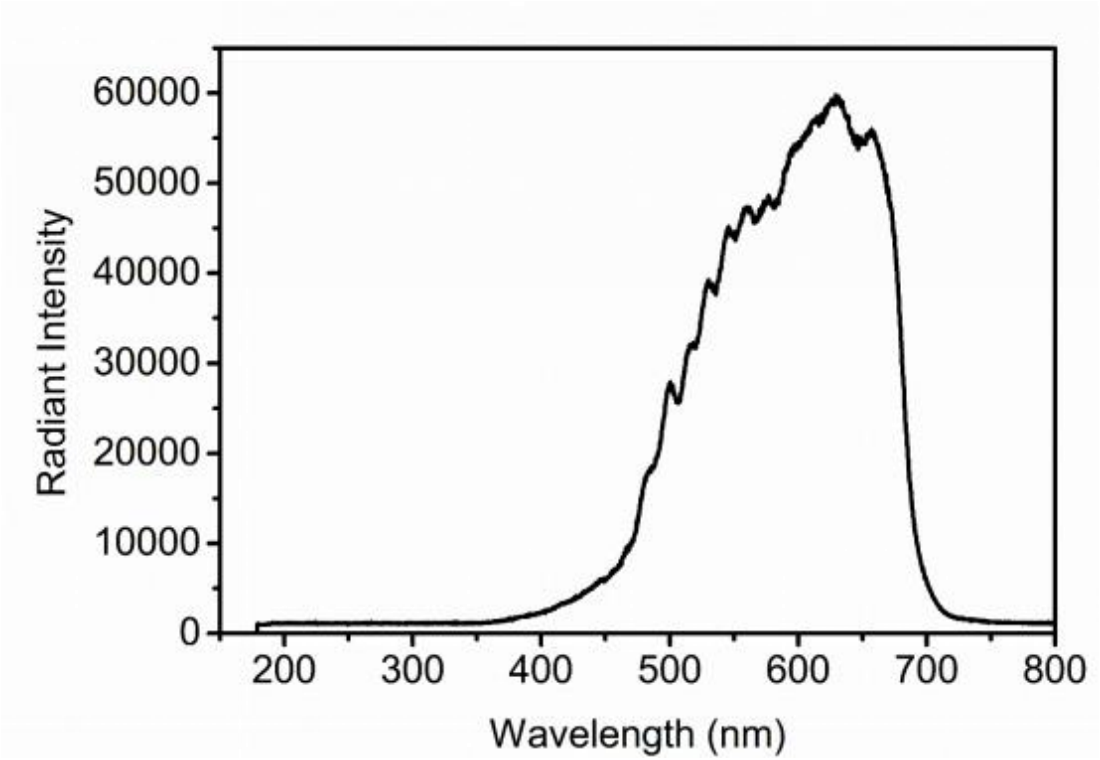

Fig. 2.7 Spectrum of the halogen light used in photocurrent density measurement.

2.3.3 IPCE measurements

The incident photon to electron conversion efficiency (IPCE) is another important parameter for the photocatalyst. The integration of the IPCE values over the AM 1.5G solar spectrum can provide the estimated maximum solar to hydrogen efficiency (STH) when they are measured under zero bias potential between the working and the counter electrodes. It can be measured from the photocurrent generated form monochromatic light. The definition of IPCE is shown in equation 2.1.

$$\mathrm{IPCE} = \frac{\mathrm{electrons}(cm^2/\mathrm{s})}{\mathrm{photons}(cm^2/\mathrm{s})} = \frac{J_{photo}(mA/cm^2)\times 1240(eV\,nm)}{P(mW/cm^2)\times\lambda(nm)}\times 100\%, \qquad (2.1)$$

where J_{photo} is the photocurrent density measured at the single wavelength light; P is the incident power density of light; λ is the wavelength of incident light. The number

1240 is the unit conversion factor (eV nm) from the product of the Plank constant and the speed of light. From the IPCE spectrum, an estimation of the total photocurrent under AM1.5 illumination can be obtained by integration over all the IPCE values for each wavelength through an important underlying assumption that there is a linear relationship between the monochromatic photocurrent and the light intensity.

IPCE measurements were performed using a Xe lamp with the single-wavelength filters from 400nm to 650nm. The light energy of the incident light from the lamp was measured with a power meter (COHERENT LM-10). All IPCE measurements were carried out with the applied bias of 0.234 V versus Ag/AgCl reference electrode (1.23 V vs. RHE).

2.3.4 Stability test

Photocorrosion in aqueous environment is one of the most significant obstacles to the widespread deployment of semiconductor materials as PEC devices for solar hydrogen production. The photogenerated holes and electrons in semiconductor electrodes are generally characterized by strong oxidizing and reducing potentials. In this study, in order to understand the stability of Fe_2O_3 nanowire array photoanode, a chopped light was used to measure the photo response during the light on and off situation.

2.4 Growth mechanism of Fe_2O_3 nanowire array

Stress induced atomic diffusion method can be divided into two ways to fabricate nanowires. One is thermal expansion method used to fabricated metallic nanowires such as Al [28], Ag[29] and Bi[30]. In this case, a metallic film and Si substrate structure is necessary. Due to the difference of thermal expansion coefficients, different expansions will introduce stress and stress gradient in the materials which will lead to atoms diffusion, thereby results the formation of nanowires, where the

nanowires grow from their tip [31]. The another is thermal oxidation method used to fabricate metal oxide nanowires such as CuO, ZnO and Fe_2O_3. In this case, only a metal plate is necessary. When a metal plate is heated in the air, an oxide layer will be formed at the top surface of the plate. Due to the molar volumes difference between the oxide layer and the plate, different volume expansions will occur in the two materials. Therefore, stress and stress gradient are induced. Thus, atoms diffusion will occur and the nanowires will be formed, where the nanowires grow from their base. The growth mechanism of Fe_2O_3 nanowires is described in detail as follows.

During the heating process, the top surface of the iron plate will be oxidized into Fe_2O_3, thus a two layer structure will be formed as shown in Fig. 2.8. The Fe_2O_3 layer suffered the compressive stress σ_x, $\sigma_y (= \sigma_x)$ generated in the Fe_2O_3/Fe interface due to the difference of volume expansion. Therefore, the compression hydrostatic stress σ [$\sigma = (\sigma_x + \sigma_y + \sigma_z)/3$, and $\sigma_z = 0$] is generated. Here, a rectangular coordinate system (*x, y, z*) is chosen where *z* is perpendicular to the top surface of the oxide layer. Because the top surface of the oxidized layer (Fe_2O_3 layer) is not restrained, the absolute value of compression hydrostatic stress at the top surface is smaller than that at the Fe_2O_3/Fe interface.

On the other hand, the top surface of Fe layer at the Fe_2O_3/Fe interface suffered the tensile stress due to the expansion of Fe_2O_3 layer. Because the bottom surface of Fe layer is not restrained, the tensile stress at the bottom surface of Fe layer is smaller than that at the Fe_2O_3/Fe interface. Therefore, the Fe atoms inside the Fe layer will diffuse along the direction from bottom surface to the Fe_2O_3/Fe interface.

Since the stress σ_x and σ_y are not continuous at the interface of Fe_2O_3/Fe, i.e. tensile in Fe and compressive in Fe_2O_3, the hydrostatic stress is discontinuity at the interface. After the Fe atoms diffuse into the Fe_2O_3 layer, they will continuously diffuse from the bottom to the top surface of Fe_2O_3 layer, as shown in Fig. 2.8.

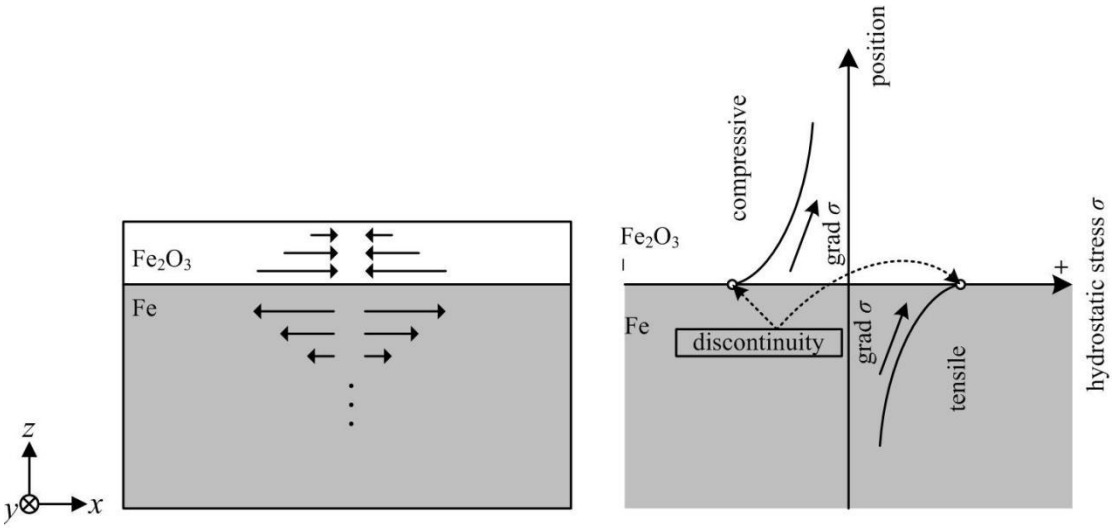

Fig. 2.8 Schematic illustrations of hydrostatic stress distribution in the two layers for explaining stress induced diffusion of Fe atoms.

Since the distribution of the hydrostatic stress, σ, is homogeneous in the x-y plane, the distribution of hydrostatic stress in the z direction results a stress gradient, gradσ, having a direction from the bottom of Fe plate to the top surface of Fe_2O_3 ($+z$ direction). The hydrostatic stress and its gradient can be considered to be the main factors to affect the diffusion of Fe atoms, which can be described by the following equation [32]:

$$J = \frac{N\Omega D_0}{kT} \exp\left[-\frac{(Q-\Omega\sigma)}{kT}\right] \mathrm{grad}\sigma \quad , \tag{2.2}$$

where J is the atomic flux, N the atomic concentration, Ω the atomic volume, k the Boltzmann's constant, T the absolute temperature, D_0 the self-diffusion coefficient, and Q the activation energy [33]. In this equation, gradσ can be considered as the driving force for the atoms diffusion, and the atomic flux has the same direction as gradσ.

References

1. Wen X, Wang S, Ding Y, et al. Controlled growth of large-area, uniform, vertically aligned arrays of α-Fe_2O_3 nanobelts and nanowires[J]. The Journal of Physical Chemistry B, 2005, 109(1): 215-220.
2. Chen J S, Zhu T, Yang X H, et al. Top-down fabrication of α-Fe_2O_3 single-crystal nanodiscs and microparticles with tunable porosity for largely improved lithium storage properties[J]. Journal of the American Chemical Society, 2010, 132(38): 13162-13164.
3. Cao X, Wang N. A novel non-enzymatic glucose sensor modified with Fe_2O_3 nanowire arrays[J]. Analyst, 2011, 136(20): 4241-4246.
4. Chen Z, Cvelbar U, Mozetic M, et al. Long-range ordering of oxygen-vacancy planes in α-Fe_2O_3 nanowires and nanobelts[J]. Chemistry of Materials, 2008, 20(9): 3224-3228.
5. Xue D S, Gao C X, Liu Q F, et al. Preparation and characterization of haematite nanowire arrays[J]. Journal of Physics: Condensed Matter, 2003, 15(9): 1455.
6. Lin Y, Sun F Q, Yuan X Y, et al. Sol–gel electrophoretic deposition and optical properties of Fe_2O_3 nanowire arrays[J]. Applied Physics A: Materials Science & Processing, 2004, 78(8): 1197-1199.
7. Liu L, Lee W, Huang Z, et al. Fabrication and characterization of a flow-through nanoporous gold nanowire/AAO composite membrane[J]. Nanotechnology, 2008, 19(33): 335604.
8. Wang X, Wang X, Huang W, et al. Sol-gel template synthesis of highly ordered MnO_2 nanowire arrays[J]. Journal of Power Sources, 2005, 140(1): 211-215.
9. Yin A J, Li J, Jian W, et al. Fabrication of highly ordered metallic nanowire arrays by electrodeposition[J]. Applied Physics Letters, 2001, 79(7): 1039-1041.
10. Zhou Y, Shen C, Li H. Synthesis of high-ordered LiCoO2 nanowire arrays by AAO template[J]. Solid State Ionics, 2002, 146(1): 81-86.
11. Sun X Y, Xu F Q, Li Z M, et al. Cyclic voltammetry for the fabrication of high

dense silver nanowire arrays with the assistance of AAO template[J]. Materials Chemistry and Physics, 2005, 90(1): 69-72.

12. Mao A, Han G Y, Park J H. Synthesis and photoelectrochemical cell properties of vertically grown α-Fe_2O_3 nanorod arrays on a gold nanorod substrate[J]. Journal of Materials Chemistry, 2010, 20(11): 2247-2250.
13. J. A. Glasscock, P. R. F. Barnes, I. C. Plumb and N. Savvides, Enhancement of photoelectrochemical hydrogen production from hematite thin films by the introduction of Ti and Si, J. Phys. Chem. C, 2007, 111, 16477–16488.
14. Y. Lin, S. Zhou, S. W. Sheehan and D. Wang, Nanonet-based hematite heteronanostructures for efficient solar water splitting, J. Am. Chem. Soc., 2011, 133, 2398–2401.
15. J. J. Wu, Y. L. Lee, H. H. Chiang and D. K. P. Wong, Growth and magnetic properties of oriented α-Fe_2O_3 nanorods, J. Phys. Chem. B, 2006, 110, 18108–18111.
16. M. L. Zhang, W. J. Luo, Z. S. Li, T. Yu and Z. G. Zou, Improved photoelectrochemical responses of Si and Ti codoped α-Fe_2O_3 photoanode films, Appl. Phys. Lett., 2010, 97, 3.
17. A. Kay, I. Cesar and M. Gratzel, New benchmark for water photooxidation by nanostructured α-Fe_2O_3 films, J. Am. Chem. Soc., 2006, 128, 15714–15721.
18. I. Cesar, K. Sivula, A. Kay, R. Zboril and M. Graetzel, Influence of feature size, film thickness, and silicon doping on the performance of nanostructured hematite photoanodes for solar water splitting, J. Phys. Chem. C, 2009, 113, 772–782.
19. S. D. Tilley, M. Cornuz, K. Sivula and M. Gratzel, Light-Induced water splitting with hematite: improved nanostructure and iridium oxide catalysis, Angew. Chem., Int. Ed., 2010, 49, 6405–6408.
20. K. Sivula, F. Le Formal and M. Gratzel, WO_3-Fe_2O_3 photoanodes for water splitting: a host scaffold, guest absorber approach, Chem. Mater., 2009, 21, 2862–2867.
21. Wheeler D A, Wang G, Ling Y, et al. Nanostructured hematite: synthesis, characterization, charge carrier dynamics, and photoelectrochemical properties[J].

Energy & Environmental Science, 2012, 5(5): 6682-6702.

22. Chueh Y L, Lai M W, Liang J Q, et al. Systematic Study of the Growth of Aligned Arrays of α-Fe_2O_3 and Fe_3O_4 Nanowires by a Vapor-Solid Process[J]. Advanced Functional Materials, 2006, 16(17): 2243-2251.
23. L. Vayssieres, N. Beermann, S. E. Lindquist and A. Hagfeldt, Controlled aqueous chemical growth of oriented three-dimensional crystalline nanorod arrays: application to iron(III) oxides, Chem. Mater., 2001, 13, 233–235.
24. R. Wang, Y. Chen, Y. Fu, H. Zhang and C. Kisielowski, Bicrystalline hematite nanowires, J. Phys. Chem. B, 2005, 109, 12245–12249.
25. Y. C. Ling, G. M. Wang, D. A. Wheeler, J. Z. Zhang and Y. Li, Sn-Doped hematite nanostructures for photoelectrochemical water splitting, Nano Lett., 2011, 11, 2119–2125.
26. Cvelbar U, Chen Z, Sunkara M K, et al. Spontaneous Growth of Superstructure α-Fe_2O_3 Nanowire and Nanobelt Arrays in Reactive Oxygen Plasma[J]. Small, 2008, 4(10): 1610-1614.
27. Yuan L, Wang Y, Cai R, et al. The origin of hematite nanowire growth during the thermal oxidation of iron[J]. Materials Science and Engineering: B, 2012, 177(3): 327-336.
28. Shingubara S, Okino O, Sayama Y, et al. Two-dimensional nanowire array formation on Si substrate using self-organized nanoholes of anodically oxidized aluminum[J]. Solid-State Electronics, 1999, 43(6): 1143-1146.
29. Xu F, Zhu Y. Highly conductive and stretchable silver nanowire conductors[J]. Advanced materials, 2012, 24(37): 5117-5122.
30. Shim W, Ham J, Lee K, et al. On-film formation of Bi nanowires with extraordinary electron mobility[J]. Nano letters, 2008, 9(1): 18-22.
31. Chen M, Yue Y, Ju Y. Growth of metal and metal oxide nanowires driven by the stress-induced migration[J]. Journal of Applied Physics, 2012, 111(10): 104305.
32. Saka M, Yamaya F, Tohmyoh H. Rapid and mass growth of stress-induced nanowhiskers on the surfaces of evaporated polycrystalline Cu films[J]. Scripta materialia, 2007, 56(12): 1031-1034.

33. Korhonen M A, Borgesen P, Tu K N, et al. Stress evolution due to electromigration in confined metal lines[J]. Journal of Applied Physics, 1993, 73(8): 3790-3799.

Chapter 3 Fabrication of high density Fe_2O_3 nanowire array and its photoelectrochemical properties

3.1 Introduction

In last chapter, we have mentioned that there are several methods to synthesis Fe_2O_3 nanowire arrays. By using the SAD method, Fe_2O_3 nanowire arrays can be obtained by heating a high-purity iron substrate under ambient conditions, which is a simple and low-cost method. However, because the density of such nanowire arrays fabricated by traditional method is not high enough, they are unfavorable for solar water splitting. In this chapter, a new method is proposed to synthesize high-density Fe_2O_3 nanowire arrays on an iron plate, under low-temperature conditions used for solar water splitting. In the presence of water vapor, surface oxidation was promoted during the heating process, thereby enhancing the driving force induced by stress gradient due to the expansion of the oxidation layer. Consequently, it is possible to fabricate high-density Fe_2O_3 nanowire arrays at a relatively low temperature (450 ^oC) compared to that used in the traditional method (500-800 ^oC) [1, 2].

3.2 Fabrication of high density Fe_2O_3 nanowire arrays

3.2.1 Sample preparation

Commercial iron plate with the purity of 99.95% was used as the substrate for

the nanowire fabrication. The thickness of the iron plate is 0.1 mm and the size of each substrate is 10 mm × 10 mm, as shown in Fig. 3.1. All the samples was cleaned by the ultrasonic cleaner (AS ONE ASU-2D) before experiment.

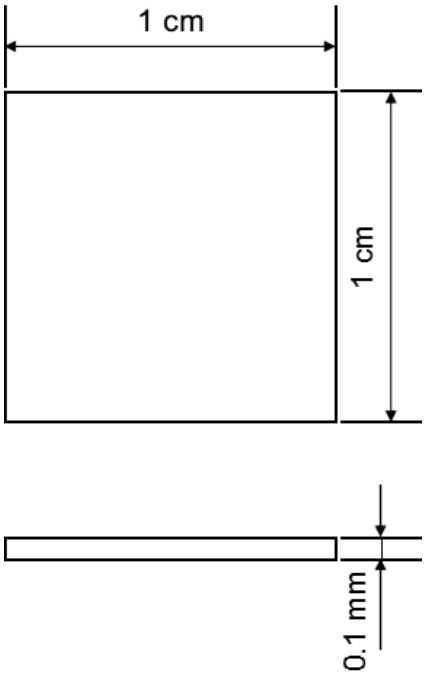

Fig. 3.1 Size of the iron plate.

3.2.2 Experimental conditions

The iron plate was heated by a ceramic heater in the atmosphere of water vapor. In order to find the best conditions for the nanowire array fabrication, some key parameters are investigated, which include the heating temperature, heating time, water vapor volume, and the duration of heating.

Heating temperature was set between 250 and 700 ^{o}C, as shown in Table 3.1. A humidifier was used to provide the water vapor condition, with a gas flow rate ranging from 0.2 L/h to 1.25 L/h, as shown in Table 3.2. Heating time of the iron plate on the ceramic heater was set to 30, 60, and 90 min, respectively, as shown in Table 3.3. After the fabrication, all the samples were analyzed by scanning electron microscopy (SEM, JSM-7000FK) and X-ray diffraction (XRD).

Table 3.1 Experimental conditions: Different heating temperatures.

No.	Heating time (min)	Temperature (°C)	Water vapor volume (L/h)
1	90	250	0.2
2		350	
3		450	
4		500	
5		600	
6		700	

Table 3.2 Experimental conditions: Different water vapor volumes.

No.	Heating time (min)	Heating temperature (°C)	Water vapor volume (L/h)
7	90	450	0.2
8			1
9			1.25

Table 3.3 Experimental conditions: Different heating times.

No.	Heating time (min)	Heating temperature (°C)	Water vapor volume (L/h)
10	30	450	0.2
11	60		
12	90		

3.3 Evaluations

3.3.1 Morphology of high density Fe_2O_3 nanowire array

Figure 3.2 to 3. 7 show the SEM images of the nanowire arrays fabricated at different heating temperatures under the conditions shown in Table 3.1. It can be inferred from the SEM images that the morphologies of the nanowires are different under different temperatures, besides the density, length, and diameters of the nanowires. The nanowires heated at 350, 450, and 500 ^{o}C (Fig. 3.3 to Fig. 3.5) are cone-shaped and those heated at 600 ^{o}C (Fig. 3.6) and 700 ^{o}C (Fig. 3.7) are wire-shaped. Similar morphologies are observed for a given temperature, indicating that the heating temperature affects the morphology of the nanowire.

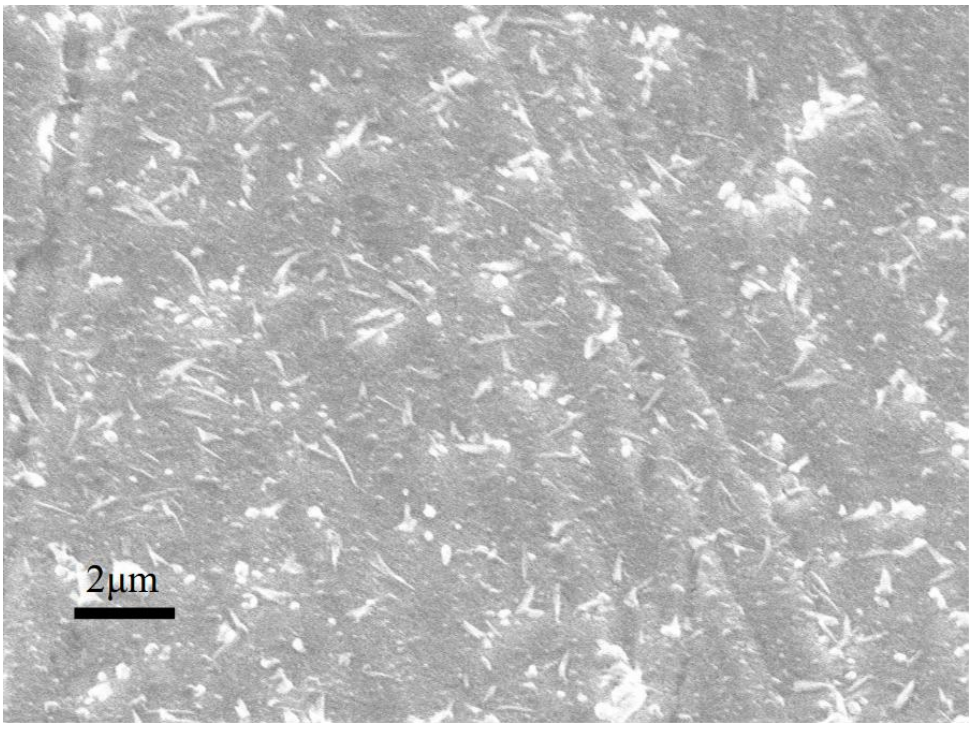

Fig. 3.2 Nanowire arrays heated at 250 ^{o}C.

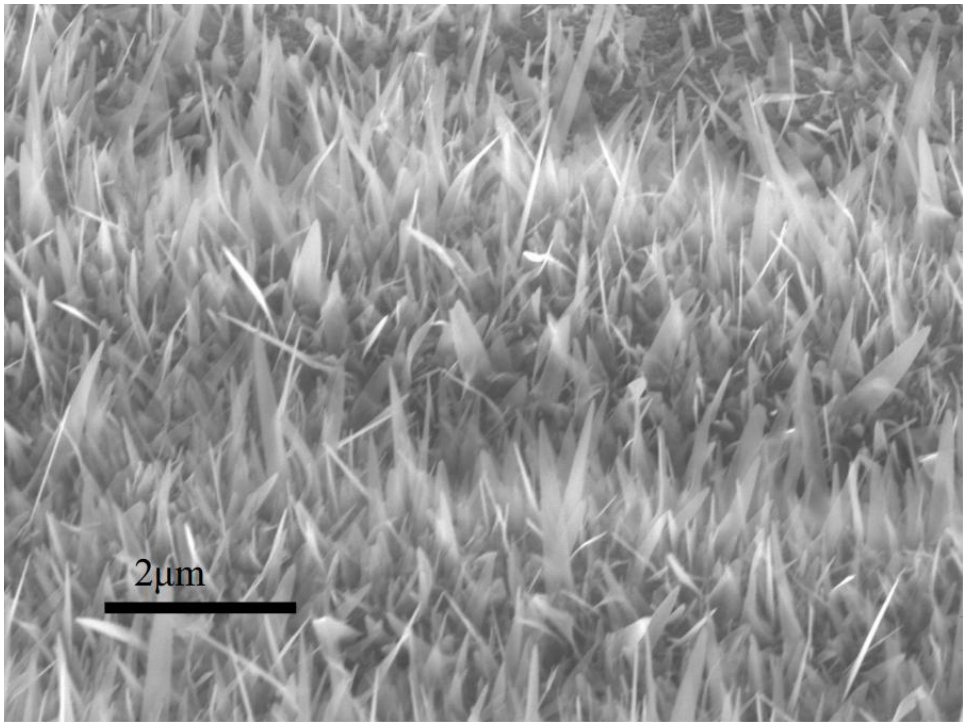

Fig. 3.3 Nanowire arrays heated at 350 ºC.

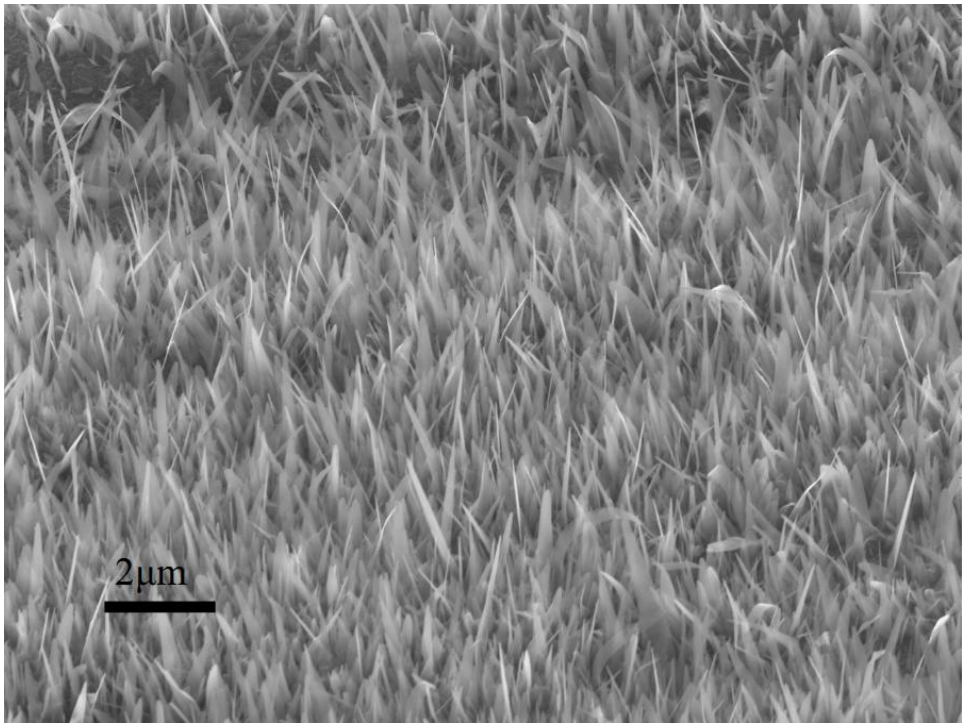

Fig. 3.4 Nanowire arrays heated at 450 ºC.

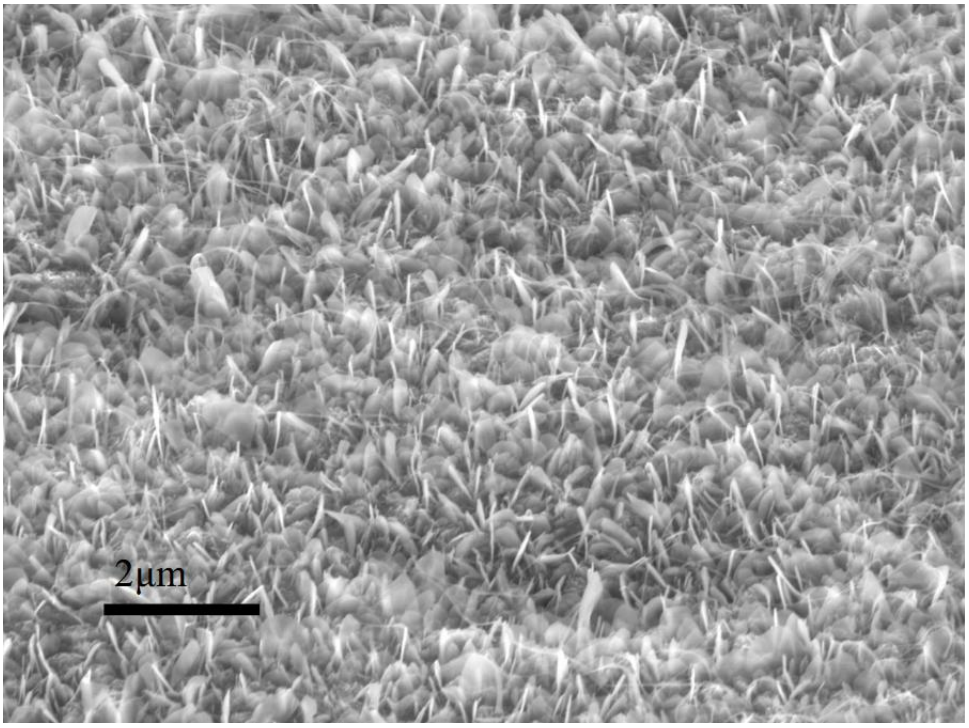

Fig. 3.5 Nanowire arrays heated at 500 °C.

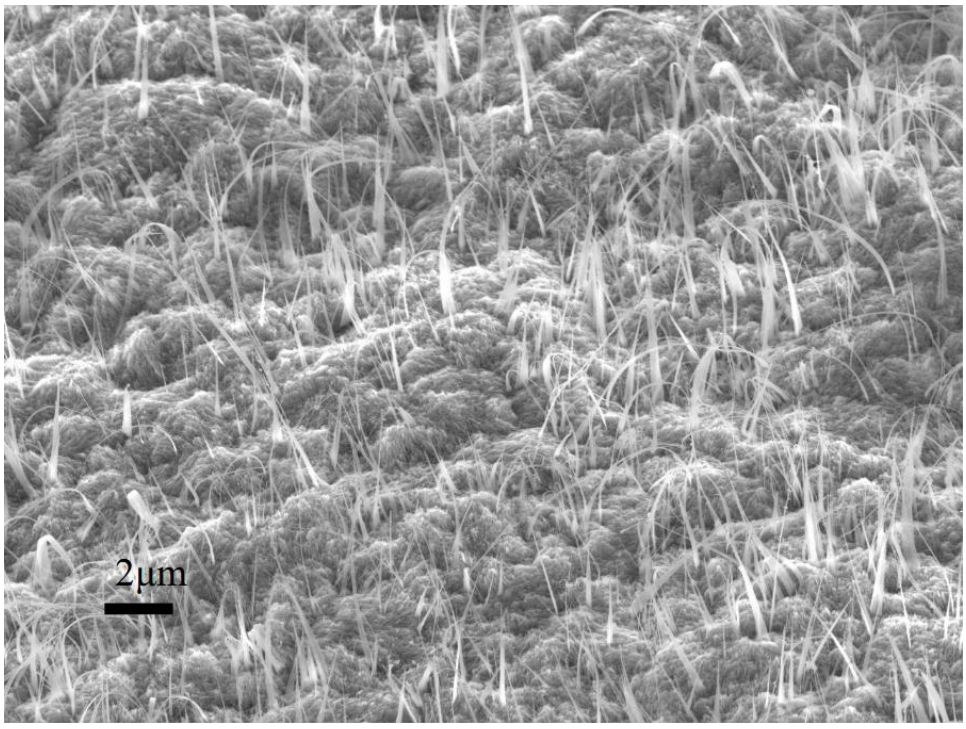

Fig. 3.6 Nanowire arrays heated at 600 °C.

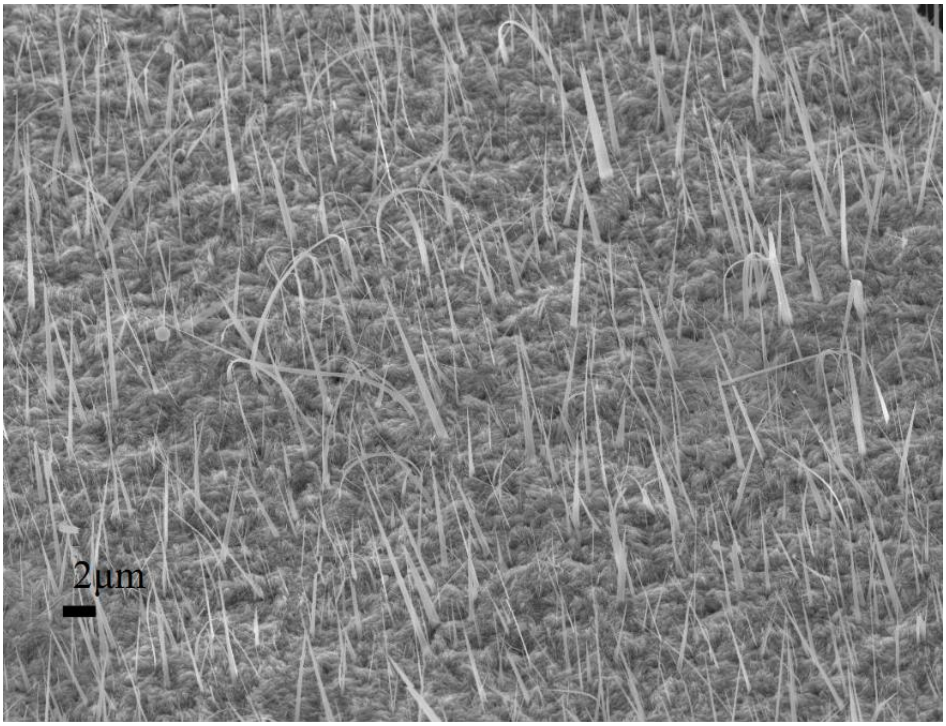

Fig. 3.7 Nanowire arrays heated at 700 °C.

The density of the nanowires is a key factor affecting the efficiency of the solar-hydrogen energy cycle. A comparison of the density of the nanowire arrays fabricated at different temperatures is shown in Fig. 3.8. The largest density of 14.3 wire/μm^2 is achieved for the sample heated at 450 °C. When the iron plate was heated at 250 °C, only a small quantity of the nanowires could be observed on the sample surface. With the increase in the heating temperature, the density of the nanowire array increased up to 450 °C. However, it decreased for temperatures above 450 °C. The density is only 1 wire/μm^2 at 700 °C.

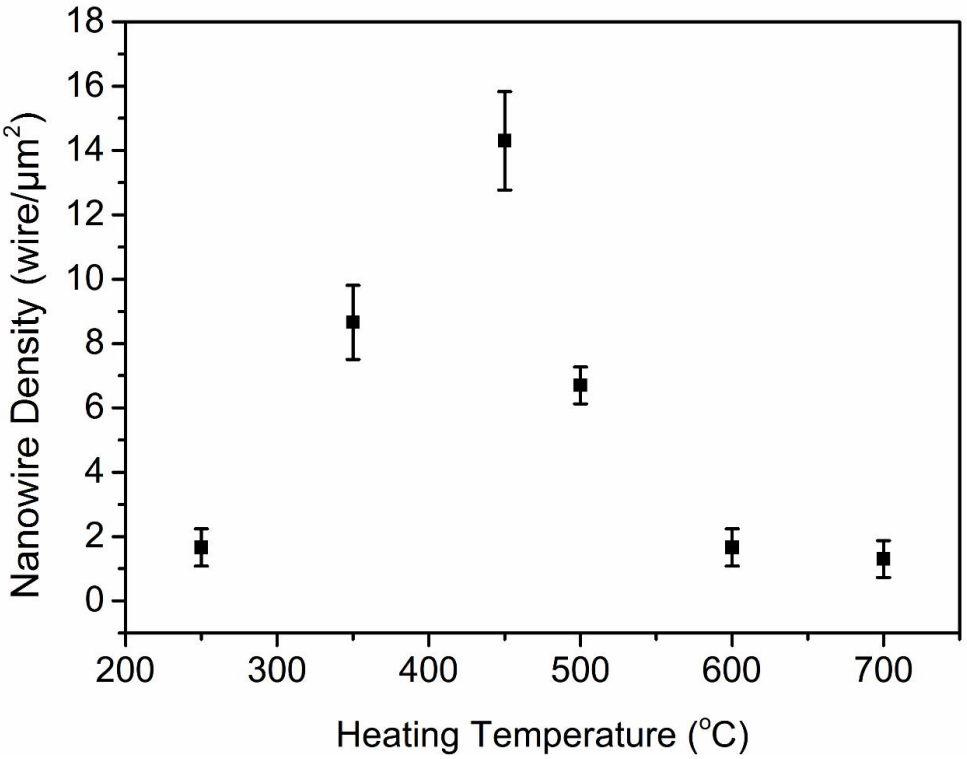

Fig. 3.8 Density statistic of the Fe_2O_3 nanowires obtained at different temperatures.

The length and diameter statistics of the nanowires obtained at different temperatures are shown in Figs. 3.9 and 3.10, respectively. With the increase in the heating temperature, the average length of the nanowires increased, and the longest nanowires of 9.98 μm average lengths were obtained at 700 °C. Figure 3.10 shows the diameter statistic of the nanowires fabricated at different temperatures. Diameters of the nanowires are also considered as an important factor affecting the efficiency of solar to hydrogen energy conversion; nanowires with larger diameters could absorb more light than those with small diameters, which could eventually improve the conversion efficiency. Unlike the variation in the average length, the average diameter of the nanowires decreases with the increase in heating temperature. The largest average diameter of 300 nm was obtained for nanowires fabricated at 250 °C.

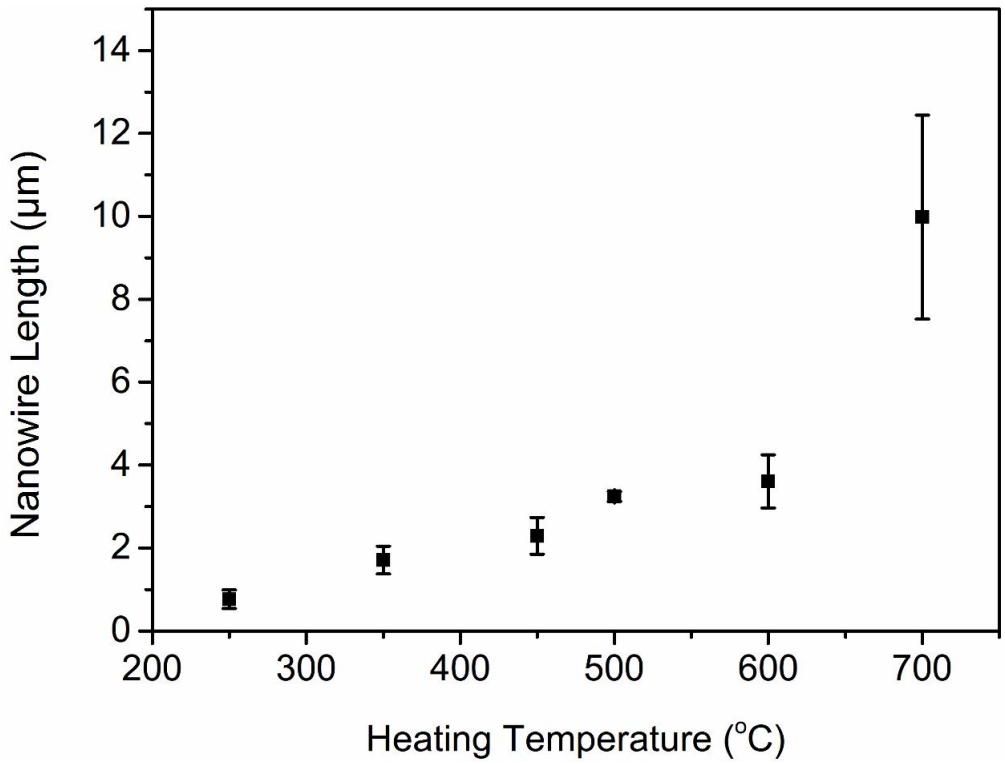

Fig. 3.9 Length statistic of the Fe_2O_3 nanowires obtained at different temperatures.

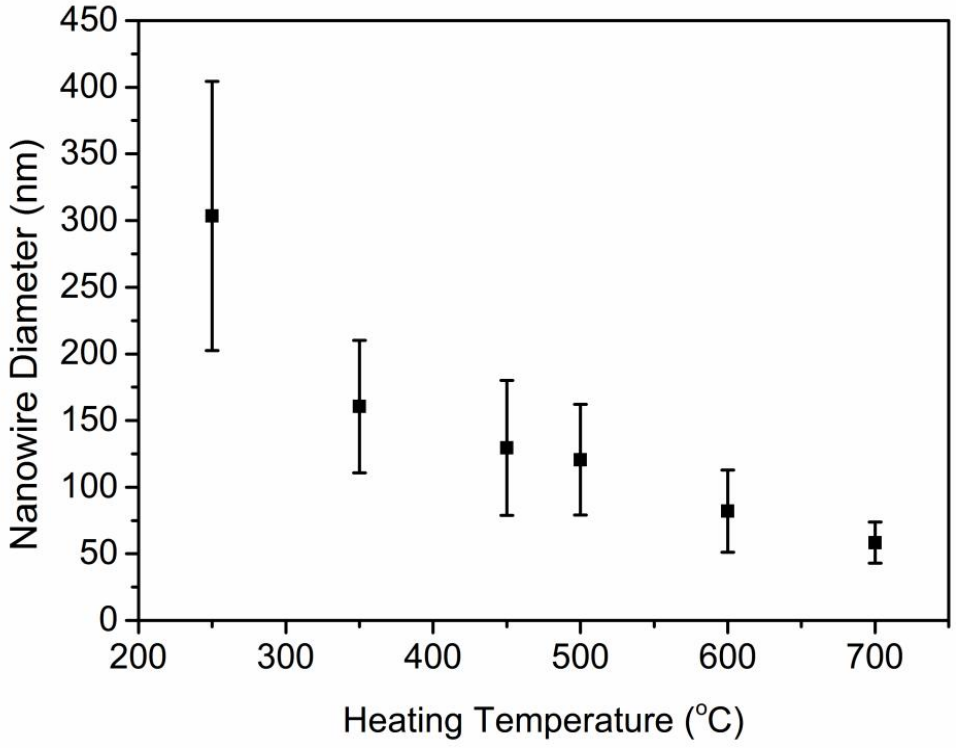

Fig. 3.10 Diameter statistic of the Fe_2O_3 nanowires obtained at different temperatures.

The cross section of the fabricated sample has also observed by using the

FESEM, as shown in Fig. 3.11. Three layers can be easily observed from the SEM image, which include the nanowire layer, the oxide layer and the iron layer. The shape of nanowires looks like grass (see Fig. 3.3), which indicated that nanowires grew from the top of themselves with the precipitation of diffused Fe atoms and their oxidation.

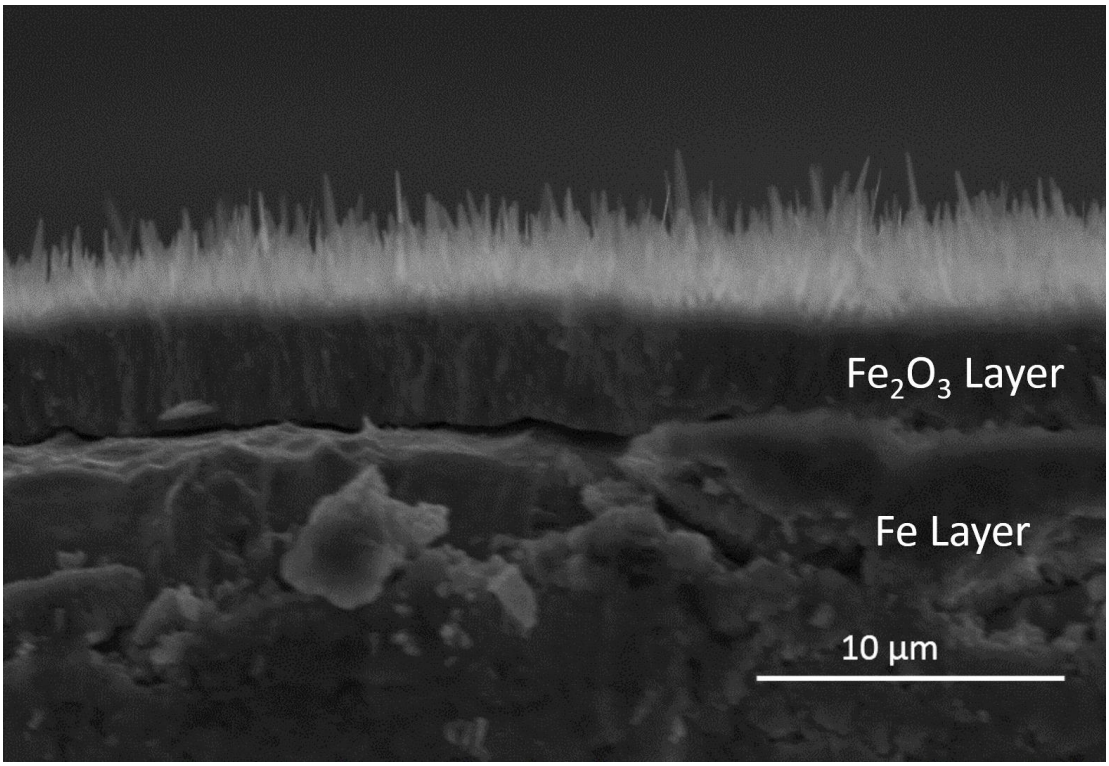

Fig. 3.11 SEM cross section observation of the Fe_2O_3 nanowire sample.

3.3.2 Water vapor effect on nanowire growth

The effect of the water vapor volume on the nanowire growth was also investigated in this study. The volume of the water vapor was set to be 0.2, 1, and 1.25 L/h, respectively, as shown in Table 3.2. From the SEM images shown in Fig. 3.12, it can be easily observed that the density of the nanowires decreased with an increase in the water vapor volume.

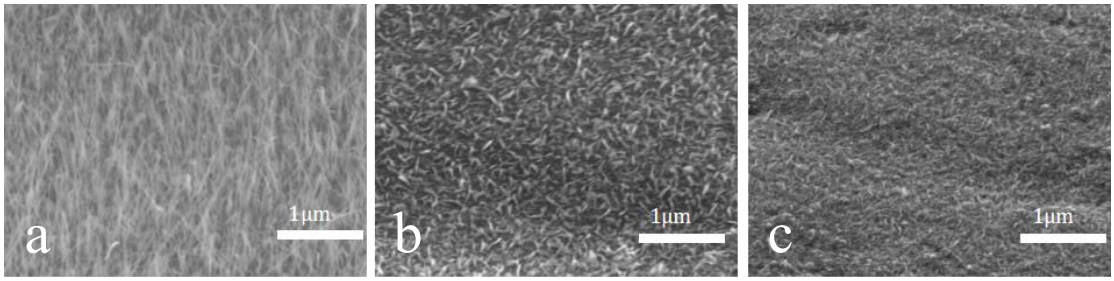

Fig. 3.12 SEM micrographs of the Fe_2O_3 nanowire arrays for samples heated at 450 °C with different water vapor volumes: (a) 0.2; (b) 1; and (c) 1.25 L/h.

3.3.3 Heating time effect on nanowire growth

Figure 3.13 shows the results of the iron samples heated for 30, 60, and 90 min, respectively, under the conditions listed in Table 3.3.

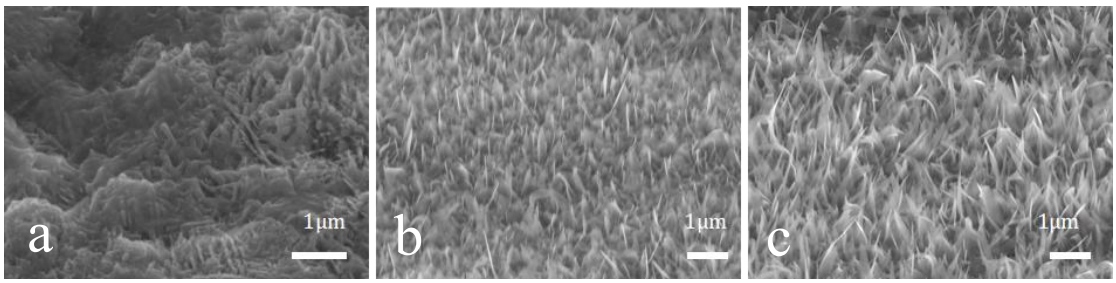

Fig. 3.13 SEM micrographs of the Fe_2O_3 nanowire arrays fabricated at 450 °C for different heating durations: (a) 30; (b) 60; and (c) 90 min.

When the sample was heated for a very short duration, some weak spots were generated on the iron plate surface, without any nanowire growth (Fig. 3.13(a)). In the

sample heated for 60 min (Fig. 3.13(b)), nanowires were formed, but with very different lengths and the density was lower than that of the sample heated for 90 min, as shown in Fig. 3.13(c). The nanowires had the highest density when the sample was heated for 90 min. The experiments were also carried out with longer heating times, 120 and 150 min, but this did not increase the density of the nanowire array.

3.3.4 Fe_2O_3 nanowire characterization

Figure 3.14 shows the XRD patterns of the nanowire arrays obtained for different heating temperatures under the water vapor condition of 0.2 L/h and heating time of 90 min. From data obtained from different samples, it can be inferred that when the heating temperature is higher than 450 ^oC, the formed Fe_2O_3 layer on Fe substrate is thicker than that formed at 450 ^oC. By comparing the densities of the nanowire arrays, it is considered that although the heating temperature of over 500 ^oC could provide a larger compressive stress in oxidation layer to increase the diffusion of the Fe atoms, the formed thicker oxidation layer will hinder the growth of the nanowires, due to the decrease of stress gradient in Fe_2O_3 layer. Therefore, low density nanowire arrays were obtained at relative high temperatures. In the case of the sample heated at 450 ^oC, the oxidization rate of the iron plate surface is optimal, generating enough compressive stress in Fe_2O_3 layer, and the stress gradient is also large enough to make the Fe atoms diffuse.

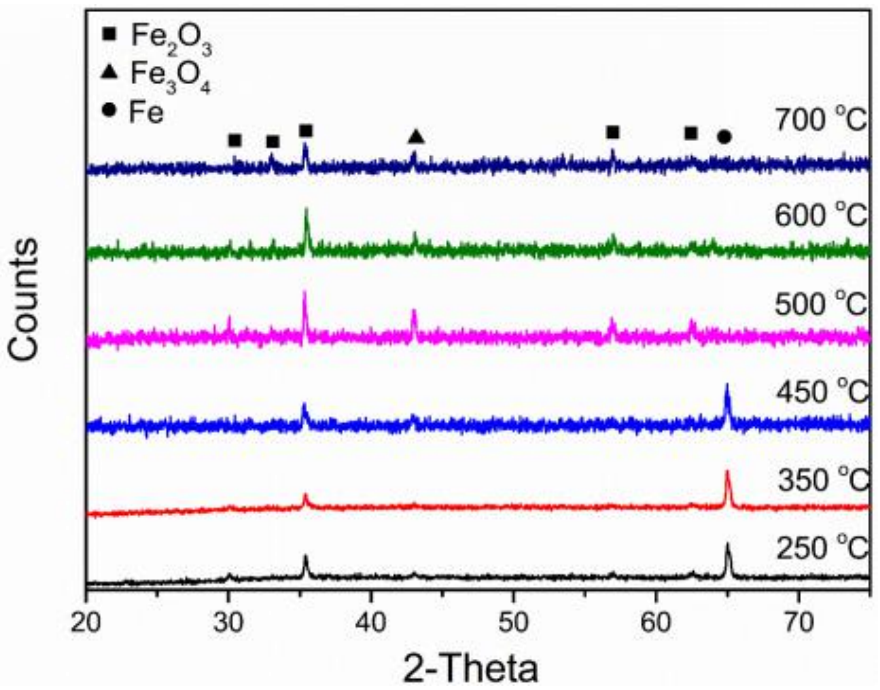

Fig. 3.14 XRD patterns of the Fe_2O_3 nanowire arrays at different temperatures.

3.4 PEC performance evaluation of high density Fe_2O_3 nanowire array

3.4.1 Photocurrent of high density Fe_2O_3 nanowire array

The photovoltaic properties of the nanowires have been investigated using a three-electrode system (Fig. 2.6), and the results are shown in Fig. 3.15. The Fe_2O_3 nanowire photoanode fabricated at 350 °C showed the largest photocurrent density among all the photoanodes, 0.65 mA/cm^2 at 1.23V vs. RHE. Although the nanowire photoanode fabricated at 450 °C has the largest density of nanowires, the photocurrent density is lower at 0.47 mA/cm^2, due to the smaller average diameter of the nanowires (127 nm), comparing with that of the nanowires fabricated at 350 °C (161 nm). The samples heated at 250, 500, 600, and 700 °C show very small photocurrent values, possibly owing to the poor nanowire density.

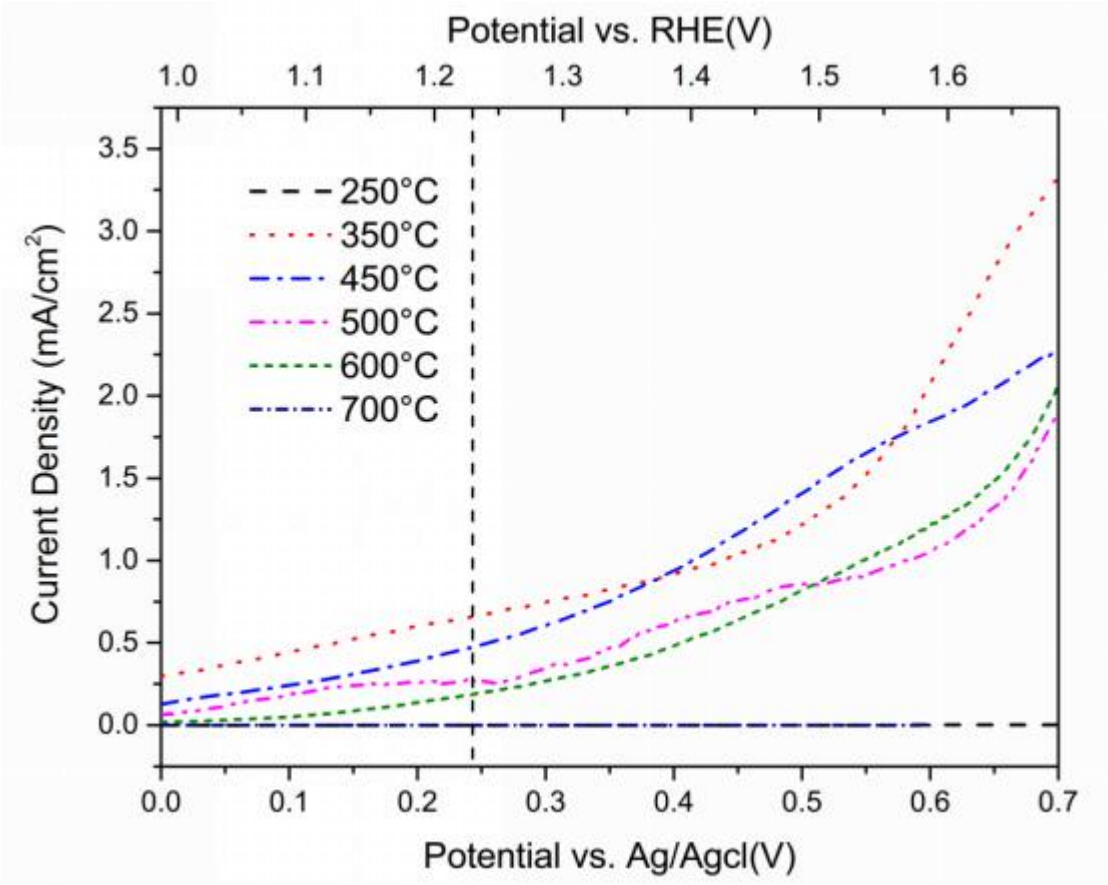

Fig. 3.15 Photocurrent densities from the nanowire array anodes obtained at different heating temperatures.

3.4.2 Incident photon-to-electron conversion efficiency of high density Fe_2O_3 nanowire array

The incident-photon-to-current efficiency (IPCE) of the nanowire photoanode fabricated at 450 ºC was measured to confirm the performance of water splitting, as shown in Fig. 3.16. The IPCE decreased with the increase of wavelength, and the maximum value is 5.54% at 400nm wavelength. This value is relative high than that of other pure Fe_2O_3 photoanodes without any functional modification, reported by the literatures, such as the Fe_2O_3 film with the IPCE of 2% at 400 nm [3], and Fe_2O_3 nanorods with the IPCE of 1.3% at 400 nm [4]. It should be mentioned that the IPCE value could be remarkably improved by functional modification of the Fe_2O_3

nanowire array. It has been reported that the Pt-doped Fe_2O_3 nanorods can reach the IPCE up to 55% at 400nm [5], Pt-doped polycrystalline thin-film electrodes of Fe_2O_3 exhibit an IPCE of 25% at 400 nm [6], and Fe_2O_3 thin films modified with a catalytic cobalt layer have the IPCE of 46% at 370 nm [7].

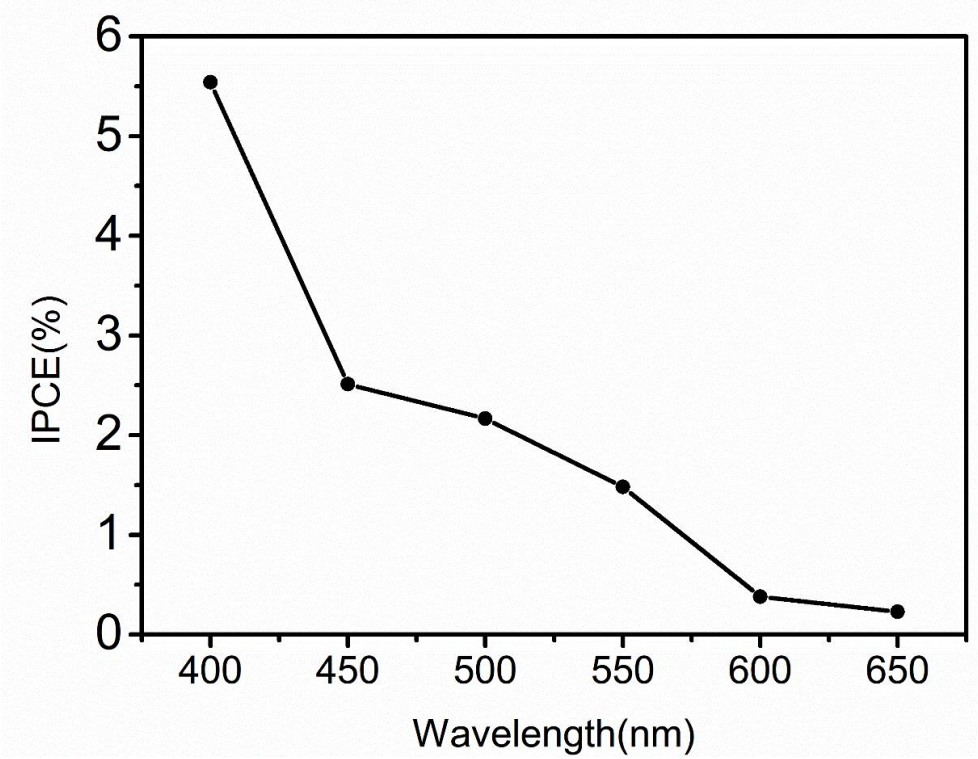

Fig. 3.16 IPCE of Fe_2O_3 nanowire array photoanode at 0.234 V vs. Ag/AgCl (1.23 V vs. RHE).

3.4.3 Stability of high density Fe_2O_3 nanowire array

The stability of photocurrent was measured at 1.23 eV vs. RHE by a chopped illumination with 10s on/off for 120 seconds, for a Fe_2O_3 nanowire array photoanode fabricated at 450 ^oC, as shown in Fig. 3.17. The photocurrent density is very stable and increased and decreased quickly with on and off the light which shows the good photoresponse properties of the Fe_2O_3 nanowire array photoanode.

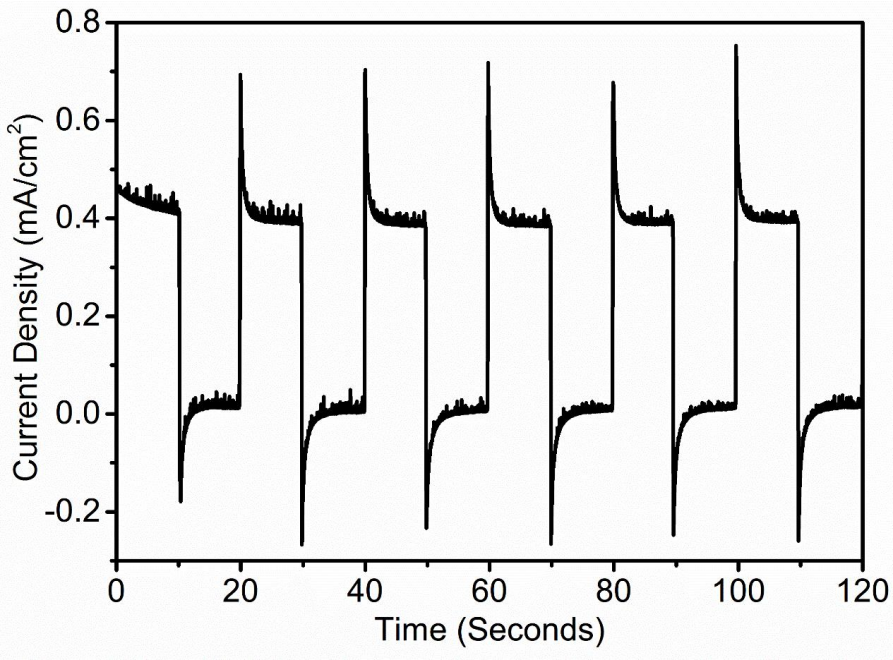

Fig. 3.17 J-t curve of Fe_2O_3 nanowire array photoanode under chopped illumination at a bias of 0.234 V vs. Ag/AgCl (1.23 V vs. RHE).

3.5 Mechanism of high density Fe_2O_3 nanowire growth

3.5.1 EDS observation

In order to certify the mechanism of the high density Fe_2O_3 nanowire growth, the first step is to understand the structure inside the Fe substrate after heating process. Here the EDS observation has been carried out from the cross section image of the Fe substrate, as shown in Fig. 3.18. Six positions has been chosen from the cross section, and the elements in these positions have been characterized by the EDS, the results are shown in Fig. 3.19 to Fig. 3.24.

From the result it can be found that in the upper layer the percentage of oxygen is about 61%, which suggested that the upper layer may consisted of the iron oxide. However, in the second layer, the percentage of iron from point 004, 005, 006 shows that there is only a few oxygen exists, which means the second layer was mainly consisted of pure iron.

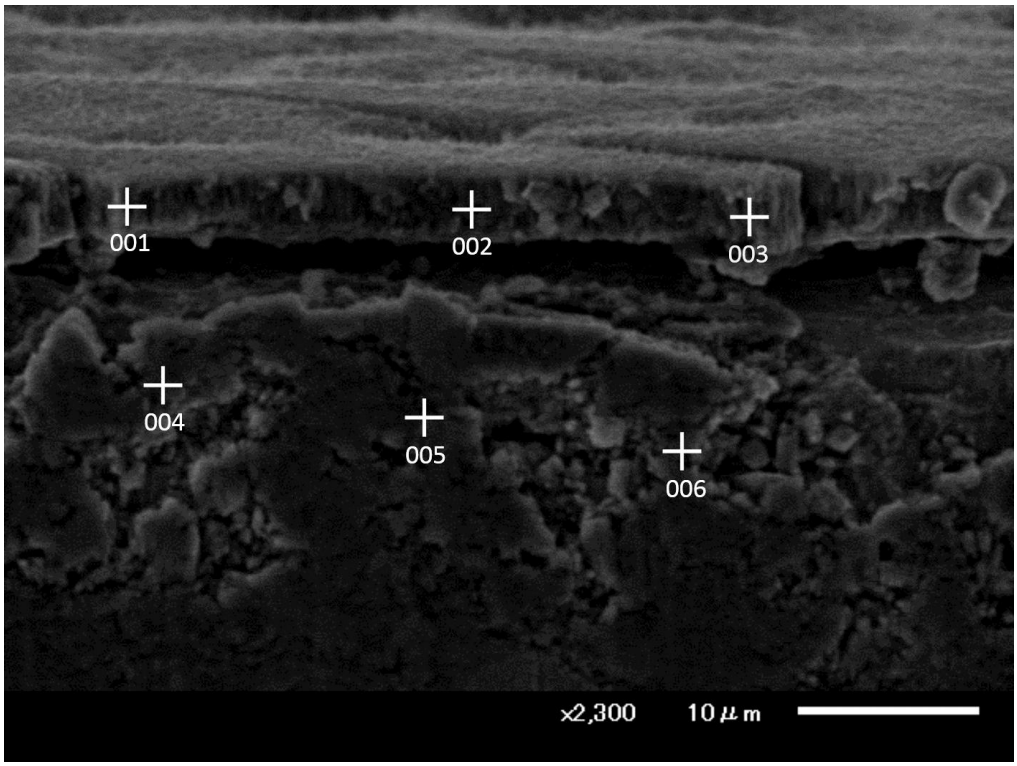

Fig. 3.18 EDS observation of the sample.

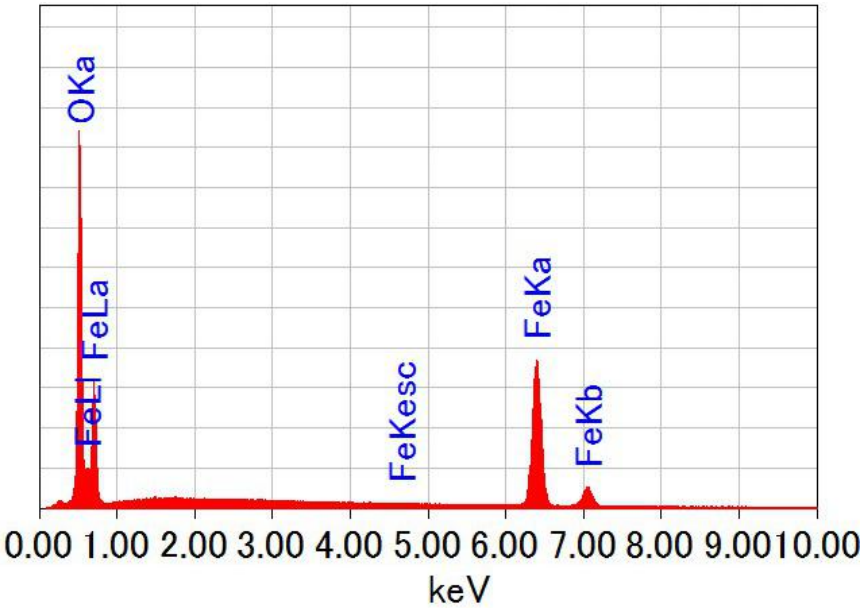

Fig. 3.19 EDS result of spot 1.

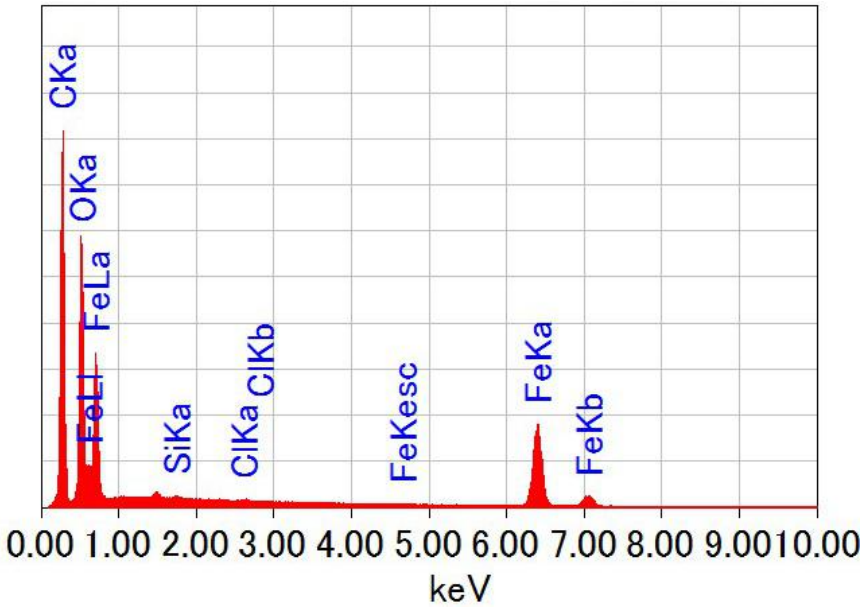

Fig. 3.20 EDS result of spot 2.

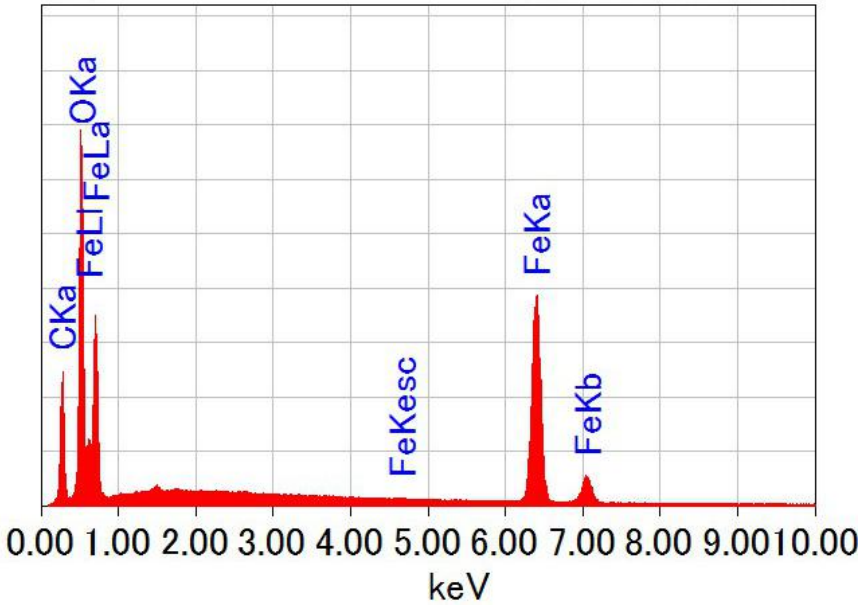

Fig. 3.21 EDS result of spot 3.

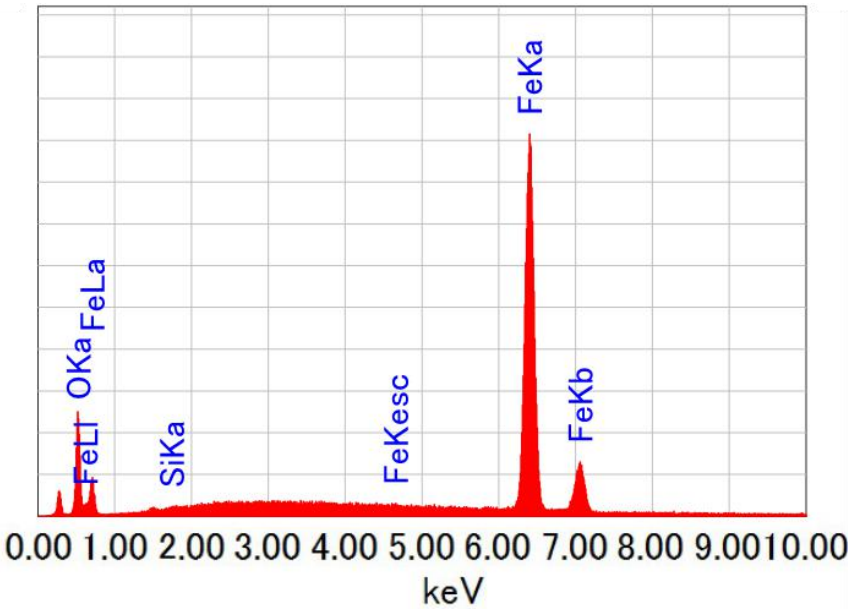

Fig. 3.22 EDS result of spot 4.

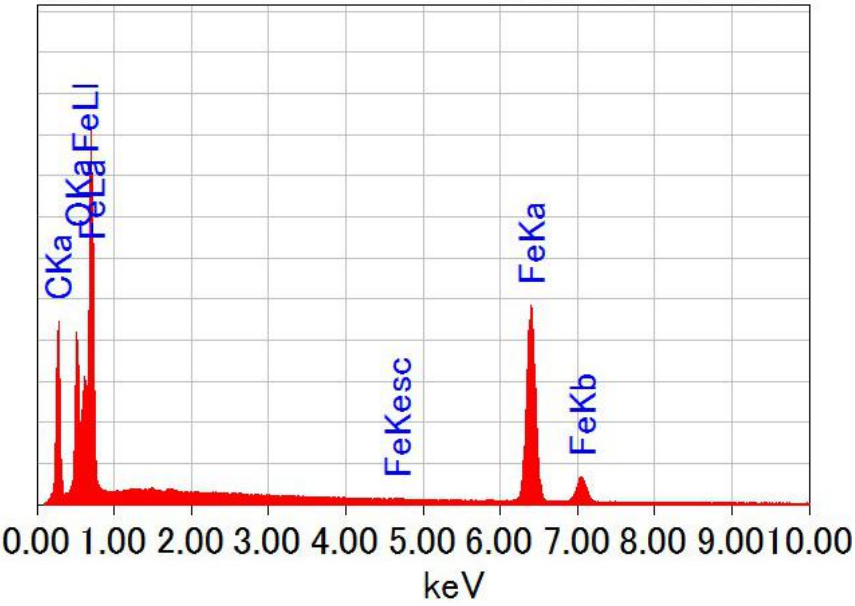

Fig. 3.23 EDS result of spot 5.

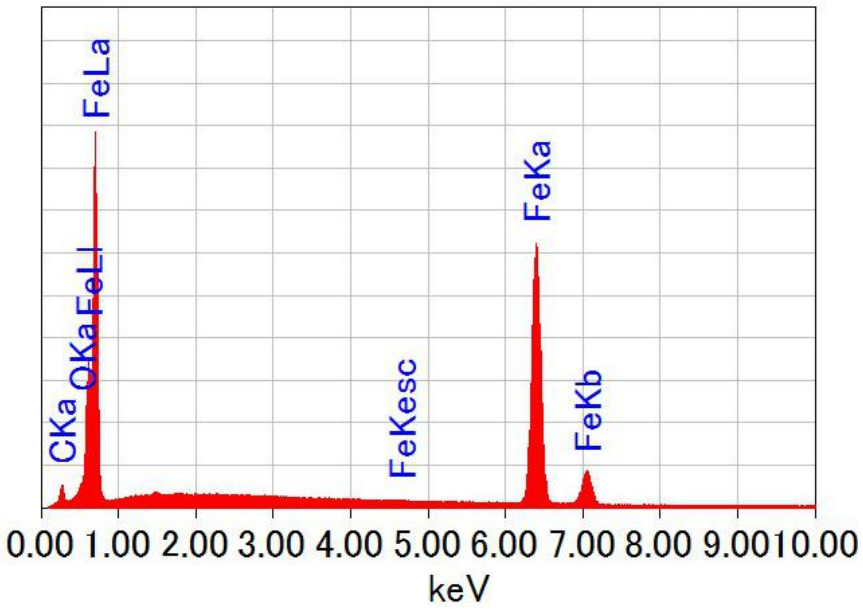

Fig. 3.24 EDS result of spot 6.

3.5.2 Mechanism

The mechanism of nanowire growth is shown in Fig. 3.25 in detail. When the iron plates are heated, the thermodynamically stable oxide layer, Fe_2O_3 topmost layer are formed. Because the molar volumes of Fe_2O_3 (30.39 cm^3/mol) is great larger than that of Fe (7.09 cm^3/mol), tensile stress is generated in the iron plate due to the volume expansion of Fe_2O_3 layer [8]. Thus, a stress gradient is generated from inside of the Fe plate to the Fe/Fe_2O_3 interface. The gradient of stress can serve as the driving force for the atomic diffusion and the atomic flux propagates from the low tensile area to high tensile area. Therefore, with the formation of the Fe_2O_3 layer, the Fe atoms move from inside of Fe plate to Fe/Fe_2O_3 interface due to the stress-induced atomic diffusion. These diffusion atoms serve as a continuous source for the formation of Fe_2O_3 nanowires.

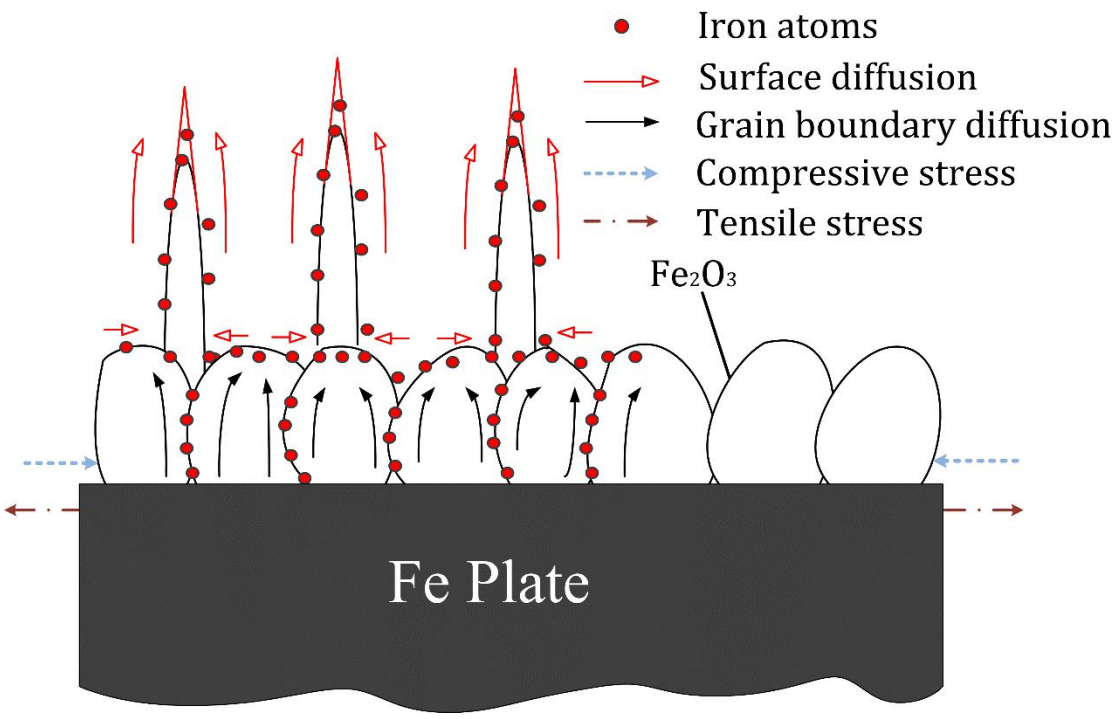

Fig. 3.25 Schematic of the mechanism of the nanowire growth.

After the Fe atoms diffuse along the stress gradient to the Fe/Fe_2O_3 interface, they cumulate at the interface and then find the weak spots of Fe_2O_3 layer and penetrate them to form nanowires accompanying the oxidation of the Fe atoms. After the nanowires are formed, Fe atoms continue to diffuse along the nanowires due to the high driving force, which explains the formation of longer nanowires with the increase in the heating time. Under the water vapor condition, greater amounts of iron can be oxidized into Fe_2O_3, which could increase the thickness of the Fe_2O_3 layer on the Fe substrate. Therefore, the tensile stress that the Fe layer suffered from the Fe_2O_3 layer is much larger in the presence of water vapor than that created under an atmosphere condition. This increase the stress gradient and the driving force for atom diffusion, thereby resulting in an increase in the density of the nanowires. It should be noted that the driving force induced by the stress gradient is due to the volume expansion of the Fe_2O_3 oxidation layer, which is different from that induced by the thermal expansion mismatch generated in Al/Si [9] or Cu/Si [10] structured samples. The similar thermal expansion coefficients of Fe_2O_3 ($12\times10^{-6}/^{o}C$) and Fe

($12.2\times10^{-6}/^{o}C$) make it difficult to create a stress based driving force based on thermal expansion mismatch.

3.6 Summary

In summary, a new oxidation-assisted stress-induce method to fabricate high-density semiconductor nanowire array has been demonstrated. Large area Fe_2O_3 nanowire arrays with high density were fabricated successfully at low temperatures under the water vapor condition. The nanowire array with the largest density (14.3 wire/μm^2) could be obtained from the sample heated at 450 ^{o}C for 90 minutes, under the water vapor volume of 0.25 L/h. However, the largest photocurrent density (0.65 mA/cm^2) was obtained from the sample heated at 350 ^{o}C for 90 minutes, under the water vapor volume of 0.25 L/h, with the density of 8.66 wire/μm^2 and the average diameter of 161 nm, approximately. Therefore, it is considered that both the density and diameter of the nanowires affect the photocurrent density of the nanowire photoanode. The photocurrent measurements indicate the good potential of the Fe_2O_3 nanowire array photoanodes for solar water splitting.

References

1. Fu Y Y, Wang R M, Xu J, et al. Synthesis of large arrays of aligned α-Fe_2O_3 nanowires[J]. Chemical Physics Letters, 2003, 379(3): 373-379.
2. X. Wen, S. Wang, Y. Ding, Z. L. Wang and S. Yang, J. Phys. Chem. B, 2005, 109, 215-220.
3. Wang G, Ling Y, Wheeler D A, et al. Facile synthesis of highly photoactive α-Fe_2O_3-based films for water oxidation[J]. Nano letters, 2011, 11(8): 3503-3509.
4. Li M, Zhang Z, Lyu F, et al. Facile Hydrothermal Synthesis of Three Dimensional Hematite Nanostructures with Enhanced Water Splitting Performance[J]. Electrochimica Acta, 2015, 186: 95-100.
5. Kim J Y, Magesh G, Youn D H, et al. Single-crystalline, wormlike hematite photoanodes for efficient solar water splitting[J]. Scientific reports, 2013, 3: 2681.
6. Schrebler R S, Ballesteros L, Burgos A, et al. Electrodeposited nanostructured α-Fe_2O_3 photoanodes for solar water splitting: effect of surface Co-modification on photoelectrochemical performance[J]. Journal of The Electrochemical Society, 2011, 158(8): D500-D505.
7. Yang Z, Li Z, Yu L, et al. Achieving high performance electromagnetic wave attenuation: a rational design of silica coated mesoporous iron microcubes[J]. Journal of Materials Chemistry C, 2014, 2(36): 7583-7588.
8. Hu L, Ju Y, Hosoi A, et al. The surface condition effect of Cu_2O flower/grass-like nanoarchitectures grown on Cu foil and Cu film[J]. Nanoscale research letters, 2013, 8(1): 445.
9. Chen M, Yue Y, Ju Y. Growth of metal and metal oxide nanowires driven by the stress-induced migration[J]. Journal of Applied Physics, 2012, 111(10): 104305.
10. Yue Y, Chen M, Ju Y, et al. Stress-induced growth of well-aligned Cu_2O nanowire arrays and their photovoltaic effect[J]. Scripta Materialia, 2012, 66(2): 81-84.

Chapter 4 Fabrication of high density single-crystal Fe_2O_3 nanowire array

4.1 Introduction

The advantages of nanowire structure for PEC water splitting is that it could provide a significant enlargement of material surface area, which could increase the absorption of sunlight and the contact surface between the photoanode and electrolyte. Also it has been reported that nanostructure is helpful to overcome the short hole diffusion length of Fe_2O_3 because it could reduce the necessary path length of hole transport [1,2]. Compare to the poly crystalline nanowire array, single-crystal nanowire array is considered more suitable to improve the efficiency of water splitting, because single-crystal could reduce the recombination due to the less grain boundaries [3]. In this chapter, a method to fabricated high density single-crystal Fe_2O_3 nanowire array has been introduced.

4.2 Fabrication of single-crystal high density Fe_2O_3 nanowire arrays

4.2.1 Sample preparation

Commercial iron plate with the purity of 99.95% was used as the substrate in this study. The thickness of the iron plate is 0.1 mm and the size is 10×10 mm^2. In order to investigated the effect of surface roughness on nanowire growth, two kinds of samples were prepared. One kind of them was polished by a rasp and the others were unpolished samples, as shown in Fig. 4.1. Then two kinds of samples were put in the alcohol, cleaned by the ultrasonic cleaner (AS ONE ASU-2D).

Fig. 4.1 Surface condition of unpolished sample and polished sample.

4.2.2 Experimental conditions

All the samples were heated by a ceramic heater (SAKAGUCHI SCR-SHQ-A) in the air condition. Heating times were set at 90 minutes. Heating temperatures were changed in order to find the optimum condition for nanowire growth, as shown in Table 4.1.

Table 4.1 Experimental conditions: Different heating temperatures.

No.	Heating time (min)	Temperature (°C)	Surface condition
1	90	500	unpolished
2		600	unpolished
3		700	unpolished
4		500	polished
5		600	polished
6		700	polished

After the fabrication of Fe_2O_3 nanowire array, scanning electron microscopy (SEM, JSM-7000FK) images were collected for the Fe_2O_3 nanowire arrays in order to study the morphology. Transmission electron microscope (TEM) observation was carried out to take the high resolution picture of single nanowire and identify the crystalline of the Fe_2O_3 nanowires. X-ray diffraction (XRD) analysis was also performed to study the structure and phase of the nanowire arrays.

4.3 Evaluations

4.3.1 Morphology of Fe_2O_3 nanowire array

Figure 4.2 to 4.7 show the SEM image of Fe_2O_3 nanowire arrays fabricated at 500 ^oC, 600 ^oC and 700 ^oC with and without surface polishing treatment, respectively. From the SEM images, it can be found that the sizes of nanowire arrays fabricated under different temperatures are very different. It can be found that there are two kinds of nanowire shapes on the sample heated at 500 ^oC, i.e., wire shaped and leaf shaped nanowires, as shown in Fig. 4.2 and Fig. 4.5. For samples heated at 600 ^oC, the length of nanowires is much longer than that of the sample heated at 500 ^oC, and

the diameters become smaller. The shape of nanowires heated at 600 °C on the unpolished sample is like a long leaf, and the nanowires grow from the polished sample is wire shaped with the average diameter of 29 nm, as shown in Fig. 4.3 and Fig. 4.6, respectively. Figure 4.4 and 4.7 show the nanowires heated at 700 °C on the unpolished and polished samples. It can be found that the shape of nanowires obtained from both polished and unpolished sample is like long triangle. In this study, the average density, average length and average diameter of nanowires have been evaluated based on the SEM observation results, as shown in Fig. 4.8, Fig. 4.9 and Fig. 4.10, respectively.

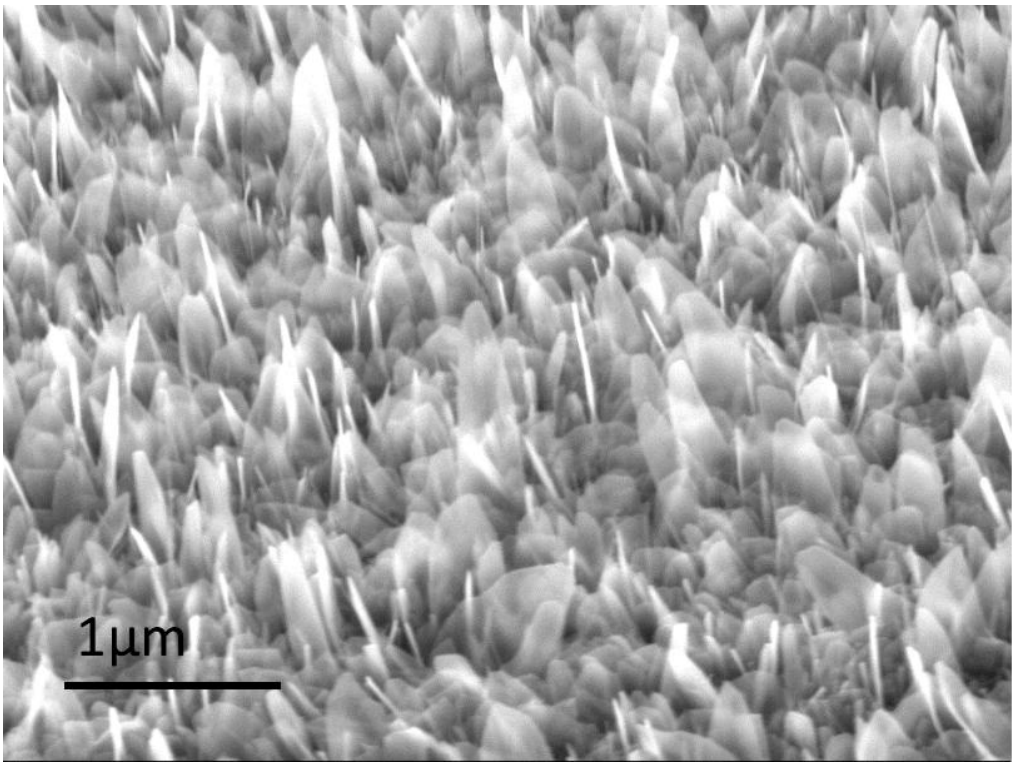

Fig. 4.2 SEM images of nanowire arrays obtained at 500 °C, unpolished sample.

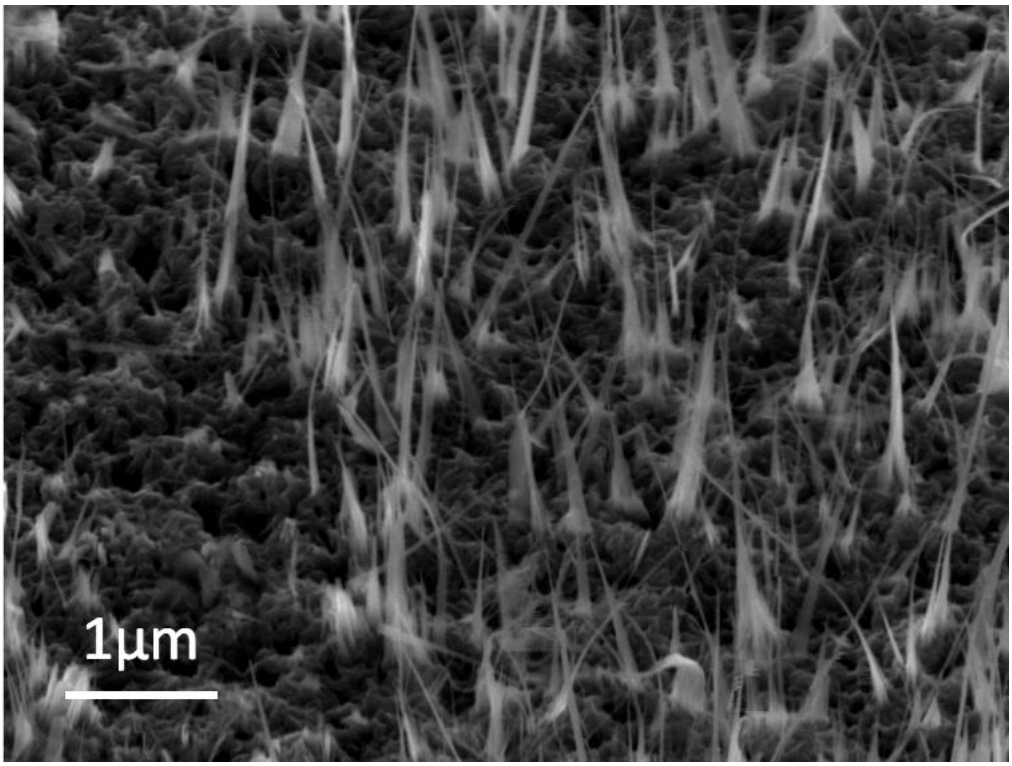

Fig. 4.3 SEM images of nanowire arrays obtained at 600 °C, unpolished sample.

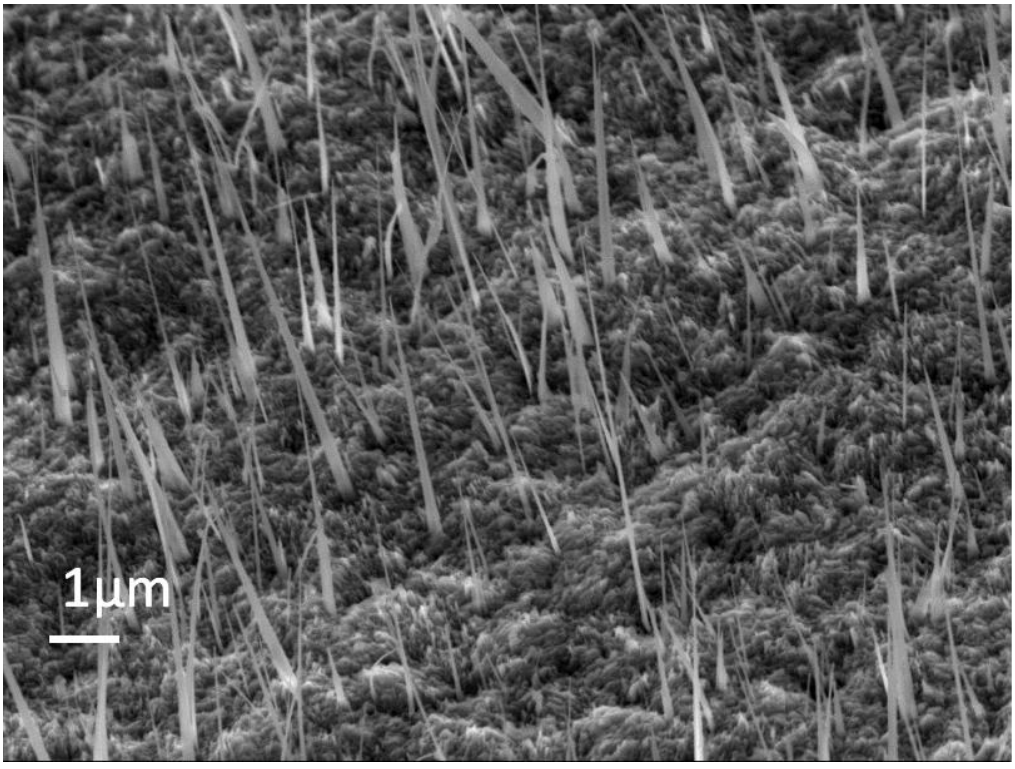

Fig. 4.4 SEM images of nanowire arrays obtained at 700 °C, unpolished sample.

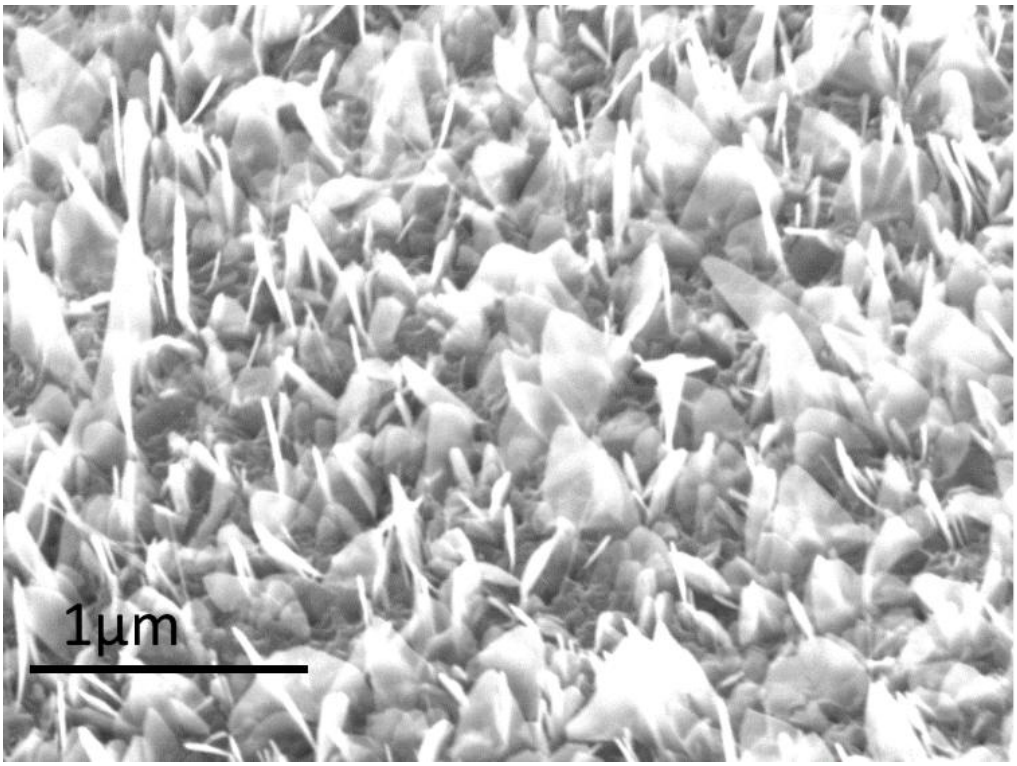

Fig. 4.5 SEM images of nanowire arrays obtained at 500 °C, polished sample.

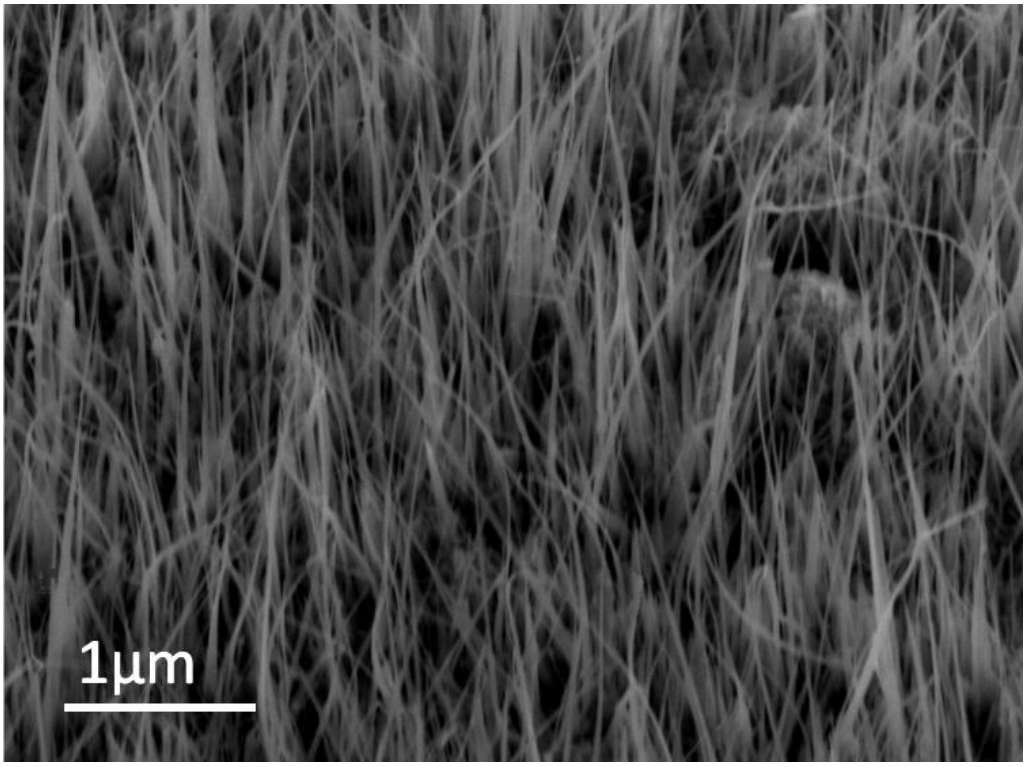

Fig. 4.6 SEM images of nanowire arrays obtained at 600 °C, polished sample.

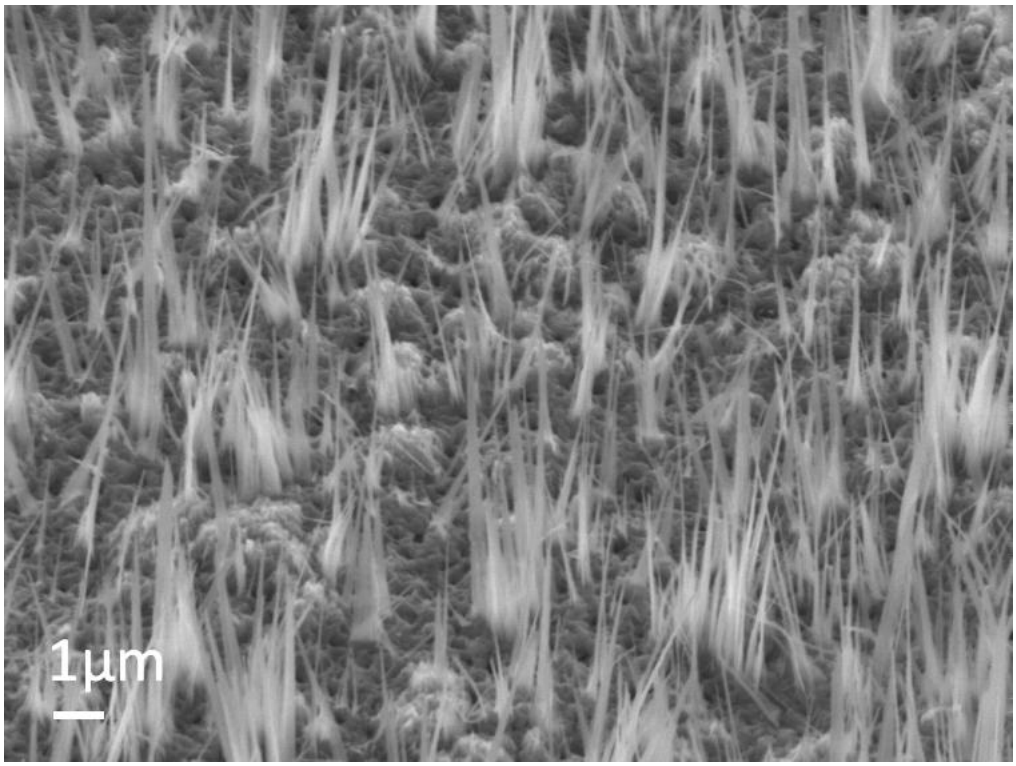

Fig. 4.7 SEM images of nanowire arrays obtained at 700 °C, polished sample.

As shown in Fig. 4.8, the largest density of 28.75 wire/μm^2 was achieved from the polished sample heated at 600 °C for 90 minutes, which is 5 times higher than the density of unpolished sample (5 wire/μm^2) heated at the same condition. For the sample heated at 500 ^oC, it can also be found that the density of polished samples is higher than the unpolished samples. It should be mentioned that nanowire arrays fabricated under all the experimental condition are uniform except the unpolished sample heated at 700 ^oC.

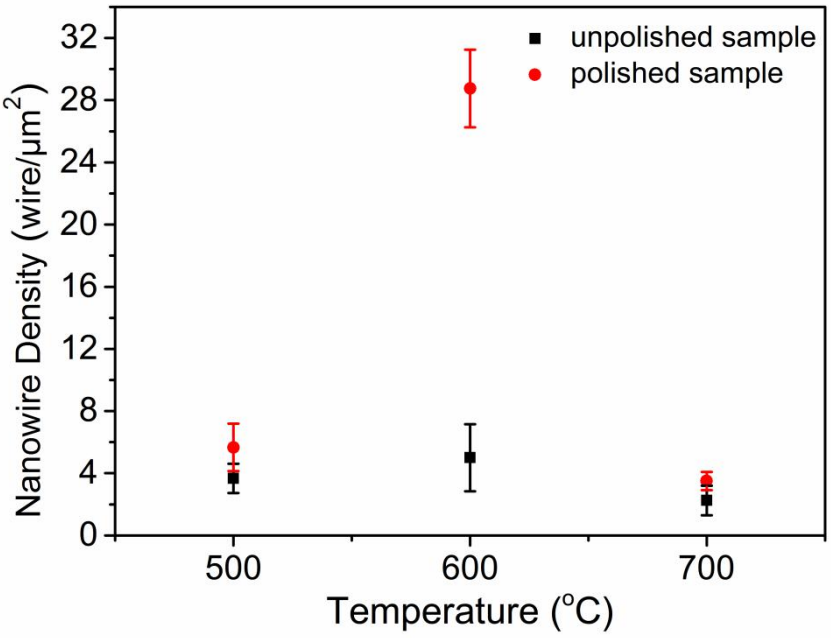

Fig. 4.8 Statistical variation of density of the Fe_2O_3 nanowires obtained at different experimental conditions.

On the other hand, it has been reported that 1D nanostructures could reduce the path length of hole transport to improve the carrier recombination due to the high aspect ratio and large surface area. As shown in Fig. 4.9, with the increase of heating temperature, the average length of the nanowires also become longer on both polished and unpolished samples, and the longest nanowires were obtained to be 3.37 μm at 700 °C from the unpolished sample. Also it can be found that the length of nanowires was almost the same for the polished and unpolished samples under the same temperature, which indicated that the heating temperature is the key factor of nanowire length. For the diameter of nanowire used for the photoanode of water splitting, it is considered that small diameter could reduce the diffusion distance of photogenerated minority carriers from the center to semiconductor-electrolyte interface. As shown in Fig. 4.10, the smallest average diameter of 29 nm was obtained for nanowires fabricated at 600 °C for 90 minutes from the polished sample. It should be mentioned that nanowire arrays fabricated at 500 °C shows a wide range of the diameters, this is due to the diameter of wire shaped nanowire is much smaller than that of the leaf shaped nanowire.

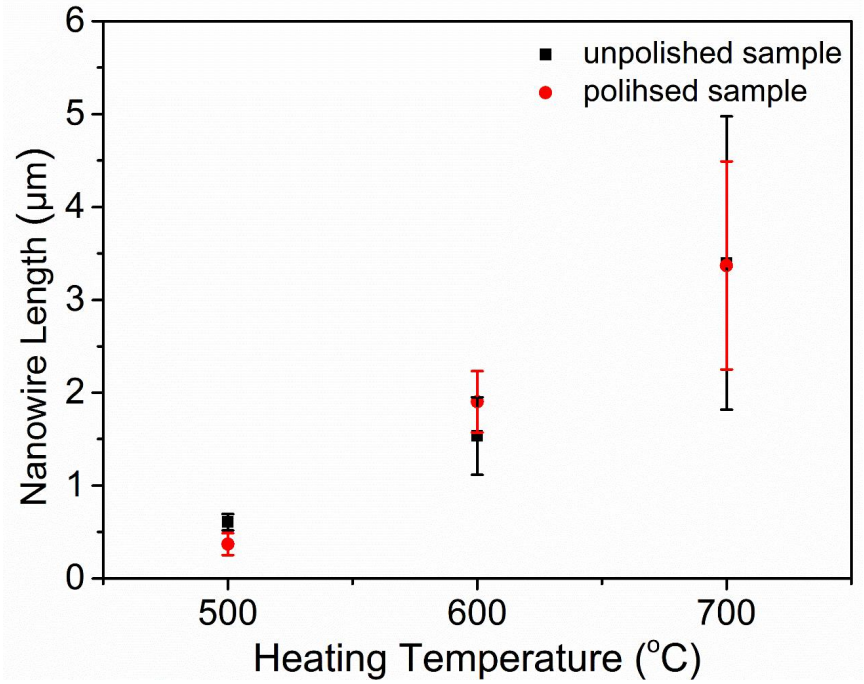

Fig. 4.9 Statistical variation of length of the Fe_2O_3 nanowires obtained at different experimental conditions.

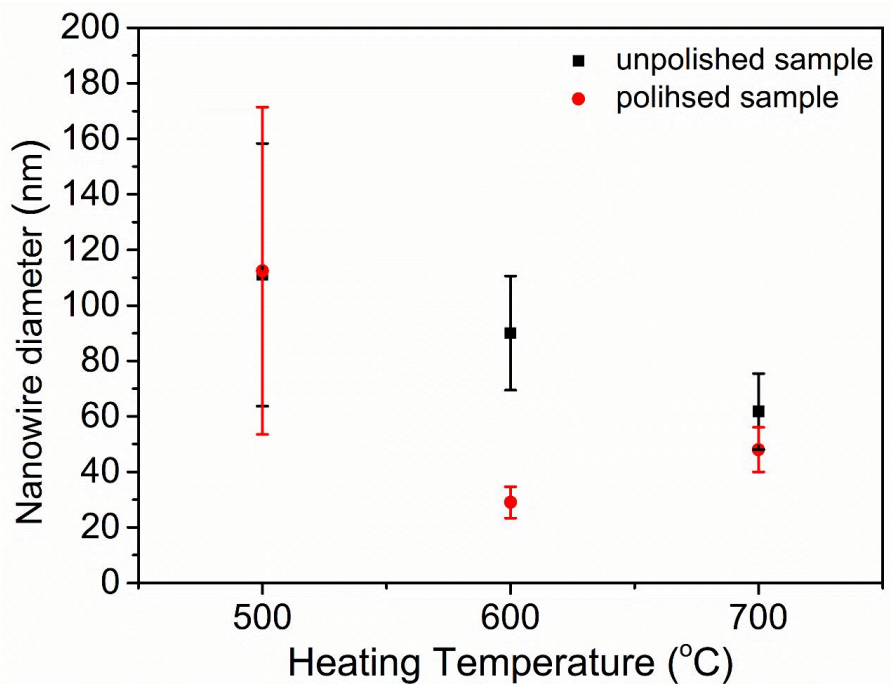

Fig. 4.10 Statistical variation of diameter of the nanowires obtained at different experimental conditions.

4.3.2 Effect of surface roughness on Fe_2O_3 nanowire growth

In order to investigated the effect of surface roughness of Fe_2O_3 nanowire growth, the roughness of polished and unpolished sample have been measured by a white interference microscope (ZYGO new view 6000). Three samples with different roughness have been prepared in this test: unpolished sample; the sample polished in one direction; and the sample polished in two direction, as shown in Table 4.2. Fig 4.11 shows the direction of polishing treatment of sample 2 and sample 3.

Table 4.2 Experimental conditions

Sample number	Surface condition
Sample 1	Unpolished
Sample 2	Polished in one direction
Sample 3	Polished in two direction

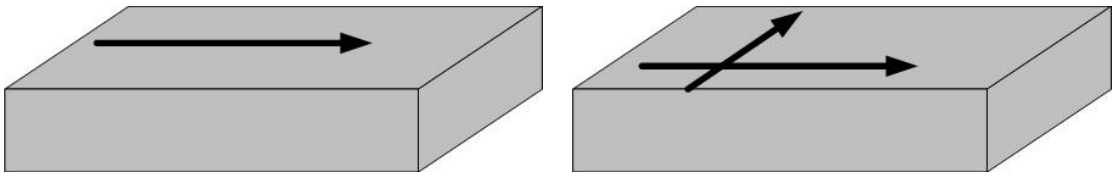

Fig. 4.11 Direction of polishing treatment: (a) polished in one direction; (b) polished in two directions.

The roughness observations of each sample are shown in Fig. 4.12 to Fig. 4.14, and the surface roughnesses were measured to be 0.443 μm, 2.483 μm and 1.644 μm, respectively, as shown in Fig. 4.15.

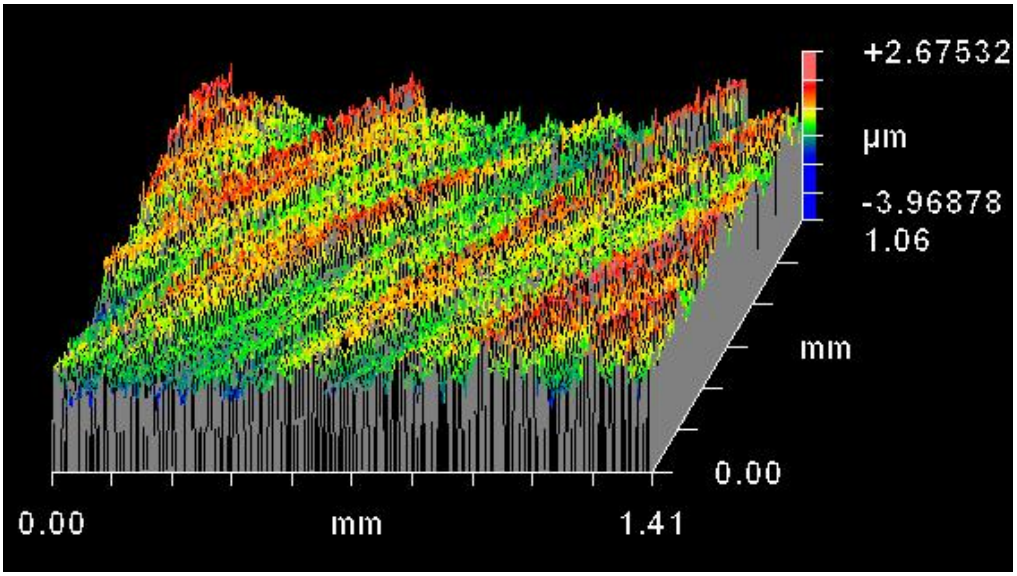

Fig. 4.12 3D model of the unpolished sample.

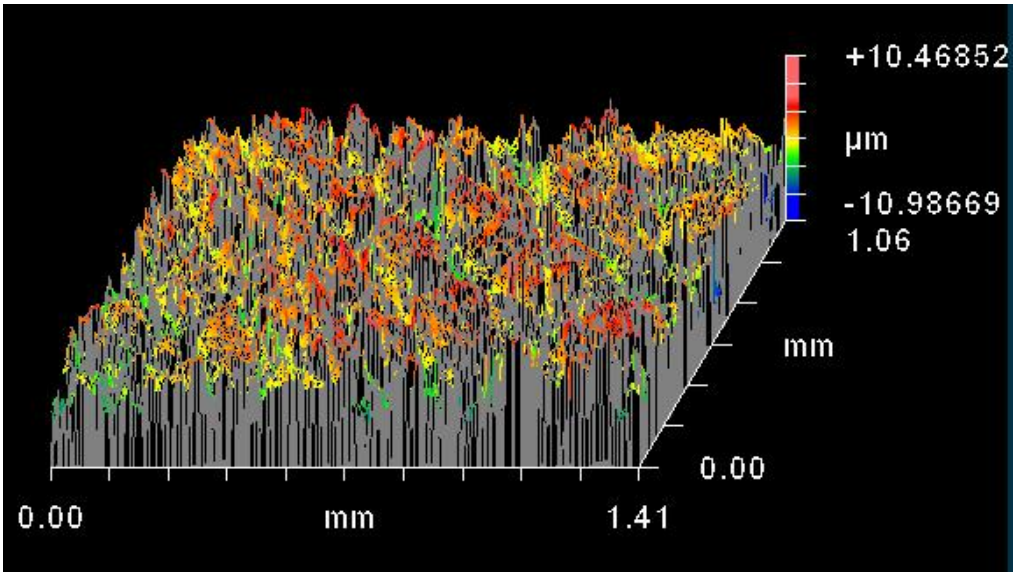

Fig. 4.13 3D model of the sample polished in one direction.

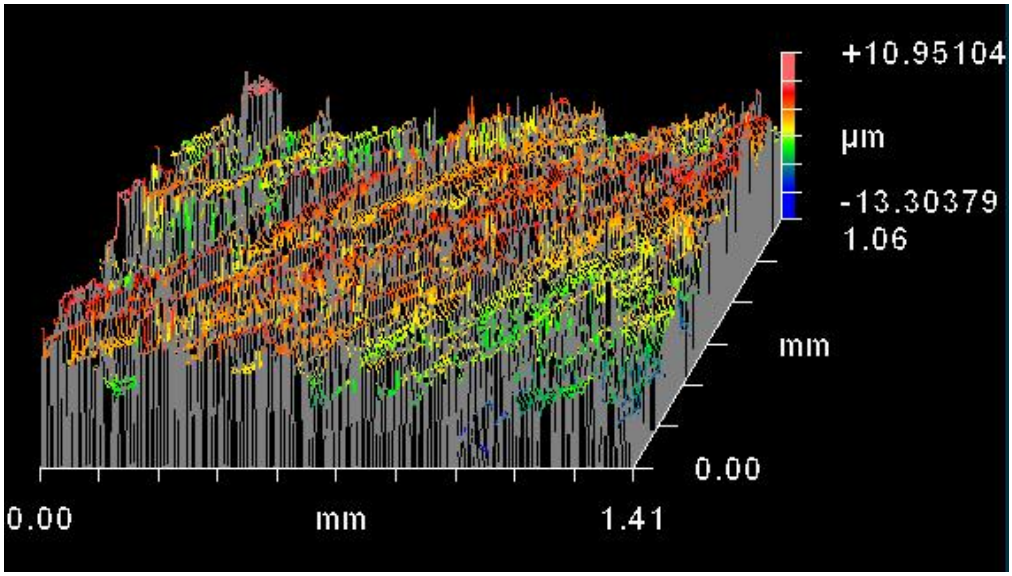

Fig. 4.14 3D model of the sample polished in two direction.

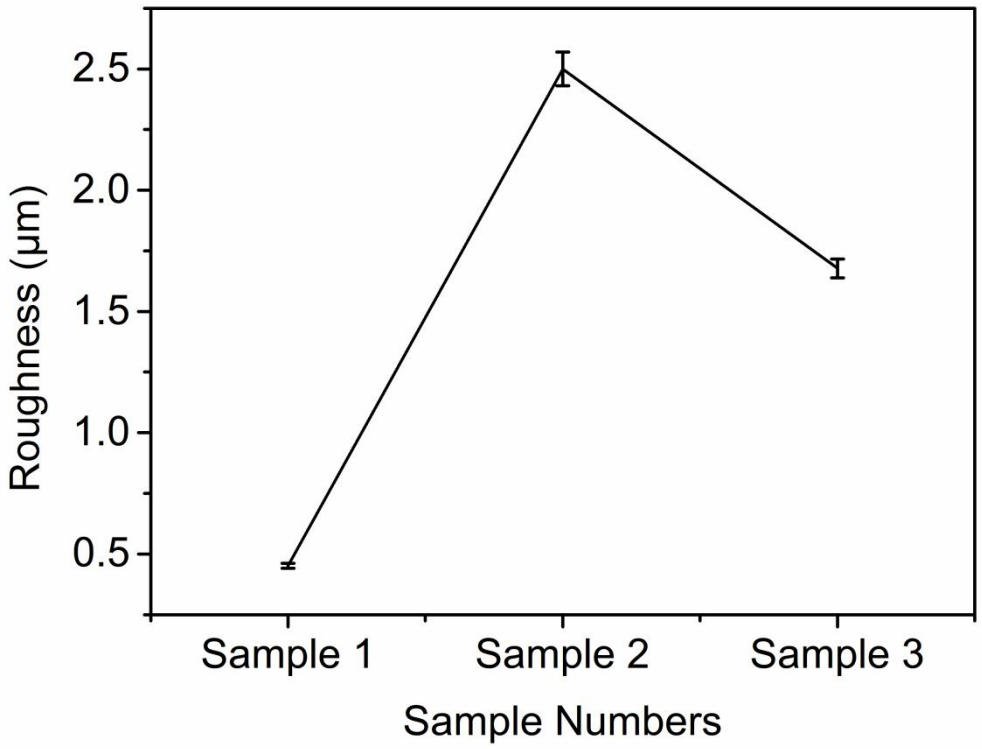

Fig. 4.15 Statistical variation of roughness of samples.

By comparing with the morphologies of Fe_2O_3 nanowire array grown from the sample with different surface roughness, it could be found that nanowire array with the largest density could be obtained from the sample with the largest surface roughness.

From the 3D image of the sample surface, it could be found that the altitude difference of the sample polished in one direction is the largest, which means there are a larger surface area exposed to the air during the heating process. Therefore, the volume of oxide layer will be increased, and the driving force will also be enlarged.

4.3.3 Effect of residual stress on Fe_2O_3 nanowire growth

Residual stress generated during the surface polishing treatment is also considered as a factor which could effect the growth of Fe_2O_3 nanowire array. In order to investigate the residual stress, X-ray sin2Ψ method [4-6] have been used by the X-Ray Diffraction (XRD). The same three samples have been used for the measurement as shown in Table 4.2. The X-ray diffraction (sin2Ψ) method was employed by using the Fe peak, occurring at a diffraction angle of 2θ=44.698°. Slow step scanning in the range from 41° to 48° was observed for Ψ-angles in of 5°, 10° and 15°, as shown in Fig. 4.16, Fig. 4.17 and Fig. 4.18, respectively.

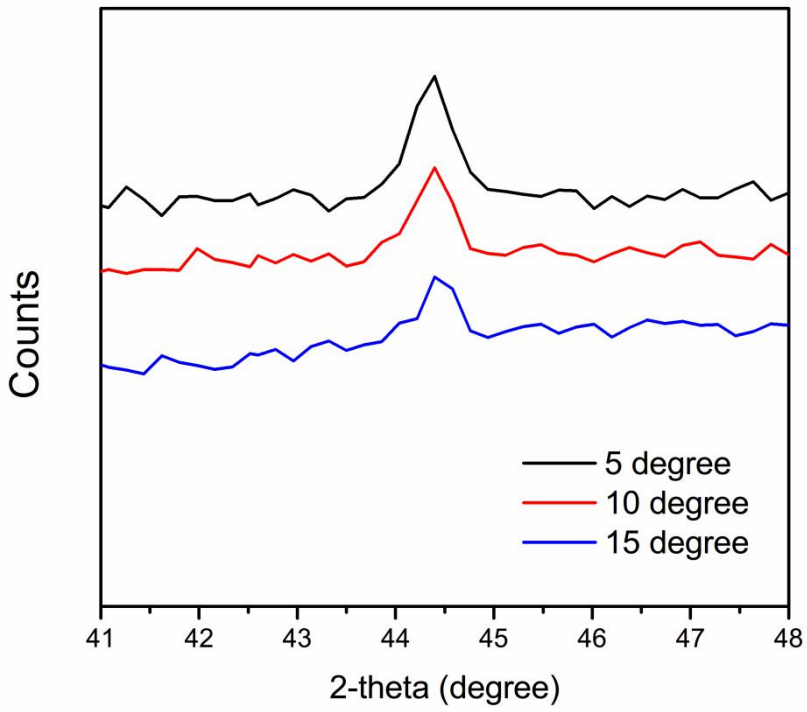

Fig. 4.16 XRD results used for the calculation of residual stress of unpolished sample.

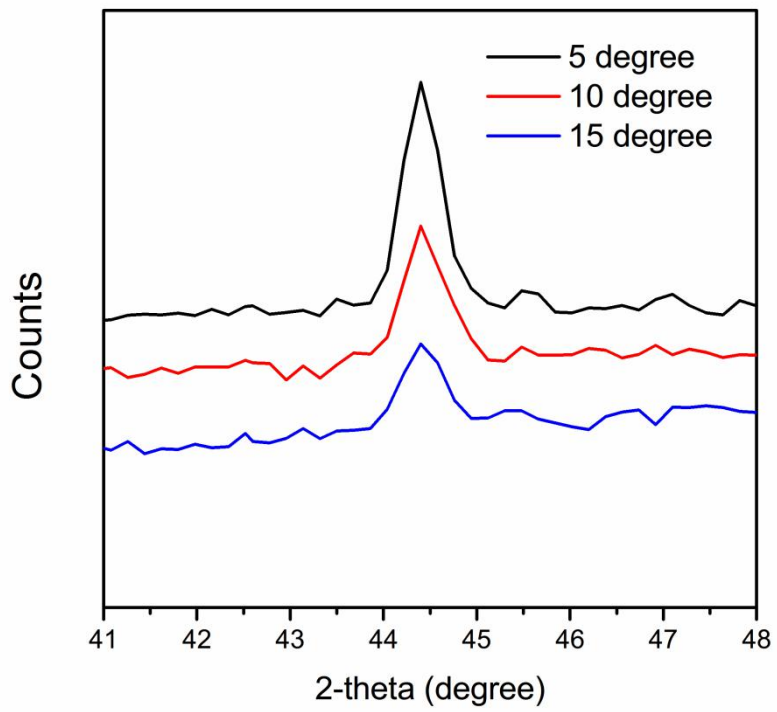

Fig. 4.17 XRD results used for the calculation of residual stress of sample polished in one direction.

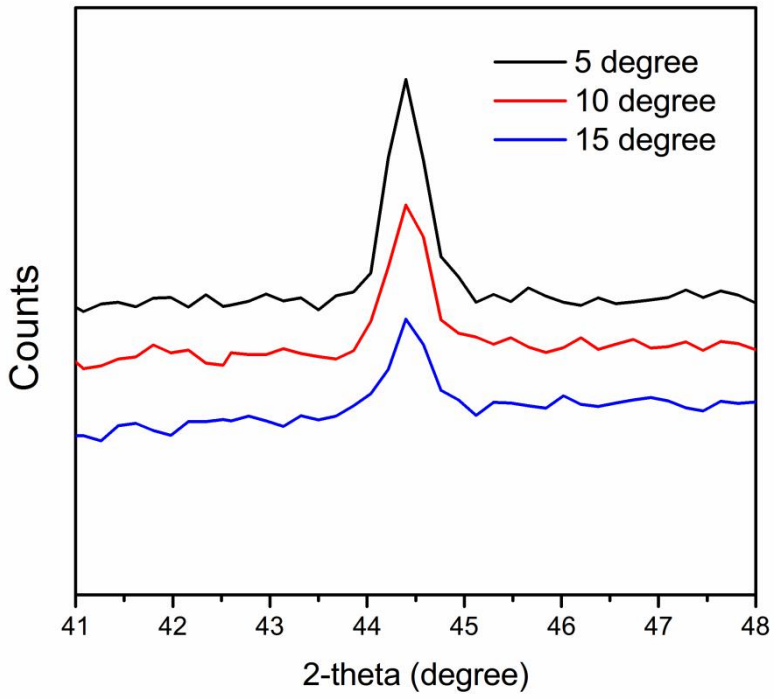

Fig. 4.18 XRD results used for the calculation of residual stress of sample polished in two direction.

After the XRD observation, the residual stress was calculated by a XRD analyze software (JADE 6.5), and the residual stress was confirmed to be compressive stress. The residual compressive stress for unpolished sample is -28.99 MPa, for sample polished in one direction is -125.3 MPa, and for the sample polished in two directions is -107.11 MPa, as shown in Fig. 4.19 In the surface polishing process, the surface of the substrates was deformed by the movements of the rasp, which left a compressive stress on the samples. Compare to the results of surface roughness from each sample, it can be found that the one direction polishing treatment could provide the largest residual stress and surface roughness.

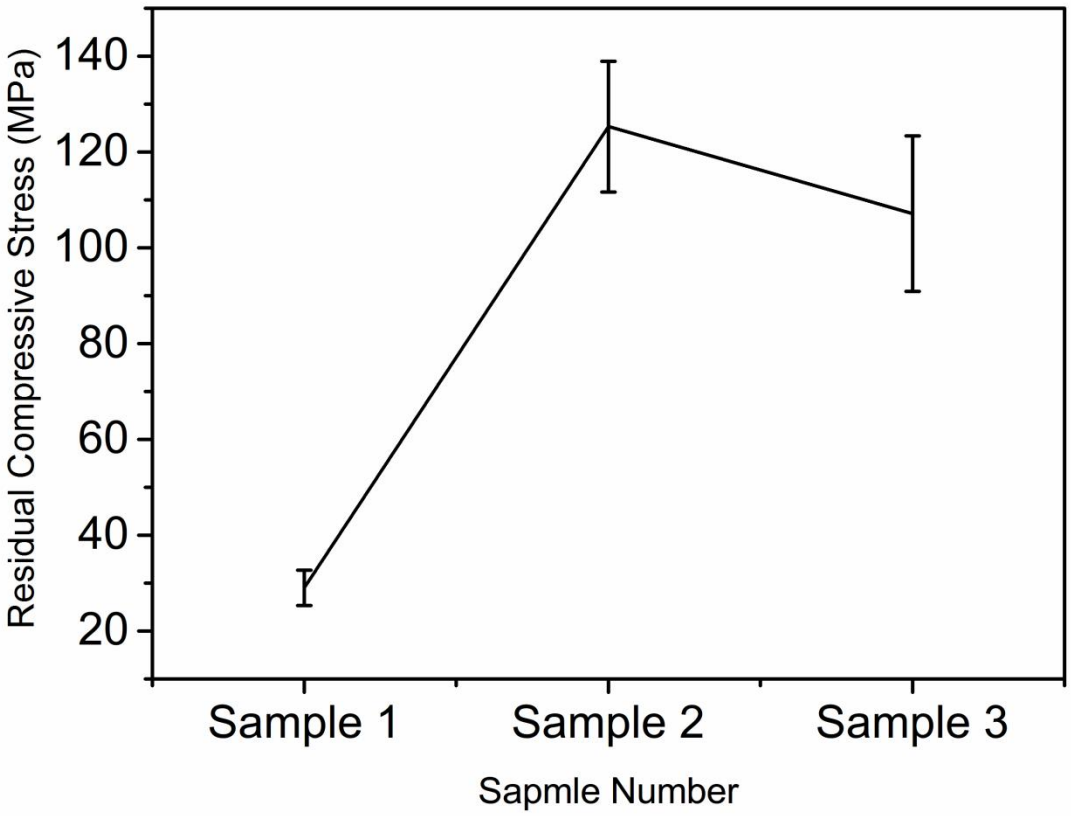

Fig. 4.19 Statistical variation of residual stress in each sample.

4.3.4 Single-crystal Fe_2O_3 nanowire characterization

Figure 4.20 shows the transmission electron diffraction pattern of a single nanowire obtained from polished sample heated at 600 °C. The diffraction pattern image of the Fe_2O_3 nanowire confirmed the nanowire fabricated under this condition is single-crystal nanowire.

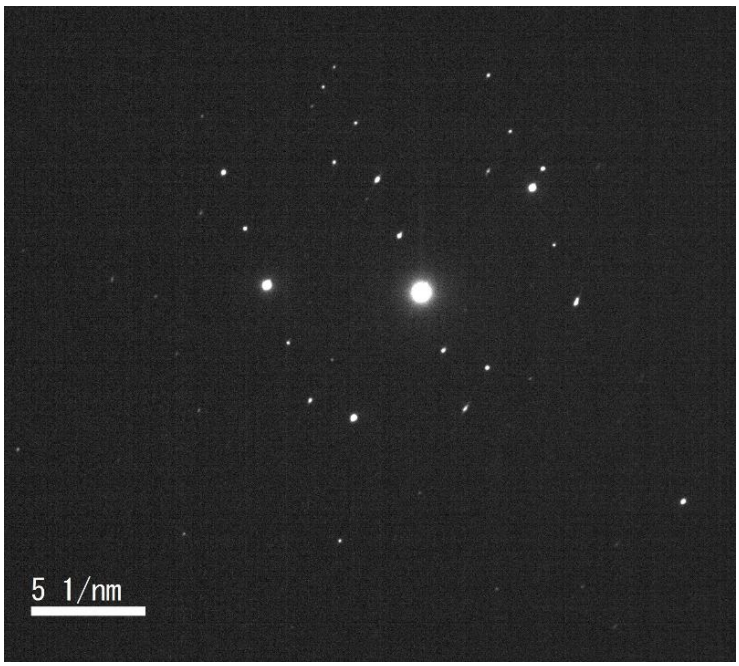

Fig. 4.20 TEM diffraction pattern of the Fe_2O_3 nanowire arrays heated at 600 °C for 90 min from the polished sample.

Representative XRD patterns of the nanowire arrays were obtained from the samples with the surface polishing treatment after heating at different temperatures of 500 °C, 600 °C and 700 °C, as shown in Fig. 4.21. Most of the appeared peaks can be well indexed to the pure alpha phase hematite, except the peak appeared at 30.18°, which is considered as the peak of Fe_3O_4. It can be explained that when heating temperature is over 500 °C, surface of the iron plate will be oxidized to Fe_2O_3 layer. However, since the thickness of the formed Fe_2O_3 layer at 500 °C is smaller than the penetration depth of XRD observation, information of the Fe_3O_4 layer under the Fe_2O_3 layer was collected in the result.

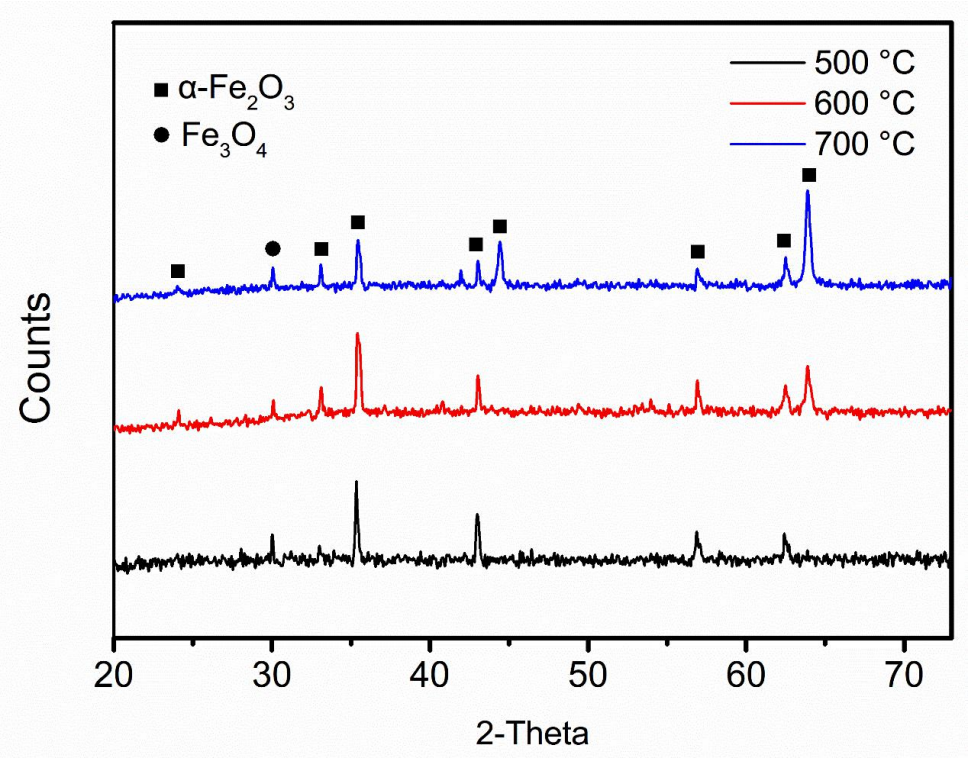

Fig. 4.21 XRD patterns of the Fe_2O_3 nanowire arrays at different temperatures from the polished samples.

4.4 PEC performance evaluation of high density single -crystal Fe_2O_3 nanowire array

4.4.1 Photocurrent of high density single-crystal Fe_2O_3 nanowire array

Photocurrent density of the Fe_2O_3 nanowire arrays fabricated at different experimental conditions have been investigated, as shown in Fig. 4.22.

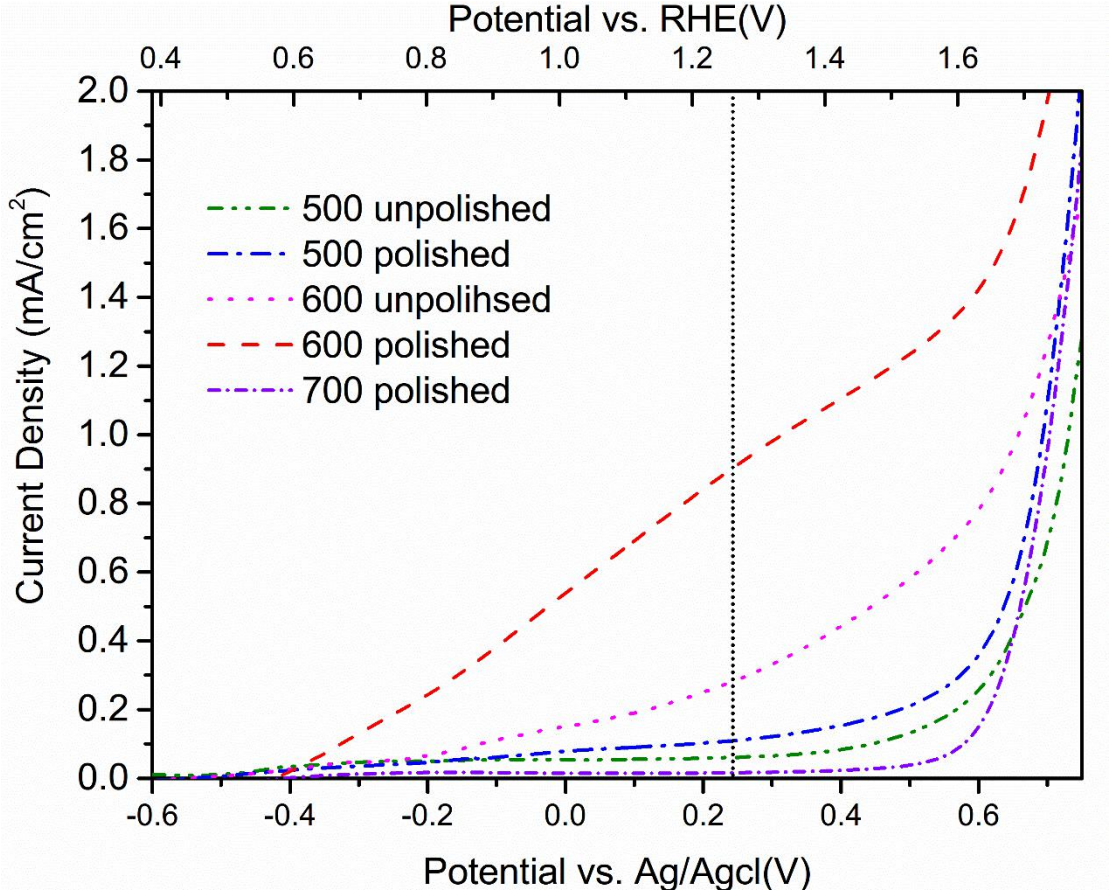

Fig. 4.22 Photocurrent densities from the nanowire array anodes obtained at different experimental conditions.

It can be seen that under each temperature, the polished samples showed a higher photocurrent density than that of the unpolished samples, which could be explained that in the polished sample, the higher density of Fe_2O_3 nanowire arrays could provide more photogenerated carriers, which could enhance the photocurrent density. Samples heated at 600 ^oC with surface polishing treatment showed the highest photocurrent density of 0.9 mA/cm^2 at 1.23 V vs. RHE.

4.4.2 Incident photon-to-electron conversion efficiency of high density single-crystal Fe_2O_3 nanowire array

Figure 4.23 shows the IPCE of the nanowire array fabricated at 600 ^oC from the

polished sample, which is 6.8% at 400 nm at 1.23 V vs. RHE. This value is higher than that of the poly crystalline Fe_2O_3 nanowire array we have reported previously (IPCE of 5.54% at 400 nm) [7]. Moreover, the IPCE value reported in this study is relative high comparing to the other undoped Fe_2O_3 photoanodes fabricated with metallic substrates, such as undoped Fe_2O_3 nanoflakes on Fe foil with the IPCE of 3.43% at 400 nm [8], hematite nanotube array on iron foil with the IPCE of 3.2% at 400 nm [9], and Fe_2O_3 nanorod array on Ti plate with the IPCE of 4.8% at 400nm. However, it should also be mentioned that nanostructured Fe_2O_3 photoanode fabricated on the FTO substrate showed higher IPCE value. For example, Liao et al. reported a IPCE value of 23% at 400nm [10]. Normally, FTO substrate is helpful to increase the photoelectrochemical performance because it could facilitate the electron transport in the photoanode. Therefore, it will be possible to further increase the IPCE value of Fe_2O_3 nanowire array photoanode using FTO substrate, and surface function with dopant doping.

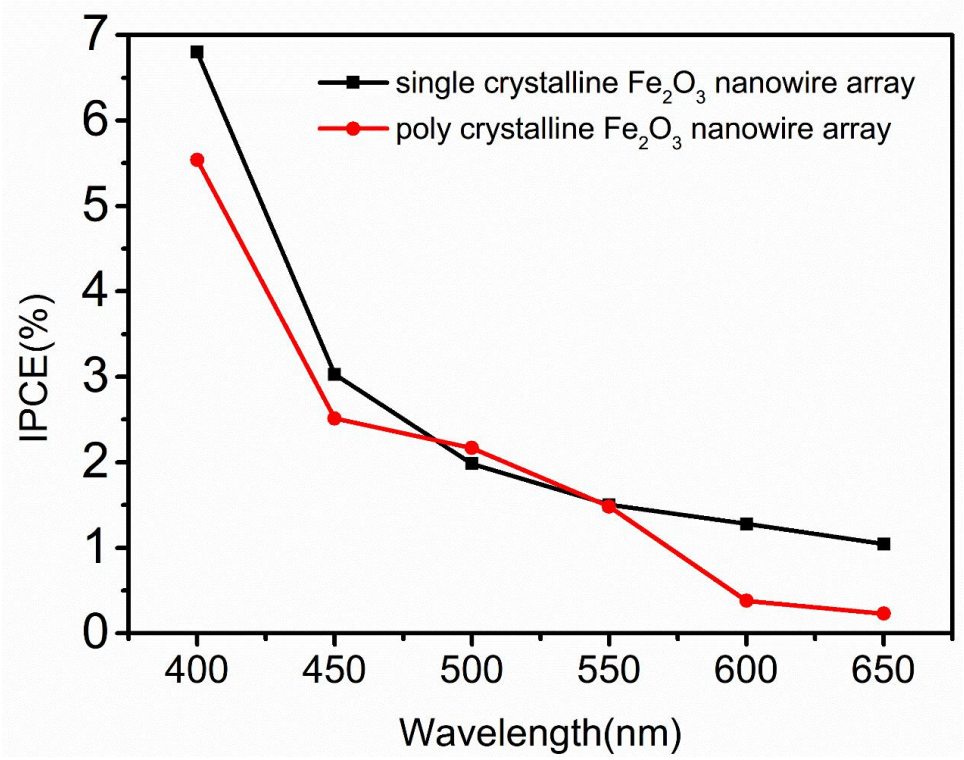

Fig. 4.23 IPCE of the Fe_2O_3 nanowire array photoanode at 0.234 V vs. Ag/AgCl (1.23 V vs. RHE).

4.4.3 Stability of high density single-crystal Fe_2O_3 nanowire array

The photocurrent stability has also been measured in this study, as shown in Fig. 4.24. The Fe_2O_3 nanowire array photoanode fabricated at 600 °C with the polished surface was illuminated with 10s on/off for 300 seconds by a chopped light. From the result, it can be inferred that the photocurrent density is 0.75 mA/cm^2 1.23 V vs. RHE during the illumination. Also it can be found that the photocurrent of the prepared sample changed quickly with the light switch off which shows a good photoresponse properties.

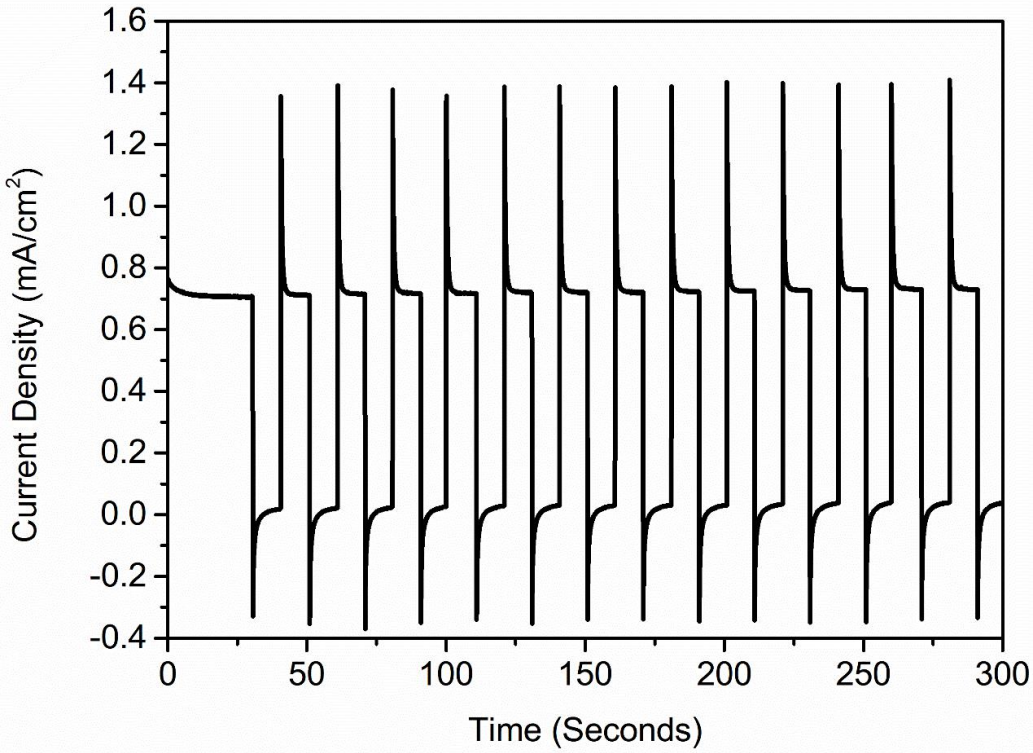

Fig. 4.24 *J-t* curve of the Fe_2O_3 nanowire array photoanode under chopped illumination at a bias of 0.234 V vs. Ag/AgCl (1.23 V vs. RHE).

4.5 Mechanism of single-crystal Fe_2O_3 nanowire growth

In our previous study, we have reported the nanowire growth mechanism based on oxidation assisted stress induced atomic diffusion. Due to the different molar volume of Fe_2O_3 and Fe, tensile stress is generated at the surface of the Fe plate [11,12]. Thus, a stress gradient is generated from the center of the Fe plate to the Fe_2O_3/Fe interface, as the driving force for nanowire growth [7].

In this study, the density of nanowire array fabricated at 600 ^oC on the polished sample is 28.75 wire/μm^2, which is much higher than the density of the nanowire array fabricated from the unpolished sample. It is considered that the surface polishing treatment could provide three advantages for the nanowire growth. Firstly, the polishing treatment induced an initial compressive residual stress on the surface of the Fe plate, which has an effect to obstruct the volume expansion of the oxide layer formed on the sample surface during the heating process. Therefore, a relative larger tensile stress will generate at the surface of the Fe plate, thus a higher effective vertical stress gradient will occur for the same oxide volume expansion. This induce more and faster diffusion of Fe atoms to the sample surface, thereby increasing the density of nanowire array. Secondly, the polishing treatment will deform the surface layer of Fe plate, which lead to the dislocations and intercrystalline failure happened at the Fe plate surface. When the polished Fe plate annealed at high temperature, recrystallization will happen [13]. Due to the cold deformation caused by the polishing treatment, the grain size of Fe will become smaller and the number of grains will increase, which will lead to increase the oxide volume expansion and the number of weak spots of Fe_2O_3 layer finally. Thirdly, the surface polishing treatment increases the roughness of Fe plate surface, which can enlarge the contact area between the sample surface and the air, thereby increasing the volume of Fe_2O_3 layer on the Fe plate. Compare to those unpolished sample, during the heating process, volume expansion of Fe_2O_3 layer for the polished sample is larger, which enhanced the tensile stress at the surface of Fe plate, and increased the driving force for Fe atomic

diffusion, as shown in Fig. 4.25. In summary, the surface polishing treatment could provide a larger driving force and increase the number of weak spots, which could increase the density of nanowire array eventually.

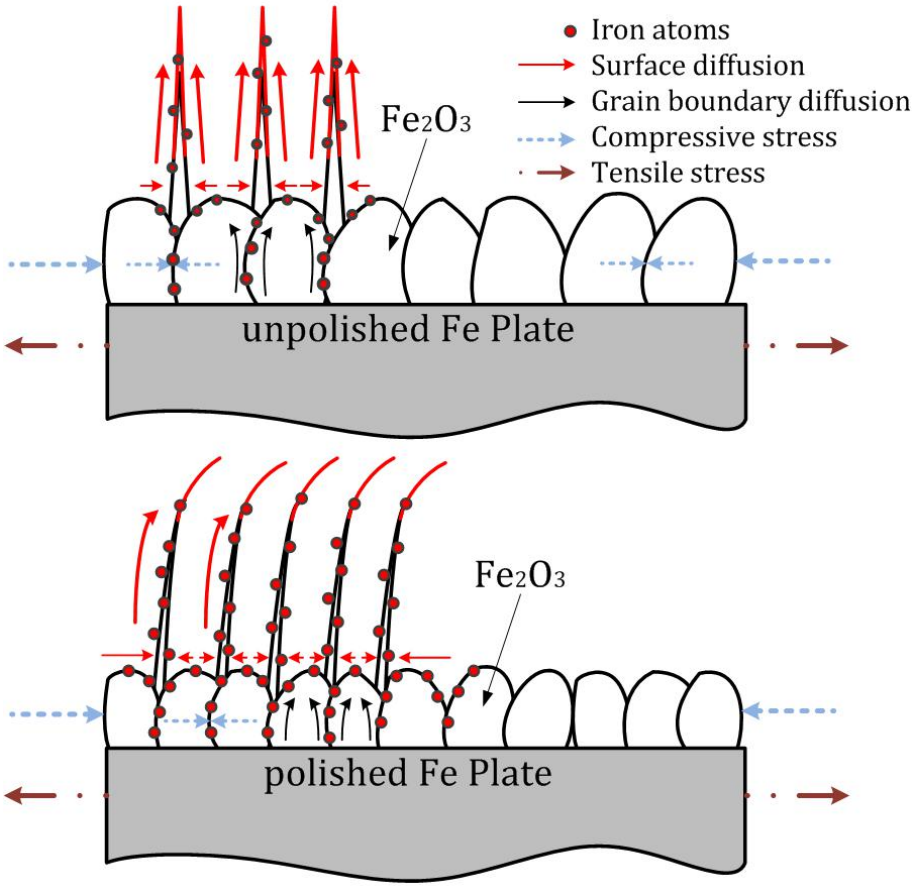

Fig. 4.25 Schematic of the nanowire growth mechanism.

4.6 Summary

In this study, high density single-crystal Fe_2O_3 nanowire arrays were fabricated based on the oxidation-assisted stress-induced atomic-diffusion method from the substrate with surface polishing treatment. The surface polishing treatment could provide a larger driving force and increase the number of weak spots on the sample surface, which lead to the increase of the nanowire density. The highest density of 28.75 wire/μm^2 was reached at the experimental condition of 600 ^oC, 90 minutes heating. The photocurrent density of the single-crystal Fe_2O_3 nanowire arrays is 0.9 mA/cm^2 at 1.23 V vs. RHE, and the IPCE is 6.8% at 400nm wavelength. Stability test results showed the good photocurrent response and stability of the single-crystal Fe_2O_3 nanowire photoanode, which indicates a good potential for the application of solar water splitting.

References

1. Tilley S D, Cornuz M, Sivula K, et al. Light-Induced Water Splitting with Hematite: Improved Nanostructure and Iridium Oxide Catalysis[J]. Angewandte Chemie, 2010, 122(36): 6549-6552.
2. Saremi-Yarahmadi S, Wijayantha K G U, Tahir A A, et al. Nanostructured α-Fe_2O_3 electrodes for solar driven water splitting: effect of doping agents on preparation and performance[J]. The Journal of Physical Chemistry C, 2009, 113(12): 4768-4778.
3. Teke A, Özgür Ü, Doğan S, et al. Excitonic fine structure and recombination dynamics in single-crystalline ZnO[J]. Physical Review B, 2004, 70(19): 195207.
4. Ma C H, Huang J H, Chen H. Residual stress measurement in textured thin film by grazing-incidence X-ray diffraction[J]. Thin Solid Films, 2002, 418(2): 73-78.
5. Zheng X, Li J, Zhou Y. X-ray diffraction measurement of residual stress in PZT thin films prepared by pulsed laser deposition[J]. Acta Materialia, 2004, 52(11): 3313-3322.
6. Wong S M. Residual stress measurements on chromium films by x-ray diffraction using the sin2ψ method[J]. Thin Solid Films, 1978, 53(1): 65-71.
7. Xie Y, Ju Y, Toku Y, et al. Fabrication of Fe_2O_3 nanowire arrays based on oxidation-assisted stress-induced atomic-diffusion and their photovoltaic properties for solar water splitting[J]. RSC Advances, 2017, 7(49): 30548-30553.
8. Wang L, Zhou X, Nguyen N T, et al. Plasmon-Enhanced Photoelectrochemical Water Splitting Using Au Nanoparticles Decorated on Hematite Nanoflake Arrays[J]. ChemSusChem, 2015, 8(4): 618-622.
9. LaTempa T J, Feng X, Paulose M, et al. Temperature-dependent growth of self-assembled hematite (α-Fe_2O_3) nanotube arrays: rapid electrochemical synthesis and photoelectrochemical properties[J]. The Journal of Physical Chemistry C, 2009, 113(36): 16293-16298.
10. Liao A, He H, Fan Z, et al. Facile room-temperature surface modification of unprecedented FeB co-catalysts on Fe_2O_3 nanorod photoanodes for high

photoelectrochemical performance[J]. Journal of Catalysis, 2017, 352: 113-119.

11. Hu L, Ju Y, Hosoi A. Growth of 3-D flower/grass-like metal oxide nanoarchitectures based on catalyst-assisted oxidation method[J]. Nanoscale research letters, 2014, 9(1): 116.
12. Chen M, Yue Y, Ju Y. Growth of metal and metal oxide nanowires driven by the stress-induced migration[J]. Journal of Applied Physics, 2012, 111(10): 104305.
13. Isshiki M, Igaki K. Preparation of High Purity Iron and Its Recrystallization Temperature[J]. Transactions of the Japan Institute of Metals, 1977, 18(5): 412-422.

Chapter 5 Modification of single-crystal Fe_2O_3 nanowire array to enhance photoelectrochemical properties

5.1 Introduction

Fe_2O_3 is a promising material for the photoelectrochemical water splitting due to the suitable band gap (2.1 eV), excellent stability against photo corrosion, abundance, and low-cost. However, there are some disadvantages limited the photoelectrochemical activity of Fe_2O_3, such as short excited-state lifetime (~10^{-12} s) [1, 2], poor oxygen evolution reaction kinetics [3], and a short hole diffusion length (2-4 nm) [4]. In order to overcome these disadvantages, two strategies have been widely studied: nanostructuring and doping another material on Fe_2O_3. In chapter 3 and chapter 4, we have reported two different synthesis methods of Fe_2O_3 nanowire array and their photoelectrochemical performance, the IPCE of the high density single-crystal Fe_2O_3 nanowire array is relatively high compared to other studies use the same material without doping [5-7]. In this chapter, the author has made some modification of the single-crystal high density Fe_2O_3 nanowire array by doping different materials, such as Pt [8-11], Ti [12-14] and Sn [15-19]. Their enhancement effects on photoelectrochemical performance were also investigated in detail.

5.2 Pt-doped single-crystal Fe_2O_3 nanowire array and its photoelectrochemical properties

Pt is an effective dopant which could increase the photoelectrochemical performance of Fe_2O_3 [20]. For example, Hu et al. has reported a Pt doped Fe_2O_3 nanoparticle prepared by a simple electrodeposition method [21], and the photocurrent density was increased from 0.69 mA/cm^2 to 1.43 mA/cm^2 at 0.4 V vs. Ag/AgCl due to enhancing the donor concentration. It has been reported that Pt doping could improve the electrical conductivity of Fe_2O_3. Also, Pt doping could reduce the energy gap of 0.15 eV [22], which improve the solar light absorption and PEC efficiency.

In this section, the author has investigated the effect of Pt doping on the single-crystal Fe_2O_3 nanowire array fabricated by the method described in chapter 4.

5.2.1 Preparation of Fe_2O_3 nanowire array photoanode

Based on the optimized experimental condition reported in chapter 4 (Table 5.1), high density single-crystal Fe_2O_3 nanowire array was fabricated, as shown in Fig. 5.1.

Table. 5.1 Experimental conditions

Heating temperature	Heating time	Surface condition
600 ^oC	90 minutes	polished

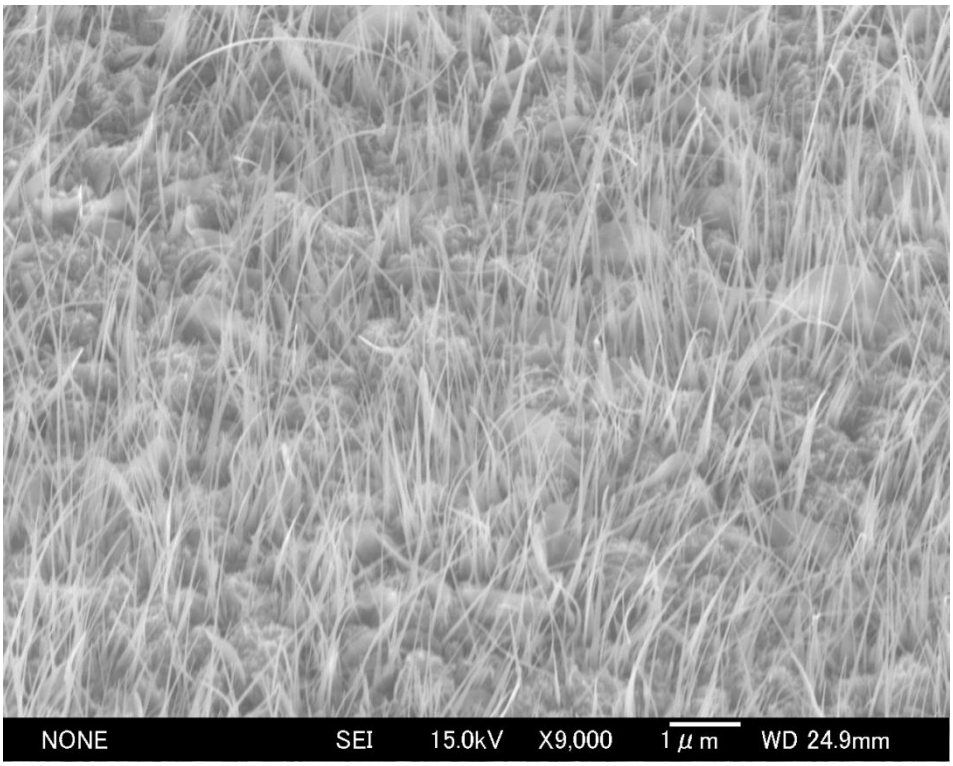

Fig. 5.1 Fe_2O_3 nanowire arrays used for Pt doping experiment.

The Pt doping experiment was carried out with a sputtering equipment (SANYU SC-701HMC Ⅱ). Samples with different Pt sputtering time have been prepared in order to compare the photoelectrochemical performance, as shown in Table. 5.2. After that, the Pt doped Fe_2O_3 nanowire array photoanodes were assembled using the method described in chapter 2.

Table. 5.2 Experimental conditions

Samples	Sputtering time (seconds)	Sputtering Material
1	5	
2	10	Platinum (Pt)
3	20	
4	30	

Figure 5.2 shows the SEM image of Fe_2O_3 nanowire array after 5 seconds Pt sputtering. It can be found that the diameter of the nanowire did not change much

from the sample without sputtering. However, due to the effect of sputtering, some of the nanowires begin to bend at the top. Fig. 5.3 is the SEM image of Fe_2O_3 nanowire array after 30 seconds Pt sputtering. From the SEM result it can be found that all the nanowire was covered with Pt on the surface after a long time sputtering, which is a core shell structure. It is considered that the thickness of the doped Pt layer will effect the light absorption because the Fe_2O_3 nanowire inside may not have a contact with the light.

TEM observation was carried out from the sample after 20 seconds Pt sputtering, as shown in Fig. 5.4. The core (Fe_2O_3) shell (Pt) structure has been confirmed from the TEM results. The thickness of formed Pt layer is 15 nm, approximately.

Fig. 5.2 Fe_2O_3 nanowire array after 5 seconds Pt sputtering

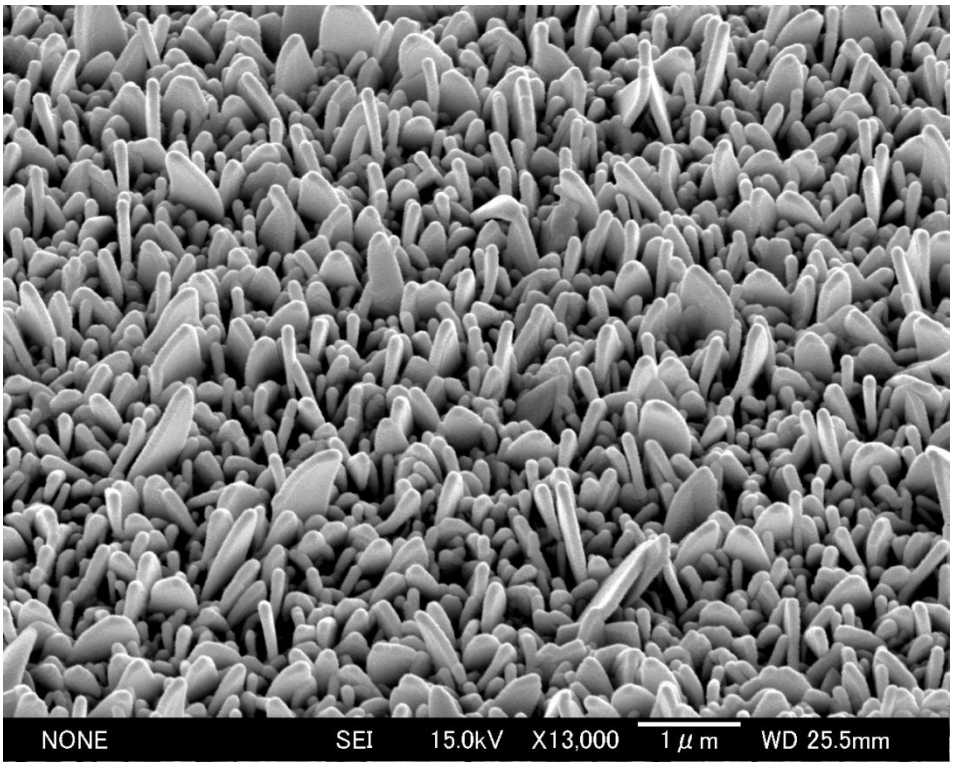

Fig. 5.3 Fe_2O_3 nanowire array after 30 seconds Pt sputtering

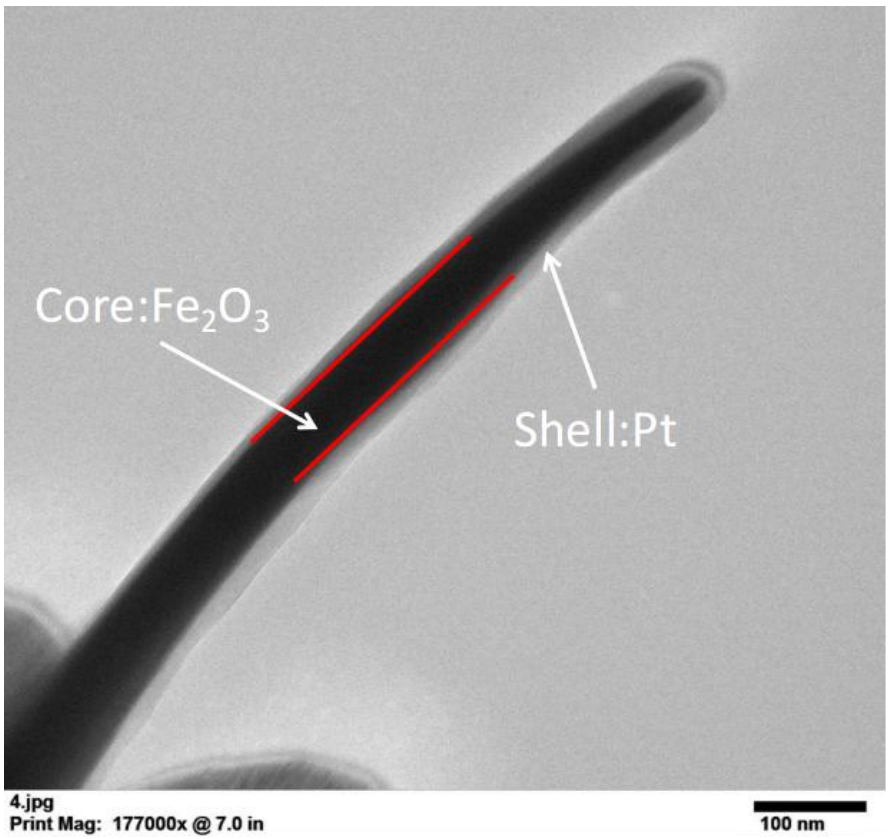

Fig. 5.4 TEM observation of single nanowire after 20 seconds Pt sputtering

XRD observation of all the samples was carried out in order to confirm the Pt sputtering experiments, as shown in Fig. 5.5. From the XRD result, it can be found that the peak of Pt is very weak compared to those of the Fe_2O_3, which is due to the small Pt volume from the sputtering experiment. However, by comparing the peak appeared at 44°, the increasing of the Pt peak become sharp with increase in sputtering time.

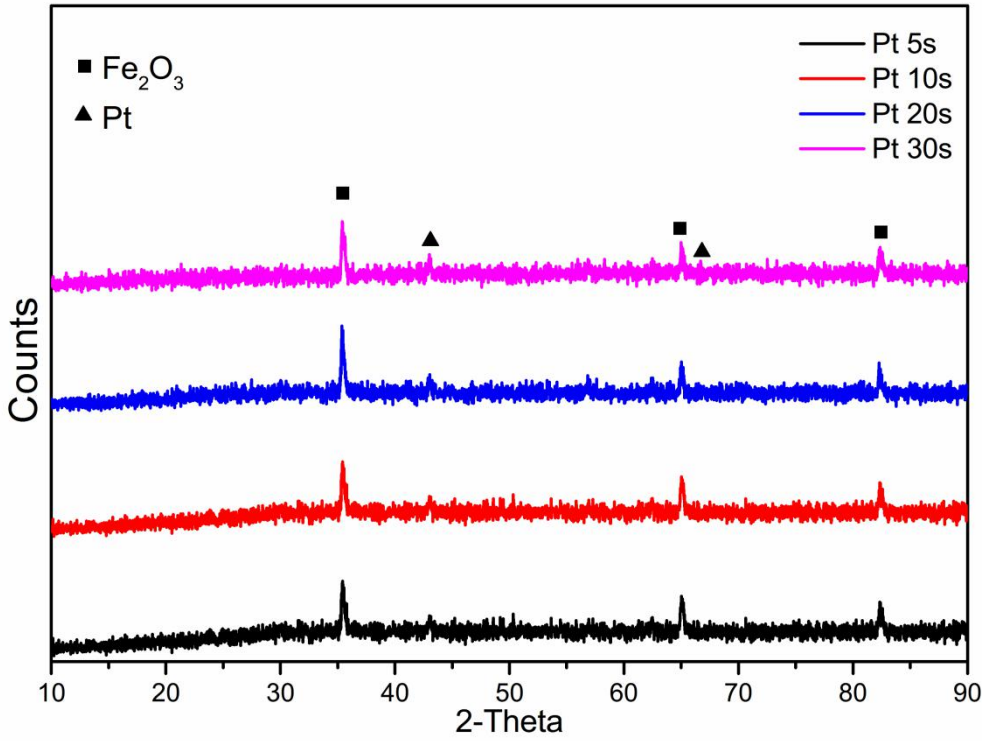

Fig. 5.5 XRD patterns of Fe_2O_3 nanowire array after Pt sputtering.

5.2.2 Photoelectrochemical properties of Pt doped Fe_2O_3 nanowire array

Photocurrent density of the Pt doped Fe_2O_3 nanowire arrays have been measured with the three electrode system, as shown in Fig. 5.6. It can be seen that sample with the 10 seconds Pt sputtering shows the highest photocurrent density, that is 1.096 mA/cm^2 at 1.23 V vs. RHE. Sample with 5 seconds Pt sputtering shows the second

highest photocurrent density, which is 0.95 mA/cm^2 at 1.23 V vs. RHE. The photocurrent density of samples with 20 and 30 seconds Pt sputtering is 0.61 and 0.23 mA/cm^2 at 1.23 V vs. RHE, respectively. By comparing the photocurrent density of pure Fe_2O_3 nanowire array photoanode without Pt sputtering (0.69 mA/cm^2 at 1.23 V vs. RHE), the photocurrent density has been enhanced successfully by 10s Pt sputtering.

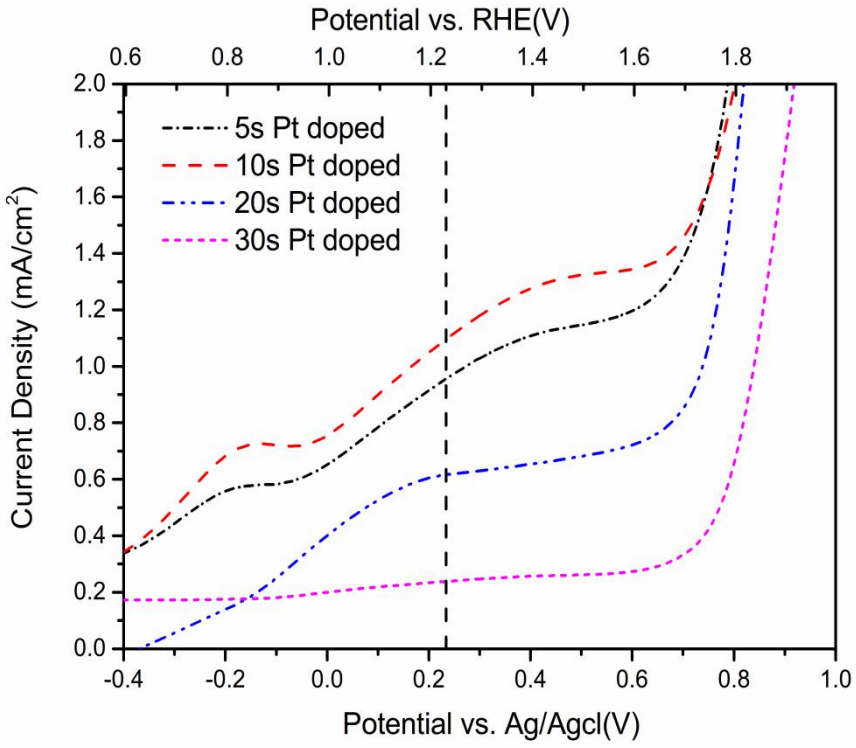

Fig. 5.6 Photocurrent densities of Pt doped Fe_2O_3 nanowire array photoanodes.

5.3 Sn-doped single-crystal Fe_2O_3 nanowire array and its photoelectrochemical properties

Recently, Sn doped Fe_2O_3 photoanode has attracted interest of many researchers because it can change the optical and electrical properties of Fe_2O_3 greatly. It is believed that the Sn doping could impact the charge transfer between the interface of Fe_2O_3 photoanode and electrolyte [20]. Dunn et al has fabricated a Sn doped mesoporous worm-like Fe_2O_3 photoanode, and a higher surface hole transfer efficiency was confirmed by the photocurrent transient analysis [23]. Moreover, Sn doped Fe_2O_3 nanocorals fabricated by hydrothemal method shows a high photocurrent density of 1.86 mA/cm^2 at 1.23 V vs. RHE [16]. The author believed that the enhancement of PEC efficiency was a synergistic effect of Sn introduced carrier density and the increased light absorption.

In this section, the PEC performance of Sn doped single-crystal Fe_2O_3 nanowire array photoanode was confirmed.

5.3.1 Experimental conditions

The same single-crystal Fe_2O_3 nanowire array photoanodes used for Pt doping were used in the Sn doping experiments. Based on the results from Pt doped experiments, the Sn sputtering time has been set from 5 seconds to 40 seconds, as shown in Table 5.3.

Table. 5.3 Experimental conditions

Samples	Sputtering time (seconds)	Sputtering Material
1	5	
2	10	
3	20	Stannum (Sn)
4	30	
5	40	

The prepared nanowire array with 30 seconds Sn sputtering is shown in Fig. 5.7. From SEM observation, it can be found that many nanowires have become bent after sputtering. The TEM result of the sample after 20 seconds Sn sputtering is shown in Fig. 5.8. A core-shell structure can be found from this result, and the thickness of the Sn shell was measured to be 8.6 nm, approximately.

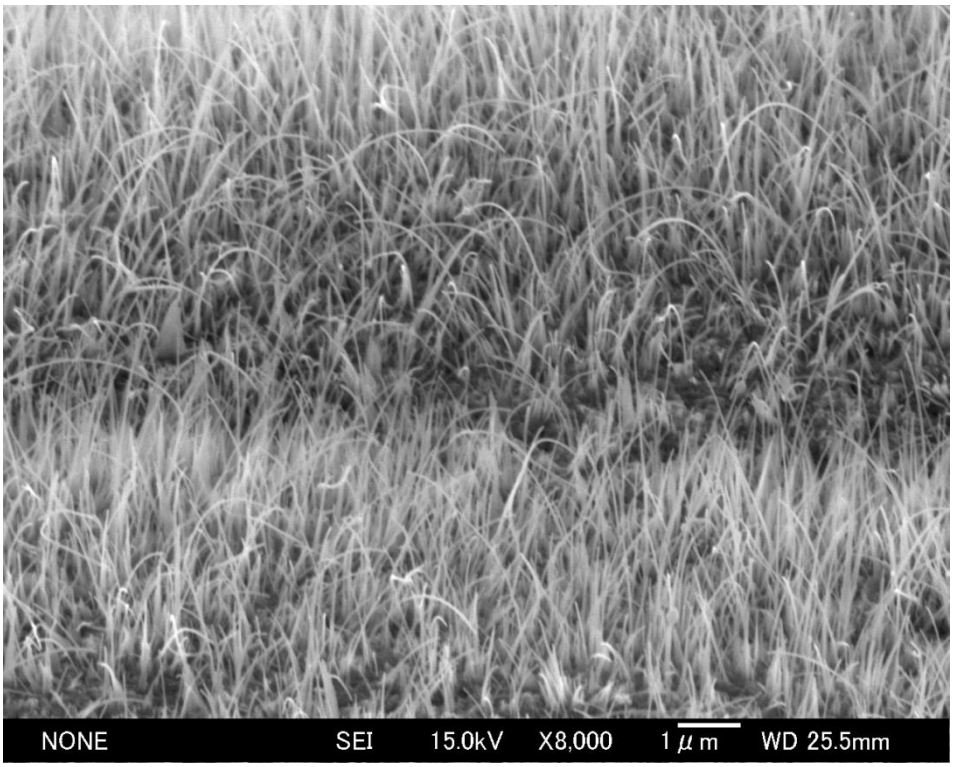

Fig. 5.7 Fe_2O_3 nanowire array after 30 seconds Sn sputtering

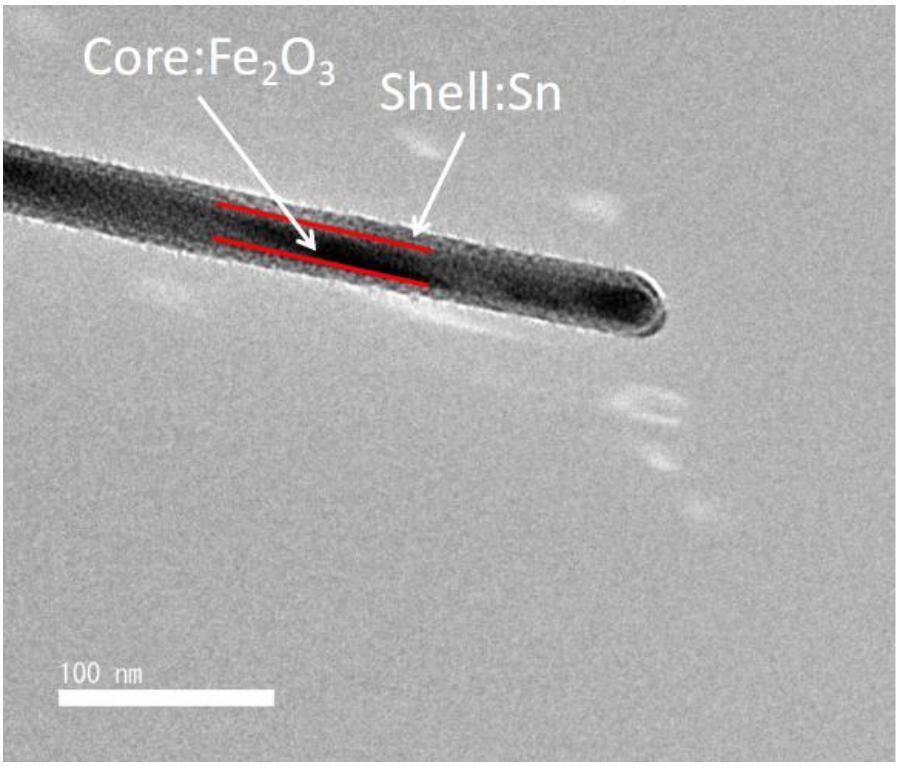

Fig. 5.8 TEM observation of single nanowire after 20 seconds Sn sputtering

5.3.2 Photoelectrochemical properties of Sn doped Fe_2O_3 nanowire array

Figure 5.9 is the photocurrent density results of Sn doped Fe_2O_3 nanowire array. The photocurrent density results for sample with Sn sputtering for 5 seconds, 10 seconds and 20 seconds are 0.68 mA/cm^2, 0.73 mA/cm^2 and 1.21 mA/cm^2 at 1.23 V vs. RHE, respectively. However, when the sputtering time of Sn was increased to 30 seconds and 40 seconds, the photocurrent density dropped rapidly, and dark current of the 40 seconds sample is also very large. Therefore it is considered that the Sn layer has fully covered the surface of iron at these conditions.

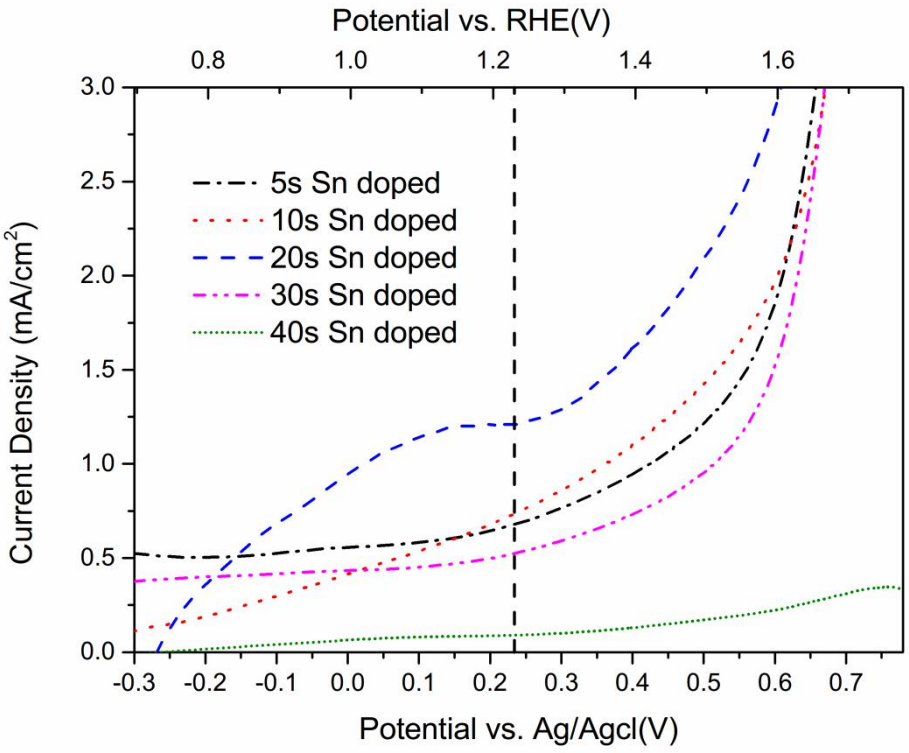

Fig. 5.9 Photocurrent densities of Sn doped Fe_2O_3 nanowire array photoanodes.

5.4 Ti-doped single-crystal Fe_2O_3 nanowire array and its photoelectrochemical properties

Among all the doping material used for improve the photoelectrochemical properties of Fe_2O_3, Ti is the most popular candidate being studied [24-26]. Compared to the undoped Fe_2O_3 photoanodes, Ti doping can enhance the electron mobility and reduce the effective mass of electrons [27]. Some studies of Ti doped hematite have shown a very high photocurrent results [28]. For example, Wang et al. have fabricated a Ti doped Fe_2O_3 nanoparticles by using a new deposition annealing method on FTO substrates, the fabricated sample shows a photocurrent density of 2.8 mA/cm^2 at 1.23 V vs. RHE. Deng et al. fabricated a Ti doped Fe_2O_3 nanorods photoanode on FTO with a hydrothermal method, and enlarged the photocurrent density to be 1.91 mA/cm^2 at 1.23 V vs. RHE. From these studies, it is revealed that Ti doping could improve charge transfer and collection efficiency by changing the surface properties

of Fe_2O_3. Ti modifications could also reduce the recombination of photogenerated electron and hole, therefore, a higher efficiency could be achieved [29].

In this section, the effect of Ti doping on single-crystal Fe_2O_3 nanowire array was studied.

5.4.1 Experimental conditions

The same single-crystal Fe_2O_3 nanowire array photoanodes used for Pt doping were used in the Ti doping experiments. Based on the results from Pt doped experiments, sputtering time of Ti sputtering has been set from 5 seconds to 30 seconds, as shown in Table 5.4.

Table. 5.4 Experimental conditions

Samples	Sputtering time (seconds)	Sputtering Material
1	5	Titanium (Ti)
2	10	
3	20	
4	30	

The prepared nanowire array with 20 seconds Ti sputtering is shown in Fig. 5.10. Most of Ti doped Fe_2O_3 nanowires are still straight after sputtering process. The core-shell structure has also been confirmed from the TEM observation, as shown in the Fig. 5.11, and the thickness of the Ti shell after 20 seconds sputtering was measured to be 11.1 nm, approximately.

Fig. 5.10 Fe_2O_3 nanowire array after 20 seconds Ti sputtering

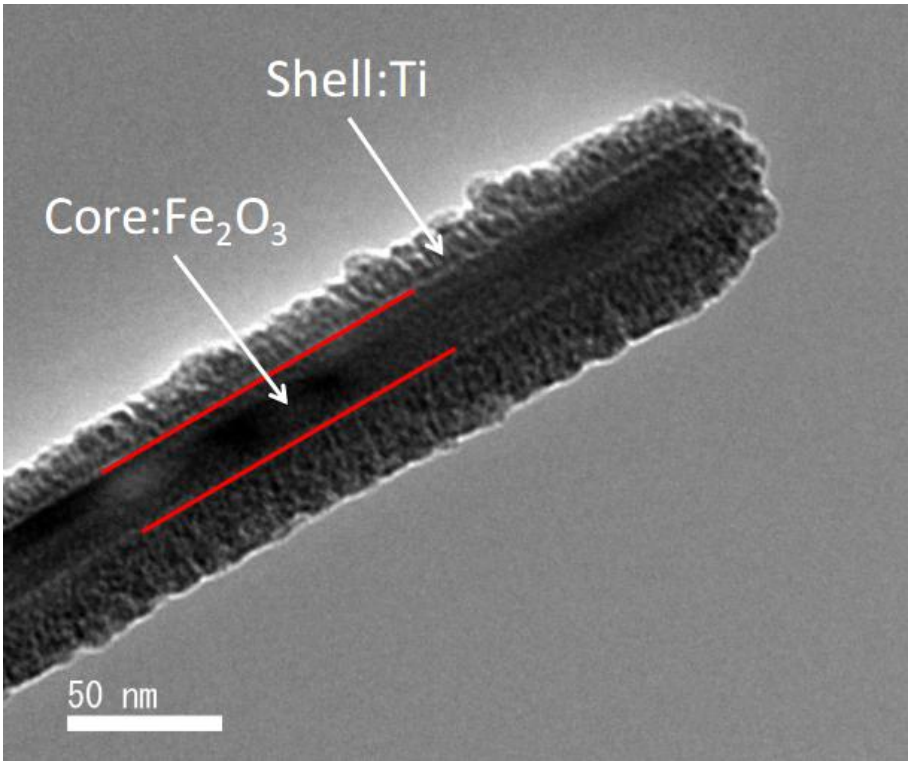

Fig. 5.11 Fe_2O_3 nanowire array after 20 seconds Ti sputtering

5.4.2 Photoelectrochemical properties of Ti doped Fe_2O_3 nanowire array

Figure. 5.12 is the photocurrent density results of Ti doped Fe_2O_3 nanowire array. The photocurrent density of Fe_2O_3 nanowire array photoanode with Ti sputtering for 5 seconds, 10 seconds and 20 second is 0.61mA/cm^2, 0.72 mA/cm^2 and 1.94 mA/cm^2 at 1.23 V vs. RHE, respectively. The observed photocurrent density of sample with Ti sputtering for 30 seconds is 1.152 mA/cm^2 at 1.23 V vs. RHE. It is considered that the thickness of the Ti sputtering is too large for the Fe_2O_3 nanowire array photoanode at this condition.

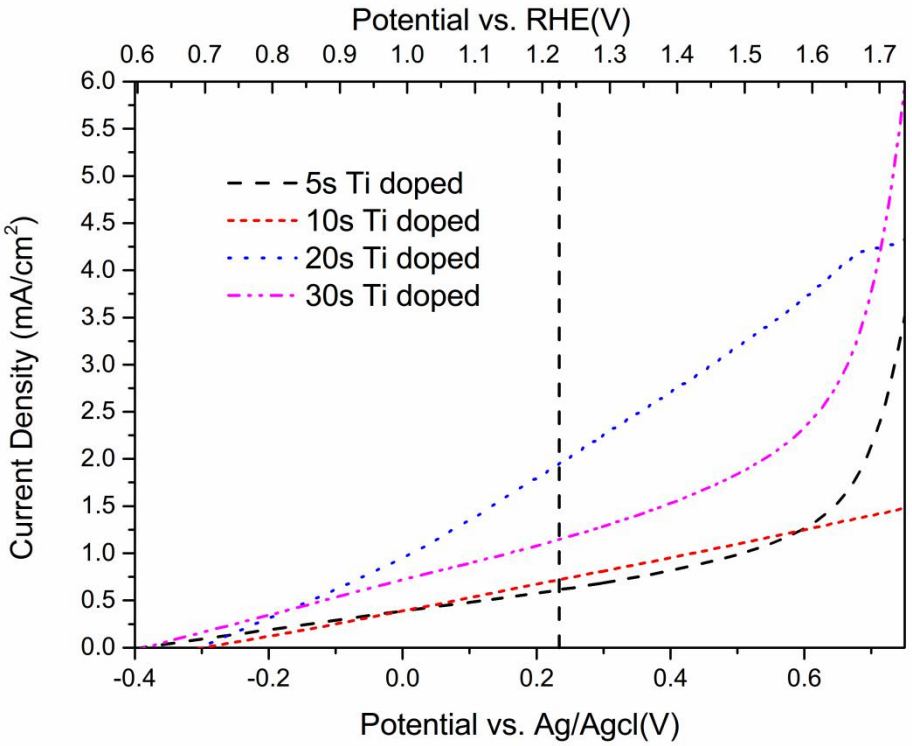

Fig. 5.12 Photocurrent densities of Ti doped Fe_2O_3 nanowire array photoanodes.

5.5 Summary

In this chapter, single-crystal Fe_2O_3 nanowire-array photoanodes with different materials doping have been studied.The current densities under each experimental condition are summarized in Fig. 5.13. For the Pt doping, the best result was obtained from the sample after 10 seconds of Pt sputtering, with the photocurrent density of 1.096 mA/cm^2 at 1.23 V vs. RHE. In Sn doping, the best result was obtained from the sample after 20 seconds of Sn sputtering, with the photocurrent density of 1.21 mA/cm^2 at 1.23 V vs. RHE. The largest photocurrent density was obtained from the sample after 20 seconds of Ti sputtering, with the photocurrent density of 1.94 mA/cm^2 at 1.23 V vs. RHE. The thickness changing with sputtering time for different doped materials is summarized in Fig. 5.14, It can be found that the thickness of doped materials for 10 seconds Pt sputtering, 20 seconds Sn sputtering, and 20 seconds Ti sputtering are similar, which is the condition to reach the maximum value of photocurrent density. Therefore, it is indicated that the suitable thickness of doped material to functionalize the Fe_2O_3 nanowire array is around 10 nm.

Compared to the photoelectrochemical performance of Ti doped Fe_2O_3 photoanodes reported in other literatures, such as Wang et al. reported a Ti doped Fe_2O_3 film with a photocurrent of 2.8 mA/cm^2 at 1.23 V vs. RHE [30], Maxime et al. reported a Ti doped Fe_2O_3 film with a photocurrent of 2.4 mA/cm^2 at 0.8 V vs. Ag/AgCl [31], and Lee et al. reported a nanostructured Ti-doped Fe_2O_3 photoanodes with a photocurrent of 2.1 mA/cm^2 at 0.7 V vs. Ag/AgCl [32], the result of this study (1.94 mA/cm^2 at 1.23 V vs. RHE) is not the best result. However it should be mentioned that all the above mentioned results were obtained based on FTO glass. Therefore, by instead of the Fe substrate with FTO glass, photocurrent density of the demonstrated method in this study could be improved.

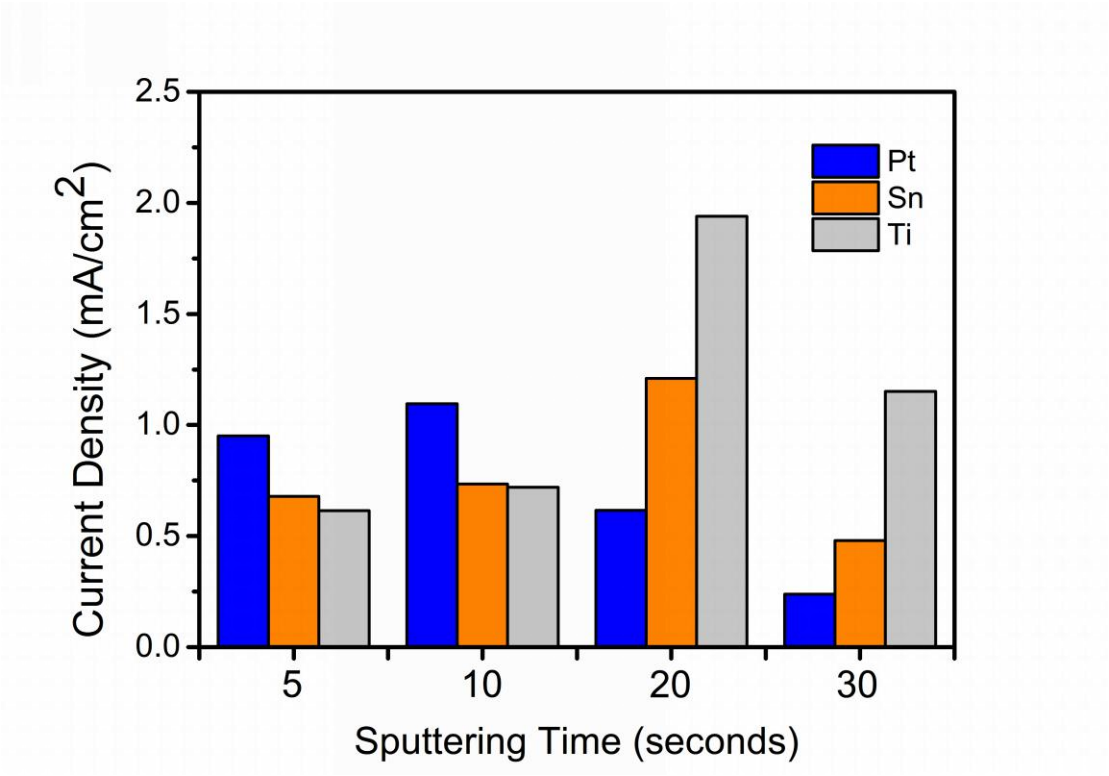

Fig. 5.13 Current density comparison of each doped material

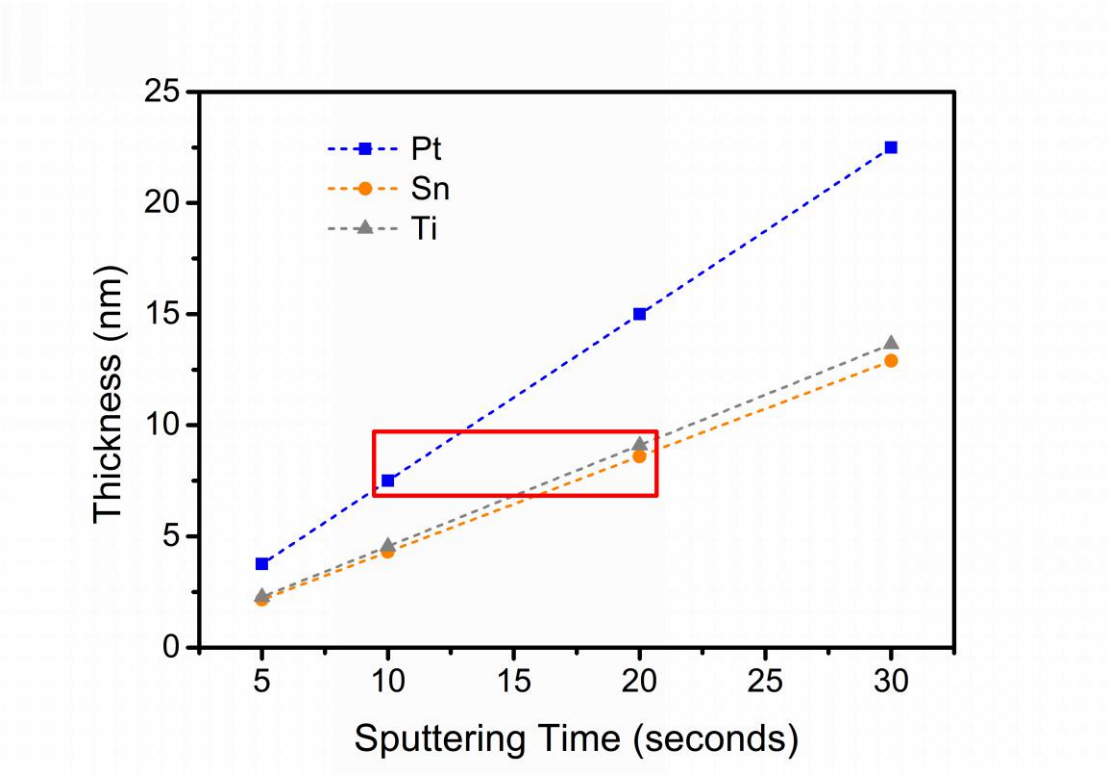

Fig. 5.14 Thickness comparison of each doped material

References

1. Cherepy N J, Liston D B, Lovejoy J A, et al. Ultrafast studies of photoexcited electron dynamics in γ-and α-Fe_2O_3 semiconductor nanoparticles[J]. The Journal of Physical Chemistry B, 1998, 102(5): 770-776.
2. He Y P, Miao Y M, Li C R, et al. Size and structure effect on optical transitions of iron oxide nanocrystals[J]. Physical Review B, 2005, 71(12): 125411.
3. Zhong D K, Gamelin D R. Photoelectrochemical water oxidation by cobalt catalyst ("Co-Pi")/α-Fe_2O_3 composite photoanodes: oxygen evolution and resolution of a kinetic bottleneck[J]. Journal of the American Chemical Society, 2010, 132(12): 4202-4207.
4. Zhu J, Yin Z, Yang D, et al. Hierarchical hollow spheres composed of ultrathin Fe_2O_3 nanosheets for lithium storage and photocatalytic water oxidation[J]. Energy & Environmental Science, 2013, 6(3): 987-993.
5. Wang L, Zhou X, Nguyen N T, et al. Plasmon‐Enhanced Photoelectrochemical Water Splitting Using Au Nanoparticles Decorated on Hematite Nanoflake Arrays[J]. ChemSusChem, 2015, 8(4): 618-622.
6. LaTempa T J, Feng X, Paulose M, et al. Temperature-dependent growth of self-assembled hematite (α-Fe_2O_3) nanotube arrays: rapid electrochemical synthesis and photoelectrochemical properties[J]. The Journal of Physical Chemistry C, 2009, 113(36): 16293-16298.
7. Zhang R, Fang Y, Chen T, et al. Enhanced Photoelectrochemical Water Oxidation Performance of Fe_2O_3 Nanorods Array by S Doping[J]. ACS Sustainable Chemistry & Engineering, 2017, 5(9): 7502-7506.
8. Hu Y S, Kleiman-Shwarsctein A, Forman A J, et al. Pt-doped α-Fe_2O_3 thin films active for photoelectrochemical water splitting[J]. Chemistry of Materials, 2008, 20(12): 3803-3805.
9. Hsu Y P, Lee S W, Chang J K, et al. Effects of platinum doping on the photoelectrochemical properties of Fe_2O_3 electrodes[J]. Int. J. Electrochem. Sci, 2013, 8: 11615-11623.

10. Wang Y, Wang S, Zhao Y, et al. H 2 S sensing characteristics of Pt-doped α-Fe_2O_3 thick film sensors[J]. Sensors and Actuators B: Chemical, 2007, 125(1): 79-84.
11. Zeng Y, Han Y, Zhao Y, et al. Advanced Ti‐Doped Fe_2O_3@ PEDOT Core/Shell Anode for High‐Energy Asymmetric Supercapacitors[J]. Advanced Energy Materials, 2015, 5(12).
12. Kobayashi T, Haruta M, Sano H, et al. A selective CO sensor using Ti-doped α-Fe_2O_3 with coprecipitated ultrafine particles of gold[J]. Sensors and Actuators, 1988, 13(4): 339-349.
13. Droubay T, Rosso K M, Heald S M, et al. Structure, magnetism, and conductivity in epitaxial Ti-doped α-Fe_2O_3 hematite: Experiment and density functional theory calculations[J]. Physical Review B, 2007, 75(10): 104412.
14. Zhang P, Kleiman-Shwarsctein A, Hu Y S, et al. Oriented Ti doped hematite thin film as active photoanodes synthesized by facile APCVD[J]. Energy & Environmental Science, 2011, 4(3): 1020-1028.
15. Hahn N T, Mullins C B. Photoelectrochemical performance of nanostructured Ti-and Sn-doped α-Fe_2O_3 photoanodes[J]. Chemistry of Materials, 2010, 22(23): 6474-6482.
16. Ling Y, Wang G, Wheeler D A, et al. Sn-doped hematite nanostructures for photoelectrochemical water splitting[J]. Nano letters, 2011, 11(5): 2119-2125.
17. Fitzgerald C B, Venkatesan M, Douvalis A P, et al. SnO_2 doped with Mn, Fe or Co: room temperature dilute magnetic semiconductors[J]. Journal of applied physics, 2004, 95(11): 7390-7392.
18. Jang J S, Yoon K Y, Xiao X, et al. Development of a potential Fe_2O_3-based photocatalyst thin film for water oxidation by scanning electrochemical microscopy: effects of Ag-Fe_2O_3 nanocomposite and Sn doping[J]. Chemistry of Materials, 2009, 21(20): 4803-4810.
19. Jang J S, Yoon K Y, Xiao X, et al. Development of a potential Fe_2O_3-based photocatalyst thin film for water oxidation by scanning electrochemical microscopy: effects of Ag-Fe_2O_3 nanocomposite and Sn doping[J]. Chemistry of

Materials, 2009, 21(20): 4803-4810.

20. Zhang Y, Ji H, Ma W, et al. Doping-promoted solar water oxidation on hematite photoanodes[J]. Molecules, 2016, 21(7): 868.
21. Hu Y S, Kleiman-Shwarsctein A, Forman A J, et al. Pt-doped α-Fe_2O_3 thin films active for photoelectrochemical water splitting[J]. Chemistry of Materials, 2008, 20(12): 3803-3805.
22. Neufeld O, Toroker M C. Platinum-doped α-Fe_2O_3 for enhanced water splitting efficiency: a DFT+ U study[J]. The Journal of Physical Chemistry C, 2015, 119(11): 5836-5847.
23. Dunn H K, Feckl J M, Müller A, et al. Tin doping speeds up hole transfer during light-driven water oxidation at hematite photoanodes[J]. Physical Chemistry Chemical Physics, 2014, 16(44): 24610-24620.
24. Morin F J. Electrical Properties of α-Fe_2O_3 and α-Fe_2O_3 Containing Titanium[J]. Physical Review, 1951, 83(5): 1005.
25. Rioult M, Magnan H, Stanescu D, et al. single-crystalline hematite films for solar water splitting: Ti-doping and thickness effects[J]. The Journal of Physical Chemistry C, 2014, 118(6): 3007-3014.
26. Kronawitter C X, Zegkinoglou I, Shen S H, et al. Titanium incorporation into hematite photoelectrodes: theoretical considerations and experimental observations[J]. Energy & Environmental Science, 2014, 7(10): 3100-3121.
27. Huda, M.N.; Walsh, A.; Yan, Y.; Wei, S.-H.; Al-Jassim, M.M. Electronic, structural, and magnetic effects of 3d transition metals in hematite. J. Appl. Phys. 2010, 107, 123712. [CrossRef]
28. Deng J, Zhong J, Pu A, et al. Ti-doped hematite nanostructures for solar water splitting with high efficiency[J]. Journal of Applied Physics, 2012, 112(8): 084312.
29. Annamalai A, Lee H H, Choi S H, et al. Sn/Be sequentially co-doped hematite photoanodes for enhanced photoelectrochemical water oxidation: effect of Be2+ as co-dopant[J]. Scientific reports, 2016, 6: 23183.
30. Wang G, Ling Y, Wheeler D A, et al. Facile synthesis of highly photoactive

α-Fe_2O_3-based films for water oxidation[J]. Nano letters, 2011, 11(8): 3503-3509.

31. Rioult M, Magnan H, Stanescu D, et al. single-crystalline hematite films for solar water splitting: Ti-doping and thickness effects[J]. The Journal of Physical Chemistry C, 2014, 118(6): 3007-3014.
32. Lee M H, Park J H, Han H S, et al. Nanostructured Ti-doped hematite (α-Fe_2O_3) photoanodes for efficient photoelectrochemical water oxidation[J]. International Journal of Hydrogen Energy, 2014, 39(30): 17501-17507.

Chapter 6 Conclusions

The increasing fossil fuels consumption and CO_2 concentration drive the search for new sustainable energy. Hydrogen is a promising energy for the future since it is clean, renewable, sustainable and zero emission. Solar water splitting is a novel hydrogen production method, which uses only water and sunlight to produce hydrogen. Fe_2O_3 is a suitable semiconductor materials for this application, which could meet most of the requirements of solar water splitting, however there are still several disadvantages limited the photoelectrochemical efficiency of Fe_2O_3. In this work, the author is mainly focused to improve the photoelectrochemical performance of Fe_2O_3 photoanode by nanostructuring and surface modification used for solar water splitting.

In order to overcome the limitation of Fe_2O_3 and improve the PEC efficiency of Fe_2O_3, a novel fabrication method to synthesis the high density Fe_2O_3 nanowire array was demonstrated. By introducing the water vapor in the fabrication process, a Fe_2O_3 nanowire array with high density of 8.66 wire/μm^2 was obtained, and the best experimental condition for high density Fe_2O_3 nanowire array growth is heated at 450 ^oC for 90 minutes, with the water vapor volume of 0.2L/h. The photocurrent density of the as-prepared sample is 0.65 mA/cm^2 at 1.23 V vs. RHE, and the IPCE was measured to be 5.54% at 400nm wavelength. It is believed that the role of water vapor in the fabrication process is increasing the oxidation from Fe to Fe_2O_3, which will increase the stress induced driving force for atom diffusion, therefore, the high density nanowire array can be obtained.

Compare to the polycrystalline nanostructure and bulk material, single-crystal nanostructure is believed to be able to provide a higher PEC efficiency because it could reduce the recombination of photogenerated electrons and holes. A new method to prepare the single-crystal high density Fe_2O_3 nanowire have been proposed in this study. By polishing the surface of iron plate before heating, an extremely high density

single-crystal Fe_2O_3 nanowire array was fabricated. The optimized experimental condition is heat the polished sample at 600 ^oC for 90 minutes. A single-crystal Fe_2O_3 nanowire array with the density of 28.75 wire/μm^2 has been fabricated successfully under this condition. The photocurrent density is 0.69 mA/cm^2 at 1.23 V vs. RHE and the IPCE is 6.8% at 400 nm wavelength. After surface polishing treatment, the surface roughness was increased from 0.433 μm to 2.483 μm, and the residual stress of the iron plate was measured by a XRD analysis, it is found that the residual stress was increased from -28.99 MPa to -125.3 MPa. The increased surface roughness and residual stress are considered to increase the driving force for the nanowire growth.

After the best nanostructure of Fe_2O_3 being investigated, the surface modifications of the Fe_2O_3 photoanode were carried out in order to achieve a higher PEC performance. Ti, Sn and Pt have been doped on the photoanode surface by a sputtering equipment. It was found that 20 seconds of Ti doping showed a high photocurrent density of 1.94 mA/cm^2 at 1.23 V vs. RHE.

Based on this research, we have found a new method to fabricate high density single-crystal Fe_2O_3 nanowire array used for the photoanode of solar water splitting. With the fabricated Fe_2O_3 nanowire photoanode and Ti doped functionalization, high photocurrent density has be realized for solar water splitting. The new finds of this research bring a promising potential to use solar water splitting for along term massive hydrogen production.

Acknowledgements

First and foremost, I would like to express my sincere gratitude to my supervisor Prof. Yang Ju, Nagoya University, for giving me the chance to study and work in this wonderful laboratory for six years as a master and doctor student. He has taught me many things, not only the knowledge, the research skills, but also includes the logical thinking, and the serious attitudes in details. His guidance, meticulous care and continuously support have always enlightened me when I feel confused in my research and life. It has been a long journey of the days worked with Prof. Ju. At the end, I really want to say thanks again to Prof. Ju for everything he has done for me.

I am grateful to Prof. Noritsugu Umehara and Prof. Koji Mizuno, Nagoya University, for their professional advice and kind help on my research.

I would like to express my sincere gratitude to Prof. Masumi Saka, Tohoku Univesity. Thanks him for his valuable suggestions on my thesis, his inspiration has expanded my horizons and guided me deeply understanding my research.

Also, I would like to thank Assoc. Prof. Yasuyuki Morita, Nagoya University, for the encouragement of all the time. The meeting with Prof. Morita always makes me feel confidence to overcome the next challenge.

I would also like to thank Assistant Prof. Yuhki Toku, Nagoya University, for the time we discussed about every details in the research.

Thanks to all the members in Ju lab. Thanks for all the help and support they provide, and thanks for the good time we spent together.

Finally, I would like to say thanks to my parents for their unbounded love and support.